Universitat Autònoma de Barcelona

Brillouin scattering in bosonic systems

Omar Enrique Florez Peñaloza

Universitat Autònoma de Barcelona

Doctoral thesis

Brillouin scattering in bosonic systems

Author:
Omar Enrique Florez Peñaloza

Supervisors:
Dr. Pedro David García Fernández
Prof. Dr. Clivia Marfa Sotomayor Torres

Phononic and Photonic Nanostructures Group

2022

Declaration of Authorship

I, Omar Enrique Florez Peñaloza, declare that this thesis titled, "Brillouin scattering in bosonic systems" and the work presented in it are my own. I confirm that:

- This work was done wholly or mainly while in candidature for a research degree at this University.
- Where any part of this thesis has previously been submitted for a degree or any other qualification at this University or any other institution, this has been clearly stated.
- Where I have consulted the published work of others, this is always clearly attributed.
- Where I have quoted from the work of others, the source is always given. With the exception of such quotations, this thesis is entirely my own work.
- I have acknowledged all main sources of help.
- Where the thesis is based on work done by myself jointly with others, I have made clear exactly what was done by others and what I have contributed myself.

Barcelona, October 26, 2022

"*El que anda mucho y lee mucho, ve mucho y sabe mucho.*"

Miguel de Cervantes Saavedra

Abstract

The precise control and guidance of mechanical vibrations at MHz and GHz frequencies has potential applications in the field of signal processing as well as fundamental research at quantum level. At mesoscale level, thermal vibrations can represent a source of noise for many physical phenomena. A proper engineering of frequency band gaps and guided modes can be achieved by implementing periodic materials. The most recent topological approach translated into bosonic systems to guide edge states immune or robust to unwanted scattering is also based in the design of periodic structures.

In this thesis was covered the design and experimental characterization of trivial phononic waveguides, also called defect waveguides, as well as the design of phononic topological waveguides based in the analogy of the quantum spin Hall effect (QSHE) and the quantum valley Hall effect (QVHE). For the case of trivial waveguides, we first report the full characterization of hypersonic bandgaps with up to 64 % of gap to mid-gap ratio. The same structures were used to build defect line waveguides in which it was possible to measure hypersonic guided modes at room temperature by measuring thermally excited phonons in the structure.

For the topological waveguides, design constraints related to the anisotropy of the silicon material and the particular experimental characterization technique implemented here were explored. Using the analogy of the QSHE in bosonic systems, a hybrid phononic-photonic topological insulator based on an hexagonal array of shamrocks features was designed. The pseudospin concept is illustrated with the topological phononic edge modes.

Finally the analog of the QVHE is also explored for designing a phononic crystal that supports topological edge modes above 10 GHz. Te parallel between isotropic and anisotropic silicon is considered in this design to illustrate the geometrical constraints on topological phononic crystals design.

Acknowledgements

Thank you very much to Clivia for the opportunity in her group. Thanks to David for the freedom during all this process.

To all my co-workers who made my life easier and happy during this period: Francisco, Martin P, Emigdio, Guilhem, Juliana, Ryan, Guillermo, Peng, Martin C, Alejandra, Lisa, Philippe.

Special thanks to Prof. Søren Stobbe and Marcus Albrechtsen for the amazing samples that made possible the measurements presented in this work.

Special thanks also to Ryan for all the countless grammar corrections.

To my family because always have been with me, supporting me and taking care of me. To my mother, my father and my brother: gracias por todo.

Contents

List of Figures

List of Abbreviations

PE	**P**hoto **E**lastic
MB	**M**oving **B**oundary
ES	**E**lectro**S**triction
RP	**R**adiation **P**reasure
TFP	**T**andem **F**abry-**P**erot
FSR	**F**ree **S**pectral **R**ange
BLS	**B**rillouin **L**ight **S**cattering
FEM	**F**inite **E**lement **M**ethod
SEM	**S**canning **E**lectron **M**icroscopy
SOI	**S**ilicon **O**n **I**nsulator
CMOS	**C**omplementary **M**etal **O**xide **S**emiconductor
DOS	**D**ensity **O**f **S**tates
FIB	**F**ocus **I**on **B**eam
GPW	**G**lide **P**lane **W**aveguides
CW	**C**ontinuous **W**ave
SNR	**S**ignal to **N**oise **R**atio
QSHE	**Q**uantum **S**pin **H**all textbfEfect
QVHE	**Q**uantum **V**alley **H**all textbfEfect
DP	**D**irac **P**oint
IDT	**I**nter **D**igital **T**ransducer
SAW	**S**urface **A**coustic **W**ave
IoT	**I**nternet **o**f **T**hings

To my mom

Chapter 1

Introduction and motivation

The ever growing demand for data transmission and signal processing claims for devices with higher and higher rates of bandwidth operations. Surface Acoustic Wave (SAW) filters are one of the significant components that have been present in mobile communications and digital television for decades and nowadays widely used also in Internet of Things (IoT) devices. Radio Frequency and wireless applications require to avoid potential interference from surroundings and improve received signal quality. With the use of filters ranging from few kHz up to 6 GHz range this is achieved. It is intuitive to think that increasing the operation range, will increase the amount of processed information. Telecommunication is one of the different fields that clearly illustrates the necessity to control and route high frequency mechanical vibrations.

Nanostructured materials offer the possibility to manipulate the mechanical vibrations of a solid over a specified spectral bandwidth. This in turn enables the control of light–matter interactions in the visible and near-infrared regimes for optomechanical applications ranging from high-resolution accelerometers [1] to mass and force sensors [2, 3], in addition to providing fundamental insights into phenomena such as quantum ground-state cooling [4, 5]. By periodically distributing the mass within a system, it is possible to engineer its mechanical modes [6, 7] and open frequency windows over which the destructive interference of scattered waves forbids any phonon propagation [8, 9]. This approach enables engineering of the thermal conductance of the structure [10] and allows for the routing of phonons at the mesoscale [11]. Although full-gap gigahertz phononic crystals are widely used in optomechanical systems to create phononic shields [12], waveguides and cavities [13–16], clear and direct experimental evidence of a complete omnidirectional phononic bandgap at hypersonic (GHz) frequencies is still lacking.

The experimental work reported until now is generally limited to megahertz frequencies up to the 1 GHz band, using piezoelectric materials to drive the system [17, 18], requiring varying interdigitated electrodes to probe different frequencies and propagation directions. For gigahertz frequencies, only partial and narrow mechanical bandgaps (with up to 8% gap-to-midgap ratio) have been shown using assembled platforms such as colloidal crystals [19] or two-dimensional phononic crystal membranes [20]. Furthermore, the control and guiding of elastic waves at gigahertz frequencies has been difficult to achieve or measure, relying on complex optomechanical systems or nonlinear stimulated phenomena [21].

In this thesis it is reported direct experimental evidence of a wide full phononic gap with a central frequency at 8.4 GHz and a spectral width of 5.3 GHz (a gap-to-midgap ratio of 64%) in a free-standing patterned silicon membrane phononic crystal. Additionally, it is created a line-defect waveguide with the same geometry in which

we directly measure two guided modes at 5.7 GHz and 7.1 GHz within the bandgap at room temperature. We demonstrate the passive spectral tunability of the mechanical gap as a function of the geometric parameters of the crystal, with a spectral shift spanning the range from approximately 4 GHz to 11.5 GHz, which subsequently also enables spectral tunability of the guided modes.

The standard definition of topology is: the study of quantities that are preserved under continuous (adiabatic) perturbations. The study of topological phases of mater started recently in 1980 with the discovering of the quantum Hall effect (QHE) by Von Klitzing [22]. shortly after was shown that the quantization of the conductance in this effect was originated by the non-trivial topological properties of the energy bands, described by the TKNN theory [23], later refereed as the band Chern number C. the Chern number describes the geometrical phase, commonly known as Berry phase [24], accumulated over the Brillouin zone, that is therefore related with the topological invariant of energy bands in the reciprocal space [25].

In 2006 was experimentally demonstrated that by applying an external magnetic field, the spin-orbital coupling of a material can also originate topological phases [26]. This effect is known as quantum spin Hall effect (QSHE). This was the first observation of spin currents with minimum dissipation. Also in this century was introduced another approach to optain topological protected states known as the quantum valley Hall effect (QVHE) [27]. Valley refers to the two energy extrema generally located at K and K', at wich the Berry curvature have opposite signs giving a zero integral over the full Brillouin zone [25].

The same ideas discovered in condensed matter physics were translated to bosonic systems. The analogue of QHE in photonic crystals was shown [28], and more recently the analog of QSHE [29] and QVHE [30] in acoustic systems. The complexity of topological designs have limitated the fabrication of many of them down to nanoscale and therefore, the analog of QSHE and QVHE at hypersonic frequencies is still pending. The experimental realization of topological states at hypersonic frequencies is limited to 1 GHz [31]. In this thesis is evaluated the phononic analog of both approach with the design of two different crystal geometries. The geometrical, material and experimental limitation are detailed in each model with the aim to optimize the best platform for the further experimental demonstration.

1.1 Thesis outline

This thesis covers the design of trivial and topological phononic waveguides. Here it is presented experimental evidence of trivial hypersonic guided modes. For the topological phononic waveguides, design and experimental limitations are presented. The content of each chapter is summarized below.

- **Chapter 2** presents the theoretical background of Brillouin scattering, the deduction of the phase matching condition as a function of the scattering angle and also a brief explanation of the two main physical mechanisms responsible for the spontaneous scattering process: the moving boundary and the photoelastic effect. It is the basis to understand how Brillouin light scattering spectroscopy works and what is the most optimal experimental configuration for the detection of thermal excited phonons. In this chapter is also presented a simple

experimental validation of numerical simulations measuring an unpatterned silicon membrane. Finally it is presented the analytical deduction of the coupling coefficients for the moving-boundary perturbation.

- **Chapter 3** presents a brief introduction of phononic crystals. After that it is introduced the shamrock geometry, widely used in this work, and it is explained the relation between this particular geometry and the apperance of wide full mechanical bandgaps. This geometry is optimized to be implemented in the standard SOI platform that offers CMOS compatibility for reliable fabrication at nanoscale level. The CORE fabrication process is summarized and from the fabricated samples is elaborated an statistical analysis of the geometrical fluctuations based in the extracted information from SEM images. Finally it is presented the experimental band reconstruction of GHz phononic bandgaps and is showed how the variations in the vertical profile of the nanostructures causes important changes in frequency.
- **Chapter 4** introduces the concept of defect waveguides and how this idea is applied to design hypersonic trivial waveguides based on the shamrock crystal geometry. In this chapter it is presented the geometrical optimization in order to obtain the best confinement of guided modes. Based on this optimization it is presented the experimental detection of hypersonic guided modes detected at room temperture with no external excitation. Finally the waveguide dispersion relation is experimentally reconstructed using Brillouin light scattering spectroscopy.
- **Chapter 5** presents the analog of the quantum spin Hall effect in a hybrid optomechanic crystal based in an hexagonal array of shamrock features. It is illustrated the band folding concept as a result of a change in the considered unit cell of the geometrical lattice. The phononic and photonic analogies of the QSHE are presented in parallel. The optimization constrains are evaluated to obtain the best configuration for the hybrid system. It is also presented the fabricated sample and the experimental limitations are revised.
- **Chapter 6** presents the analog of the quantum valley hall effect in a phononic crystal based in a hexagonall array of rounded triangles. Here it is evaluated the influence of the material anisotropy in topology. Numerical simulations of 3d Dirac cones are presented to illustrate how the change in the geometry lift this degeneracy and allows the construction of topological edge waveguides. Here it is also explored the geometrical limitations imposed by the size of the drilled scatters that causes strong linear diffraction of the incident light.
- **Chapter 7** Present a summary of the main conclusions and experimental achievements of this work. Based on it, it is also presented additional ideas that can be implemented using either the experimental technique, or the knowledge about the geometrical limitations, to evaluate the robustness of topological structures and prove phonon transport at hypersonic frequencies.

1.2 Thesis Publications

The experimental results with shamrock crystals and waveguides were summarized and published in one main article:

- Engineering nanoscale hypersonic phonon transport O. Florez, G. Arregui, M. Albrechtsen, R. C. Ng, J. Gomis-Bresco, S. Stobbe, C. M. Sotomayor-Torres and P. D. García. Nat. Nanotechnol. 17, 947–951 (2022).

I had also the opportunity to contribute in the book to celebrate the 100 years of Brillouin scattering. The contribution was for chapter 15:

- Electromechanical Brillouin scattering. Huan Li, Omar Florez, Bingcheng Pan, Guilhem Madiot, Clivia M Sotomayor Torres, Mo Li. Elsevier (2022).

There were other contributions to publications within the group:

- Excitation and detection of acoustic phonons in nanoscale systems. Ryan C Ng, Alexandros El Sachat, Francisco Cespedes, Martin Poblet, Guilhem Madiot, Juliana Jaramillo-Fernandez, Omar Florez, Peng Xiao, Marianna Sledzinska, Clivia M Sotomayor-Torres, Emigdio Chavez-Angel. Nanoscale 14 (37), 13428-13451 (2022).
- Optomechanical generation of coherent GHz vibrations in a phononic waveguide. Guilhem Madiot, Ryan C Ng, Guillermo Arregui, Omar Florez, Marcus Albrechtsen, Soren Stobbe, Pedro D Garcia, Clivia M Sotomayor-Torres. To be published in Phys. Rev. Lett.

Chapter 2

Brillouin scattering

2.1 Introduction

Leon Brillouin predicted theoretically in his doctoral thesis, back in 1920, that thermally generated sound waves in transparent media were capable of scattering incident light with a frequency shift. It was published as *Diffusion de la lumière et des rayons X par un corps transparent homogène. influence de l'agitation thermique* [32].This inelastic process is due to the time dependent refractive index grating induced by mechanical waves, leading to the generation of two new spectral components: Stokes and anti-Stokes. From a quantum point of view, it can be seen as the annihilation of a photon with frequency ω and the creation of a photon with frequency $\omega \pm \omega_{ac}$ mediated by the absorption or creation of a phonon with frequency ω_{ac}, as depicted in Figure 2.1(a).

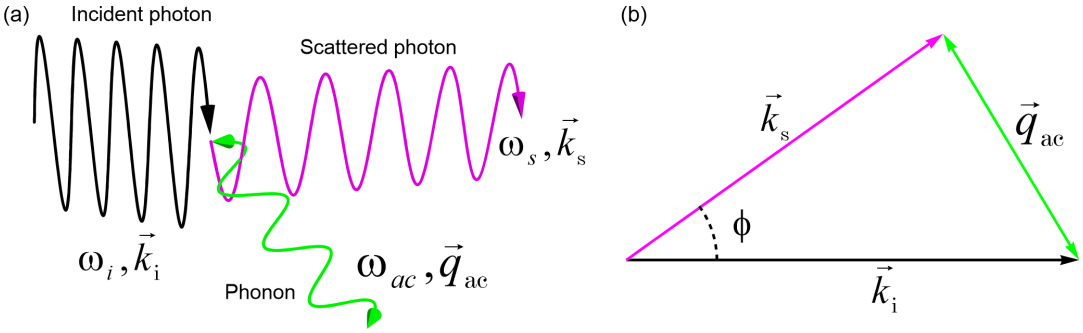

Figure 2.1: Representation of (a) Brillouin scattering process. (b) wave vectors in the Brillouin scattering process. ϕ is called the scattering angle. The mechanical wavevector has two arrowheads depending on if a phonon is absorbed or created during the scattering process.

In this inelastic process, energy and momentum are conserved. Considering the propagation direction of the incident and scattered light as shown in figure 2.1(b), the value of the mechanical wavevctor depends on the angle between incident and scattered light, an is at the minimum at $\phi = 0$ (forward scattering) and at the maximum at $\phi = \pi$ (backward scattering). These conservation rules determines the phase matching conditions for the scattering process.

2.2 Energy and momentum conservation: phase matching conditions

From the energy relation for bosons $E = \hbar\omega$, for the scattering process, energy conservation states that:

$$\omega_s = \omega_i \pm \omega_{ac}, \tag{2.1}$$

where ω_s, ω_i and ω_{ac} are the frequencies of the scattered photon, incident photon, and acoustic phonon respectively. The $\pm$ signs are due to the Doppler effect and indicate that the scattered light may be blue-shifted (+ sign, anti-Stokes), or red-shifted (− sign, Stokes). Stokes and Anti-Stokes processes are associated with heating or amplification, and quantum ground cooling [4, 5] of nanostructures, respectively. In the first case, the process gives vibrational energy (phonons) to the structure (heating), and in the second case, it is taken vibrational energy from the structure (cooling). From the momentum relation $\vec{P} = \hbar\vec{k}$, we have

$$\vec{k}_s = \vec{k}_i \pm \vec{q}_{ac}, \tag{2.2}$$

where $\vec{k}_s$, $\vec{k}_i$ and $\vec{k}_{ac}$ are the scattered, incident and mechanical wavevectors respectively. Each of these can be positive or negative valued depending on the propagation direction. The relation between ω and k for optical waves is given by

$$\omega_{i,s} = \frac{c}{n} k_{i,s}, \tag{2.3}$$

where c is the speed of light and n is the refractive index of the medium. For acoustic waves, in the case of long wavelengths compared to the interatomic distance, the relation between ω_{ac} and k is approximately linear [33], and can be expressed as

$$\omega_{ac} = c_{ac} q_{ac}, \tag{2.4}$$

where c_{ac} is the phase velocity of acoustic waves. considering the difference in order of magnitude between light velocity (c) and sound velocity (c_{ac}) and comparing equations 2.3 and 2.4, we have that $\omega_{ac} \ll \omega_{s,p}$. This implies that $\omega_s \approx \omega_p$ and $|k_s| \approx |k_i| = \omega_i n/c$. Then the vector magnitude in figure 2.1(b) is

$$q_{ac} \approx 2k_i \sin\frac{\phi}{2}. \tag{2.5}$$

This relation determines the phase matching condition for Brillouin scattering. For the particular cases of forward ($\phi = 0$) and backward ($\phi = \pi$) scattering, the relations are:

$$q_{ac} \approx 0 \longrightarrow \textit{forward Brillouin scattering}, \tag{2.6a}$$

$$q_{ac} \approx 2k_i \longrightarrow \textit{backward Brillouin scattering}. \tag{2.6b}$$

For $\phi = 0$, the Brillouin frequency shift approaches zero ($\omega_{ac} \approx 0$) and the forward Brillouin scattering in bulk is not allowed. However, sub-wavelength confinement in waveguides can lead to light interaction with transverse acoustic phonons, which makes forward scattering possible. Phase matching conditions for backward and forward scattering are summarized in figure 2.2 showing S and AS cases.

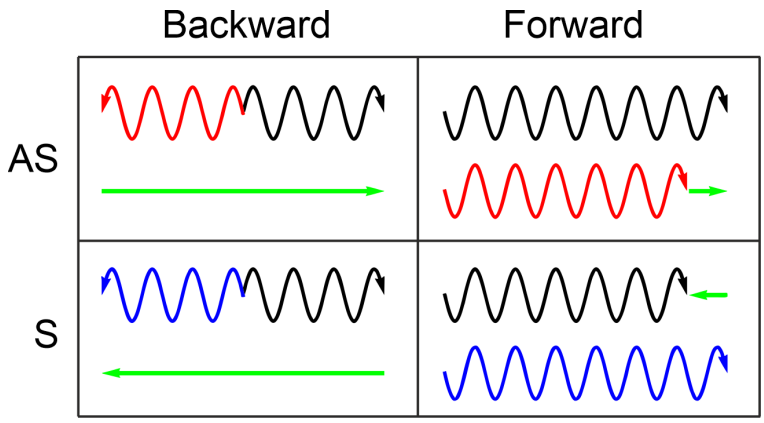

Figure 2.2: Backward and forward wavevectors for Stokes (S) and Anti-Stokes (AS) configurations. Black arrows represent incident light, blue and red arrows represent blue and red shifted scattered light respectively and green arrows represent the resulting mechanical wavevectors.

2.3 Refractive index perturbations

As Brillouin scattering arises from the periodic perturbation of the refractive index, the two main mechanisms responsible for this spontaneous perturbation are the photoelastic (PE) and moving boundary (MB) effects. The first one is induced by the elastic strain of the material and the second one is induced by displacement of the surface. A brief description of each one is given below. These perturbations originate from thermally exited phonons and therefore S and AS cases are equally likely in this stochastic process. The scattering can become stimulated if a high incident electric field contributes to the perturbation of the refractive index of the material by means of the electrostriction (ES) and radiation presure (RP) mechanisms. The former occurs when the light induces a mechanical strain field inside the material and the latter when the incident light contributes to increase the surface displacement; both effects are widely studied in optomechanical systems when phonons and photons are confined in small volumes enhancing their interaction. In the work presented here, as the system is not excited externally by means of high optical fields or another perturbation, all measurements are of spontaneous Brillouin scattering.

2.3.1 Photoelastic effect

When an acoustic mode propagates in a medium, there is an associated strain field. The strain results in a change of the refractive index. This is referred to as the elasto-optic or photoelastic effect [34, 35]. The acousto-optic interaction is used in a number of applications including light modulators, tunable filters, and spectrum analyzers, among others [36]. The relation between the dielectric perturbation $\Delta\varepsilon$ and the strain is given by

$$\Delta\varepsilon_{ij} = -\frac{\varepsilon_i \varepsilon_j}{\varepsilon_0} p_{ijkl} S_{kl}, \tag{2.7}$$

where P_{ijkl} is the elasto-optic (or photoelastic) tensor and S_{kl} is the strain tensor. Considering the crystallographic orientation of silicon in standard SOI wafers, the

elasto-optic tensor in Voigt notation is

$$p = \begin{pmatrix} p'_{11} & p'_{12} & p_{12} & 0 & 0 & 0 \\ p'_{12} & p'_{11} & p_{12} & 0 & 0 & 0 \\ p_{12} & p_{12} & p_{11} & 0 & 0 & 0 \\ 0 & 0 & 0 & p_{44} & 0 & 0 \\ 0 & 0 & 0 & 0 & p_{44} & 0 \\ 0 & 0 & 0 & 0 & 0 & p'_{66} \end{pmatrix}, \tag{2.8}$$

where $p'_{11} = (p_{11} + p_{12} + 2p_{44})/2$, $p'_{12} = (p_{11} + p_{12} - 2p_{44})/2$, $p'_{66} = (p_{11} + p_{12})/2$. The coefficients for silicon at 532 nm are $p_{11} = -0.1203$, $p_{12} = -0.0223$ and $p_{44} = -0.045$ [37].

2.3.2 Moving boundary effect

When the interface between two different materials is displaced, the volume originally occupied by one material is occupied by the other and vice versa. This leads to a change in the refractive index over a very small area.This is known as the moving boundary effect [38]. This effect is proportional to the displacement field at the surface and to the difference between the dielectric constants of the materials on both sides of the interface. For the continuous components of the electric field at the interface, the perturbation $\Delta\varepsilon$ is the difference of dielectric constants ε

$$\Delta\varepsilon_{12} = \varepsilon_1 - \varepsilon_2. \tag{2.9}$$

For the discontinuous components of the electric field at the surface, the perturbation $\Delta\varepsilon$ is the harmonic mean value of ε:

$$\frac{1}{\Delta\varepsilon_{12}} = \frac{1}{\varepsilon_1} - \frac{1}{\varepsilon_2}. \tag{2.10}$$

As the difference in orders of magnitude between optical frequencies (THz) and mechanical frequencies (GHz), the optical wave interact with a deformed but static medium. The total induced effect on the optical field can be calculated by decomposing the period T of the mechanical wave into a entire number of frames n, separated in time by T/n. The MB effect becomes important in sub-wavelength confinement of light by e.g. silica nanowires [39] or silicon waveguides [40], as a large amount of light is on the surface of the structure and this light can feel the displacement of the surface. When light directly strikes the surface, as in our case, all the incident light can interact with the mechanic displacement field on the surface.

2.4 Brillouin light scattering spectroscopy

When coherent light with a wavevector $\vec{k}_i$ hits the surface of a medium with a certain angle θ as shown in figure 2.3, part of this incident light is linearly reflected ($\vec{k}_r$), and another small part is non-linearly scattered by the two different mechanisms described in the previous section. First it is considered a transparent material as shown in figure 2.3(a). In this case, the incident light is refracted into the material with a wavevector $\vec{k}_R$. As the light propagates within the material, it is nonlinearly scattered as density fluctuations in the material, indicated by different colors in figure 2.3 (PE effect).

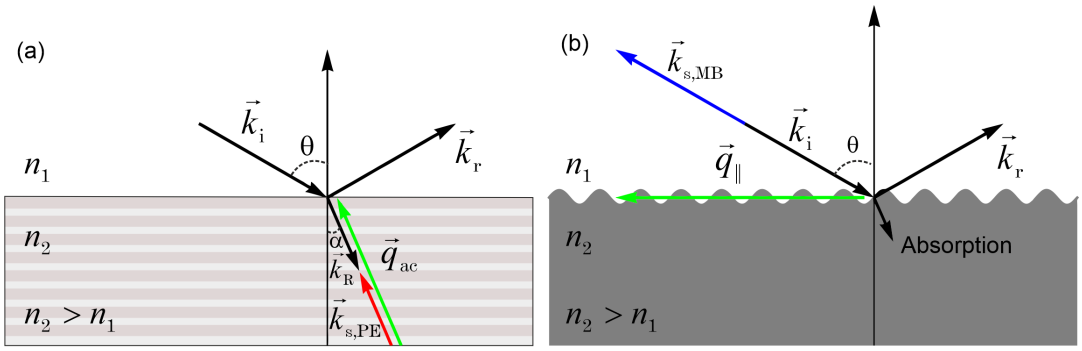

Figure 2.3: Phase matching conditions for (a) photoelastic and (b) moving boundary perturbations. The change of color inside the material in (a) indicates density fluctuations that locally changes the refractive index. Corrugation at the interface in (b) denotes the boundary displacement that dinamically changes the refractive index at the interface. Green arrows denote the mechanic wavevectors in each case.

The relation between k_i and k_R can be extracted from the momentum conservation for the parallel component as follows

$$k_i \sin\theta = k_R \sin\alpha. \tag{2.11}$$

This equation result on $k_R = k_i \frac{\sin\theta}{\sin\alpha}$. From Snell's law we have that $n_1 \sin\theta = n_2 \sin\alpha$. Replacing Snell's law into equation 2.11 finally gives that $k_R = k_i \frac{n_2}{n_1}$. The backscattered component $\vec{K}_{s,PE}$, follows the inverse path of $\vec{k}_R$ and is refracted back into the air, $\vec{k}_{s,PE}$ with the same angle θ. As a result, the phase matching condition for scattering arising from the PE effect, is $\vec{q}_{ac} = \vec{k_R} + \vec{k}_{s,PE} = 2\vec{k}_R$. After replacing k_R, it is obtained that

$$\vec{q}_{ac} = 2\frac{n_2}{n_1}\vec{k}_i. \tag{2.12}$$

Now it is considered the case of an opaque material as shown in figure 2.3(b). In this case, light is absorbed and can not penetrate deeper into the material. One small part is nonlinearly scattered by thermally excited phonons on the surface (MB effect) in all directions. Once again, we are interested in the backscattered signal $\vec{k}_{s,MB}$. Given the absorption in the material, momentum conservation in the perpendicular direction to the surface is not fulfilled; therefore momentum is only conserved in the parallel direction to the surface (in-plane component). For the backscattering configuration, the phase matching condition for the in-plane component, $\vec{q}_{\parallel}$ in figure 2.3(b), is:

$$k_{ac} = 2k_i sin(\theta). \tag{2.13}$$

In summary, phase matching conditions for PE and MB mechanisms can be written as:

$$q_{ac} = n\frac{4\pi}{\lambda} \longrightarrow for\ PE\ effect, \tag{2.14a}$$

$$q_{\parallel} = \frac{4\pi}{\lambda} sin(\theta) \longrightarrow for\ MB\ effect, \tag{2.14b}$$

where $n_2 = n$, $n_1 = n_{air} = 1$, and $k_i = 2\pi/\lambda$, where λ is the wavelength of the incident light. By changing the incident angle θ, it is possible to probe the mechanical wavevector for excitations arising in the surface and reconstruct the band diagram

of the illuminated sample. On the other hand, scattering arising inside the material does not depend on the incident angle and always will have the same mechanical wavevector k_{ac}, which only depends on the incident wavelength. The contribution of each effect depends on different factors like the transparency and geometry of the material. The reconstruction of acoustic band diagrams using the nonlinearly scattered light is known as Brillouin Light Scattering (BLS) spectroscopy. This is a non invasive and non destructive technique that allows for the characterization of opaque and thin film materials, and periodic structures as nanoscale phononic crysyals, studied in this work. The device used to resolve and increase the contrast of the weak scattered signal is known as a Tandem Fabry-Perot interferometer [41].

2.4.1 Tandem Fabry-Perot interferometer

To achieve sufficiently high resolution for a Brillouin scattering measurement, a Tandem Fabry-Perot (TFP) interferometer, shown in figure 2.4, is used as a scanning spectrometer. A single FP interferometer consists of two parallel flat mirrors separated by a variable distance L. The cavity transmits light of wavelength λ if the spacing is $L = m\lambda/2$, where m is an integer. The cavity acts as a tunable near-unity narrow spectral range bandpass filter.

In measurements where the linearly scattered signal exceeds the intensity of the nonlinearly scattered signal by orders of magnitude, like backscattering measurements on opaque materials, it is necessary to increase the contrast (ratio between maximum and minimum signal) of the system. The contrast of an interferometer may be increased by placing two or more interferometers in series. In addition, multiple passes through the same interferometer also helps to enhance the signal. The introduction of multipass interferometers enables Brillouin scattering experiments to detect surface vibrations both in transparent and opaque materials. Simultaneously, the combination of two interferometers leads to an increase in the Free Spectral Range (FSR) of the resulting interferometric system. For these reasons, choosing a multipass tandem Fabry-Perot interferometer is the most suitable system to measure the vibrational frequencies of the nanostructures studied in this work.

It is worth noting that spacial care needs to be taken in maintaining the stability of the system. Stability at least of 5Å (fluctuation of cavities), is required over the entire measurement duration which may be several hours when recording weak signals [42]. In the TFP shown in figure 2.4, the scattered light passes three times through the first cavity before passing an additional three times through the second cavity. Subsequently, the enhanced scattered signal reaches the detector and can be resolved.

2.4.2 Experimental setup

The free space setup that is used to detect the mechanical vibration of membranes and nanostructured patterned samples or phononic crystals is shown in fig. 2.5. The light source is a continuous wave (CW) 532 nm wavelength narrow green laser from Coherent (Verdi V10) with variable output power up to 10 W. One small part of the light, represented with the green dashed line, is taken as a reference for the TFP system. The beam is recollimated to reduce the beam size before reaching a $\lambda/2$ waveplate (WP) that controls the polarization of the incident beam. After that, light passes through a beam splitter (BS) that reflects 10% of the power to the objective

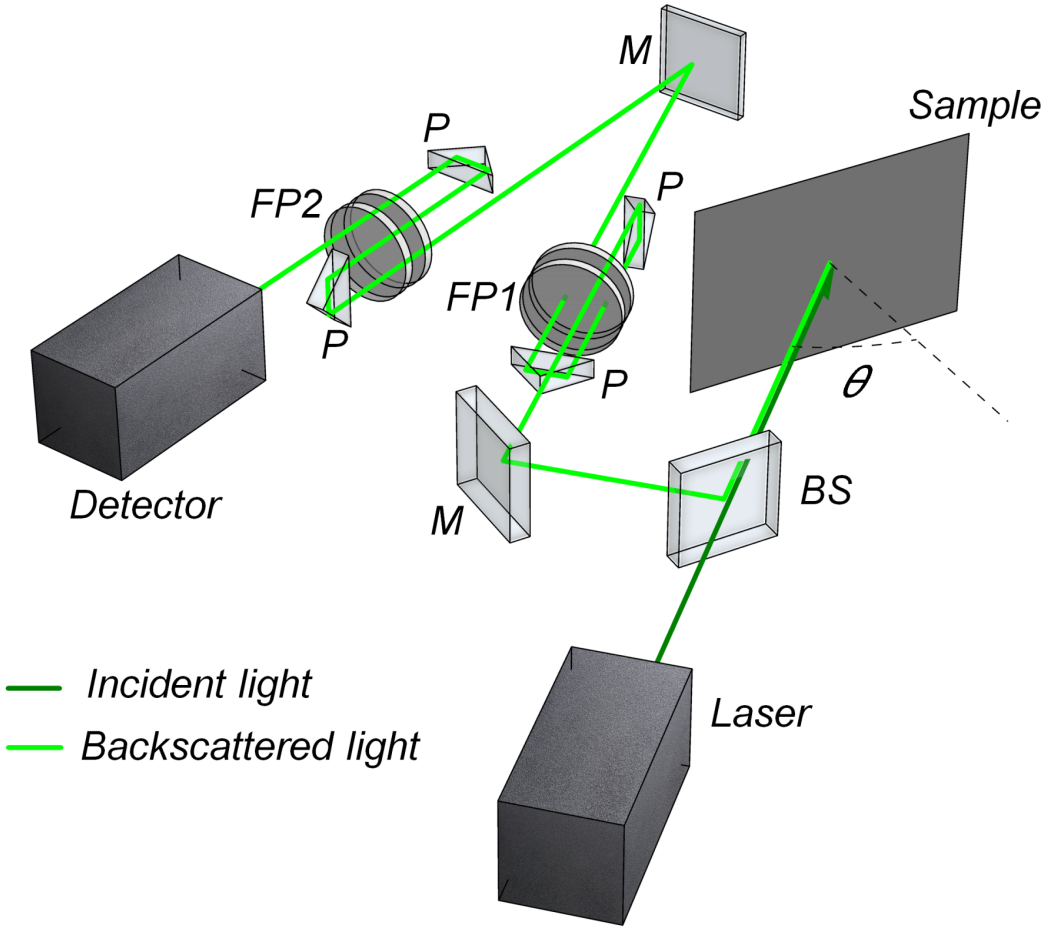

Figure 2.4: Scheme of the tandem Fabry-Perot interferometer. θ is the angle of incidence. BS=beam splitter, M=mirror, P=prism and FP=Fabry-Perot cavity.

(Ob) and transmit 90% of the light that is used to monitor the incident power reaching the sample (S).

The objective has the ability to simultaneously illuminate the sample with incident light while also collecting the backscattered signal, represented in red. The light is routed through the beam splitter and mirrors to reach a second $\lambda/2$ waveplate that controls the polarization of the scattered light. Finally the scattered beam is focused for the lens (L) to pass through the incident pinhole of the TFP system. The sample is placed on top of a motorized rotation stage that accurately controls the angle between incident light and the surface of the sample. Due to the long acquisition time of measurements and the required precision in angle rotation, the measurement system was automatized, integrating the rotation stage with the acquisition software of the TFP system (GOSTH), allowing for autonomous measurements. It was implemented in a user friendly interface made in LabVIEW.

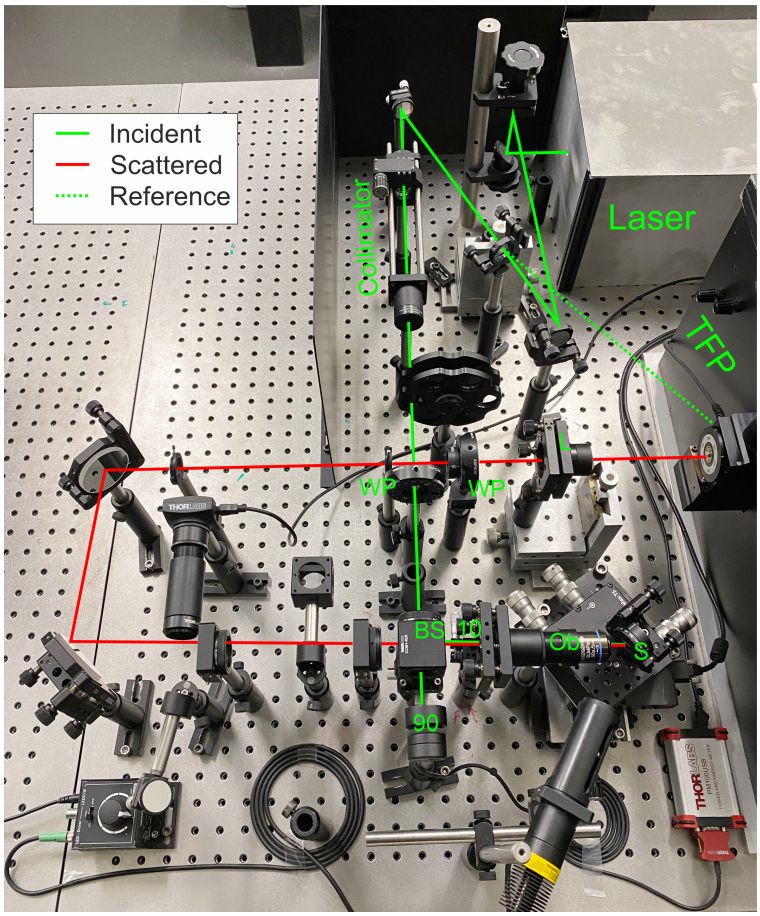

Figure 2.5: Experimental setup for Brillouin light scattering measurements. Green, red and green dashed lines represents the incident, scattered and reference light respectively. WP = waveplate, BS = beam splitter, Ob = Objective, L = Lens, S = sample

2.5 Experimental and numerical validation: Fully released silicon membrane

Fully released membranes are a good platform to test and calibrate our experimental setup. Figure 2.6 shows the measured spectrum in a fully released silicon membrane (from NORCADA) with a thickness of 250 nm, measured at an angle of 30 degrees. The strong central peak corresponds with the elastic Rayleigh scattering and the spectrum is symmetric because of Stokes and anti-Stokes contributions. The y axis indicates the intensity of scattered peaks. The system counts the number of photons with slightly different frequency that sets the amplitude (signal to noise ratio, SNR) of measured spectra. The amplitude is given in arbitrary units because it depends on the acquisition time. A longer time will increase the SNR of each peak but will also increase the background of the entire spectrum. Therefore long acquisition times will not necessarily result in a better SNR in measurements, as the measurement will stabilize after certain time.

The spectrum shows four peaks whose frequencies correspond with the different vibrational modes for this particular thickness. To analyze the data, each peak is fitted with a Lorentzian shape to obtain its central frequency and then positive and negative frequencies are averaged. Replicating this process for different incident angles

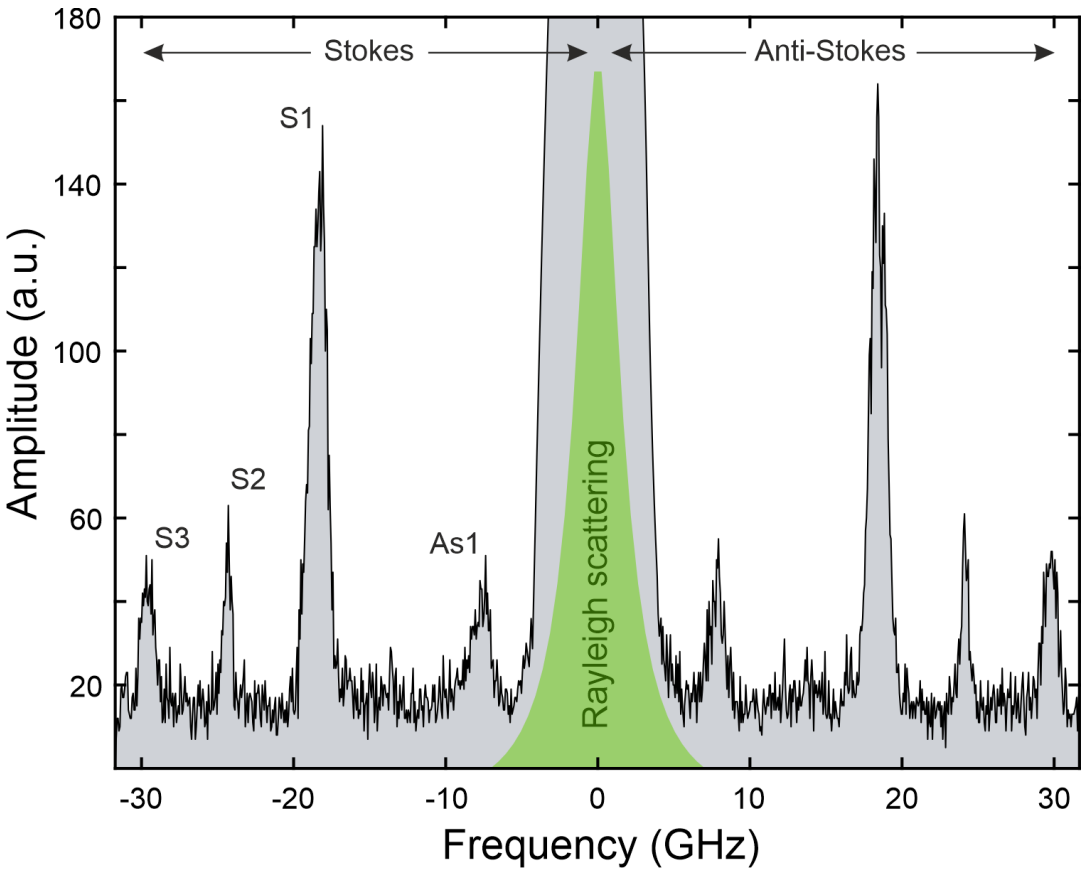

Figure 2.6: Measured spectrum for the fully released silicon membrane with a 30 degrees incidence angle.

allows for experimental reconstruction of the band diagram. Figure 2.7(a) shows the phononic dispersion relation for the silicon membrane with 250 nm of thickness calculated with finite element method (FEM) using COMSOL multiphysics software. The elastic equation and the periodic conditions used to find this band diagram will be discussed with more detail in the next chapter. Blue and red curves represent symmetric and asymmetric modes with respect to the mid plain (parallel to half of the thickness) of the membrane.

Black curves represent shear (SH) waves which does not provoke surface deformation and therefore can not be detected in the BLS measurements. The black points represent the measured frequencies for different angles and the vertical dotted line indicates the position of the frequencies shown in figure 2.6. The measurements were taken from 5 to 60 degrees with a step angle of 5 degrees with the same incident power and the same acquisition time of 210 minutes. The modes are labeled as Asn and Sn with $n = 1,2,3$ and peaks in figure 2.6 can be identified. The frequency of the modes changes with the angle and therefore the scattering process here is dominated by the MB mechanism. The x axis in figure 2.7(a) is given in degrees but can be easily changed to the wavevector using the equation 2.14b.

The phononic dispersion relation of the membrane can be modified by changing the thickness. Figure 2.7(b) shows the change in frequency for the first three symmetric and asymmetric modes as a function of the thickness calculated for a wavevector $q = \frac{4\pi}{\lambda} \sin 30$, the same position indicated with the dashed line in figure 2.7(a). As the thickness decreases, the frequency of the of the modes increases substantialy

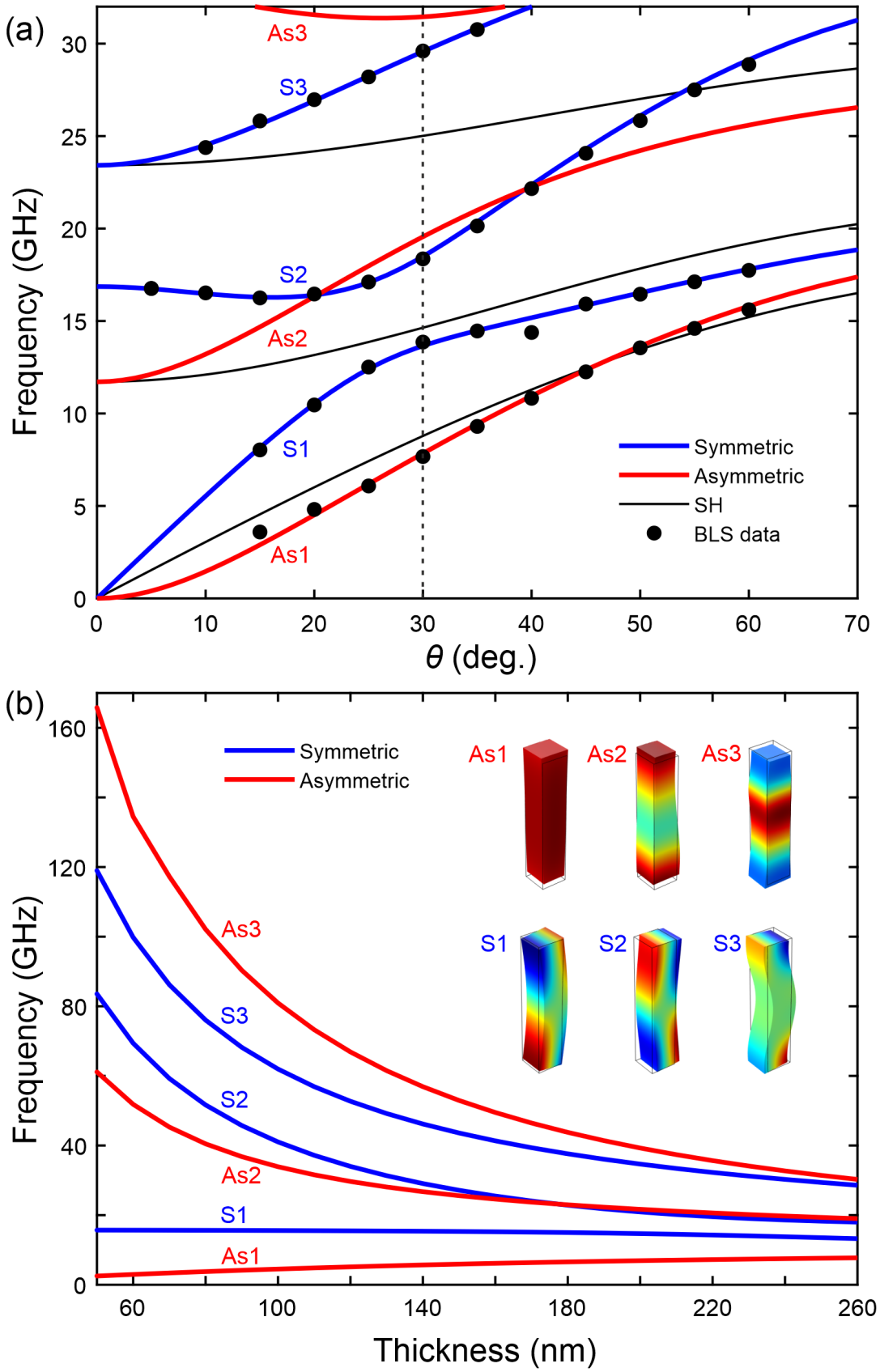

Figure 2.7: (a) Measured and simulated vibrational modes for a silicon membrane with a thickness of 250 nm. (b) Evolution in frequency for the first three symmetric and asymmetric modes as a function of thickness. The inset shows the mode profile of these modes.

except for the first mode of each family. The first asymmetric mode decreases in frequency while the first symmetric mode remains constant. The inset of the figure shows the mode profile of these modes.

2.6 Brillouin scattering efficiency

The scattering efficiency quantifies how much a mechanical mode scatters the incident light. To calculate it, we need to consider the origin of the periodic perturbation of the refractive index. It is caused by the two different mechanisms explained before, the MB and PE effects. Here we made a first approximation taking into account only the MB perturbation and neglecting the PE contribution, given the small volume of interaction in our experiments given the direction of the incident light, in the plane perpendicular to the measured samples; and also considering the small thickness (220 nm -250 nm) of the studied samples. This approximation allows us to obtain the coupling coefficients in an almost fully analytical way. According to [38], the MB coupling is given by:

$$\kappa_{mb} = \int_A U_z \left[\Delta\epsilon_{12}\left(\mathbf{E}^*_{s,\parallel}\cdot\mathbf{E}_{i,\parallel}\right) - \Delta\epsilon_{12}^{-1}\left(\mathbf{D}^*_{s,\perp}\cdot\mathbf{D}'_{i,\perp}\right)\right] dA \tag{2.15}$$

where U_z is the normal displacement to the surface A as indicated in Fig. 2.8(a). $\Delta\epsilon_{12} = (\epsilon_1 - \epsilon_2)$ and $\Delta\epsilon_{12}^{-1} = (\epsilon_1^{-1} - \epsilon_2^{-1})$, $\mathbf{E}$ and $\mathbf{D}$ are electric and displacement fields, and scripts s and i denote scattered and incident fields respectively. Taking into account the relation between the relative permittivity and the refractive index, $\epsilon = \epsilon_0 n^2$, we can write

$$\Delta\epsilon_{12} = \epsilon_0(n_1^2 - n_2^2) \tag{2.16a}$$

$$\Delta\epsilon_{12}^{-1} = \frac{1}{\epsilon_0}\left(\frac{1}{n_1^2} - \frac{1}{n_2^2}\right). \tag{2.16b}$$

Replacing the normal component of the displacement field by the electric field component, $\mathbf{D} = \epsilon\mathbf{E}$, we can rewrite Eq. 2.15 as

$$\kappa_{mb} = \int_A U_z\epsilon_0\left[\left(n_1^2 - n_2^2\right)\left(\mathbf{E}^*_{s,\parallel}\cdot\mathbf{E}_{i,\parallel}\right) - n_2^4\left(\frac{1}{n_1^2} - \frac{1}{n_2^2}\right)\left(\mathbf{E}^*_{s,\perp}\cdot\mathbf{E}'_{i,\perp}\right)\right] dA. \tag{2.17}$$

The incident and scattered electric field in the sample surface can be treated as planes waves propagating in free space and can be written as:

$$\mathbf{E}_i(r,t) = \frac{1}{2}\mathbf{E}_i(x,y)e^{-i(\omega_i t - \mathbf{k}_i\cdot\mathbf{z})} + c.c. \tag{2.18a}$$

$$\mathbf{E}_s(r,t) = \frac{1}{2}\mathbf{E}_s(x,y)e^{-i(\omega_s t + \mathbf{k}_s\cdot\mathbf{z})} + c.c. \tag{2.18b}$$

We need to account for the polarization of the electric field used in the experiment (TM polarization) as depicted in Fig. 2.8. For the backward Brillouin scattering configuration, $\vec{k}_s = -\vec{k}_i$ and $\omega_s = \omega_i \pm \Omega$ or $\omega_s \approx \omega_i$ given the small frequency of mechanical modes (GHz) compared with the incident light frequency (THz). $\mathbf{E}_s(x,y) = \mathbf{E}_i(x,y) = \mathbf{E}_i$ because light is propagating in free space. Therefore the product of the incident and scattered fields can be simplified to $\mathbf{E}_s^*\cdot\mathbf{E}_i = E_i^2$. Incident and scattered light can then be treated as the same fields.

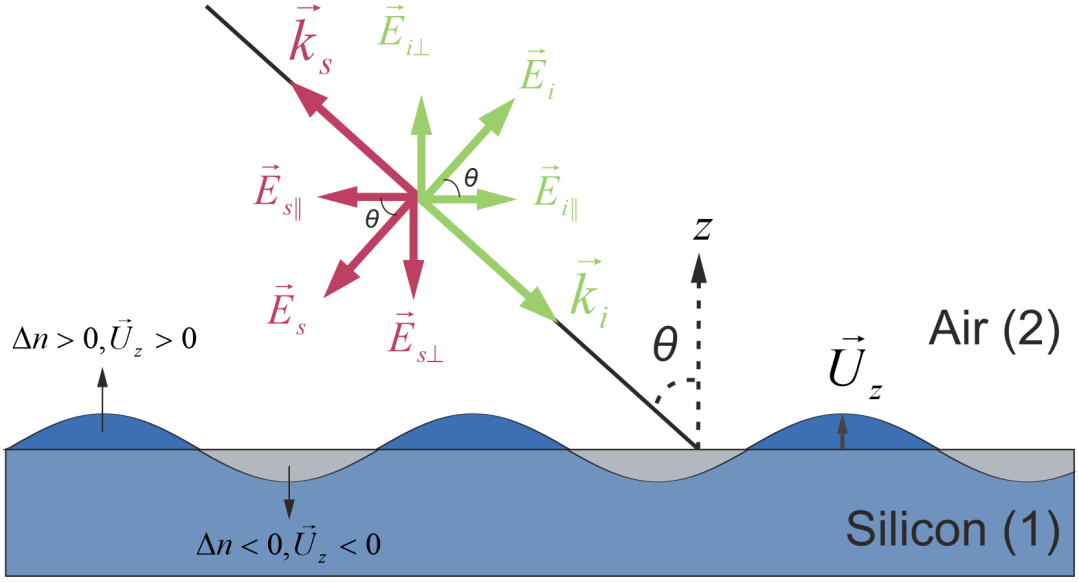

Figure 2.8: Components of the incident and backscattered electromagnetic field (green and red respectively). Each mode of the structure leads to a particular vertical displacement of the surface that determines the scattering contribution.

From figure 2.8(a), we have $\mathbf{E}_{s,\parallel} = -\mathbf{E}_{i,\parallel}$ and $\mathbf{E}_{s,\perp} = -\mathbf{E}_{i,\perp}$, where the parallel and perpendicular components of electric field are given by $\mathbf{E}_{i,\parallel} = \mathbf{E}_i \cos\theta$, and $\mathbf{E}_{i,\perp} = \mathbf{E}_i \sin\theta$. Replacing all these expressions in Eq. 2.17, we can write

$$\kappa_{mb} = \int_A U_z \epsilon_0 \left[\left(n_1^2 - n_2^2\right) \left(-E_i^2 \cos^2\theta\right) - \left(n_2^2 - n_1^2\right) \frac{n_2^2}{n_1^2} \left(-E_i^2 \sin^2\theta\right) \right] dA. \quad (2.19)$$

The entire expression inside brackets can be taken out the integral. We only need to account for the change of the refractive index with respect to the surface displacement. To do so, we always assume a positive change of the refractive index and take the absolute value of the normal displacement $\mathbf{U}_z$.

$$\kappa_{mb} = -\epsilon_0 E_i^2 \left(n_1^2 - n_2^2\right) \left[\cos^2\theta + \frac{n_2^2}{n_1^2} \sin^2\theta\right] \int_A |U_z| dA. \quad (2.20)$$

Here the coupling coefficient does not depend on the incident field and it can be normalized to $E_i^2 = 1W$. Each mechanical mode has its own scattering efficiency depending on the surface displacement U_z. The bigger the refractive index contrast, the bigger the MB contribution. Finally, the scattering cross section needs to be accounted for. The illuminated area on the sample surface changes with the angle, being a circle of area $A_c = \pi b^2$ for $\theta = 0$, where b is the beam diameter, and an ellipse with axes b and $l = b/cos(\theta)$, and area $A_e = \pi bl$ for a certain angle θ. Therefore, Eq. 2.20 needs to be divided by $cos(\theta)$ to account for the scattering cross section. Finally, replacing $n_1 = n_{si}$ and $n_2 = 1$, the coupling coefficient for the MB perturbation is given by

$$\kappa_{mb} = -\epsilon_0 E_i^2 \left(n_{Si}^2 - 1\right) \left[\cos\theta + \frac{1}{n_{Si}^2} \tan\theta \sin\theta\right] \int_A |U_z| dA. \quad (2.21)$$

The integral area depends on the structure in which the scattering efficiency have to

be calculated. In the case of the membrane, the integration area is the top square of the unit cell presented in the inset of figure 2.7. Although the expression presented here does not account for the PE contribution, it is a good approximation to determine if a particular mechanical mode can be detected in our experimental setup.

2.7 Conclusions

In this chapter has been defined the theoretical basis for the Brillouin scattering process, as well as the experimental setup description. The main conclusions are summarized below

- Despite the fact that forward Brillouin scattering is forbidden in bulk, tight confinement of mechanical waves in waveguides make it possible because the existence of transverse phonons. These mechanical modes will be standing waves ($q_a c \approx 0$) to fulfill the phase matching condition for forward scattering.
- BLS spectroscopy is a non-destructive technique that allows the experimental phononic band reconstruction in nanostructures.
- Brillouin scattering arising from the PE mechanism will have the same frequency no matters the incident angle of light. Scattering arising from MB mechanism can be mapped with the change of the incident angle. It can be a easy way to identify the dominant mechanism in the scattering process for different structures.
- The experimental reconstruction of the dispersion relation for a suspended membrane is an effectively way to validate the experimental setup and FEM simulations simultaneously. The measurements take few time compared with more intricate structures; besides that, modes are fairly far apart in frequency, making them easy to identify.

Chapter 3

Phononic crystals

3.1 Introduction

The mechanical dispersion relation of a 2D membrane such as the one presented in the previous chapter can be strongly modified by including periodic patterns (i.e., scatters) in the membrane. These periodic materials are called phononic crystals, as the counterpart of photonic crystals which modulate the refractive index of the material to modify the photonic band structure. The same periodic material can simultaneously modify the phononic and photonic dispersion relation. These are known as optomechanical crystals or phoxonic crystals [11, 43–45]. The ability to control and modify the acoustic properties in a periodic matrix makes them suitable for many applications where mechanical vibrations at the nanoscale play the main role. By exploiting electron-beam lithography of semiconductor materials and carefully designing the size and shape of the patterned structure, it is possible to produce band gaps in the entire Brillouin zone. The introduction of controlled defects to create waveguides and cavities with the goal of confining and guiding acoustic waves is the origin of the potential application of phononic and photonic crystals, which is only possible when a full gap already exist in the underlying crystal pattern. Here I present experimental evidence of a complete mechanical gap in the GHz regime for a *shamrock* phononic crystal measured using the non-invasive Brillouin light scattering spectroscopy technique. This geometry also presents a full gap for TE photons in the THz range. Therefore this structure is an optomechanical crystal.

3.2 Phononic crystals

The periodical distribution of the mass in a system allows to engineer the mechanical modes of the structure and open frequency windows over which the destructive interference of scattered waves forbids any wave propagation. This characteristic of phononic crystals allows different applications such as tunable filters, mechanical isolators, thermal management [10] and the most importantly, the routing and confinement of mechanical waves at the mesoscale [11]. The two different physical mechanisms that enable the creation of phononic band gaps are Bragg scattering [33] and local resonances [46]. For Bragg scattering, a stronger wave velocity mismatch contributes to the formation of broader band gaps due to stronger wave scattering at the interfaces. In the case of local resonances, band gaps form due to localized excitation at the resonant frequencies, which are considered independent of periodicity. The combination of these two mechanisms provides a way to design phononic crystals with simultaneously wide and robust band gaps [47].

Figure 3.1: "Órgano" sculpture by Eusebio Sempere (1977), located at the entrance of the Juan March foundation in Madrid. Photo taken from *https://vanguardiaartisticasigloxx.wordpress.com*.

One particular case of band gaps at the macro scale is the "Órgano" sculpture by Eusebio Sempere (1977), located at the entrance of the Juan March foundation in Madrid (figure 3.1). By sccidental design, this sculpture formed by holed stainless-steel circular bars with a diameter of 2.9 cm in a rectangular array with a periodic separation of 10 cm, can attenuate the sound (KHz) for a certain range of frequencies [8]. The same idea is applied at the nanoscale to form periodic structures often known as hypersonic phononic crystals [9] with vibrational frequencies ranging from 1 GHz to 1 THz. Unlike sonic and ultrasonic waves whose generation usually relies on external stimuli, acoustic waves at hypersonic frequencies can be formed simply by random thermal motion of the atoms of the material, and these high-frequency thermally exited acoustic waves are often referred to as phonons [19]. It is possible to design the intrinsic vibrational frequencies of the materials and create a range of frequencies over which not even thermal motion exists. This has interesting applications such as in the study of optomechanic organic molecular systems [48], in which environmental phonons represents a source of noise which limits vibration of the system under study.

There are few existing examples of fabricated or measured structures presenting gaps in the GHz range. The first experimental measurement of a gap at such frequencies was in colloidal crystals where it was possible to detect a gap of 400 MHz around 5GHz but just for a particular direction in the Brillouin zone [19]; meaning that this is only a partial gap. Aditionally, the assembly of such structures requires the collective alignment of small spheres, making the structure more sensitive to disorder and imperfections that strongly modifies the band structure of the system. Another important example is the snowflake crystal [49, 50] which simultaneously presents a

full gap for GHz phonons and THz photons (optomechanical crystal). This geometry fabricated in silicon on insulator (SOI) platform, was used to build optomechanic cavities in the GHz range. Up to date, there is not explicit measurements of a full mechanical gap for hypersonic frequencies. Here we will present the shamrock crystal, a simple pattern robust to fabrication fluctuations that presents simultaneous gaps for photons and phonons. This structure is fabricated in SOI platform that allows the implementation of complementary metal oxide semiconductor (CMOS) fabrication techniques and enables the integration with electronic and photonic circuits.

3.3 Shamrock geometry

Inspired by the properties of another crystal built upon shamrocks formed by overlapping ellipses [51], we consider an even simpler geometry that still retains the desired mechanical properties. We aim at exploring a design in which the unit cell building block is formed by three overlapping circles. The geometry of this phononic crystal makes it more robust against parameter-noise fluctuations during the fabrication process. The projected geometry is depicted in figure 3.2. It consists of three tangential circles of radius r, shifted by a distance $f = 2r/\sqrt{3}$ from the common center. Three small semicircles of radius $f - r$ have been added in the junctions to smooth out any sharp corners in the geometry and create a simpler pattern for fabrication.

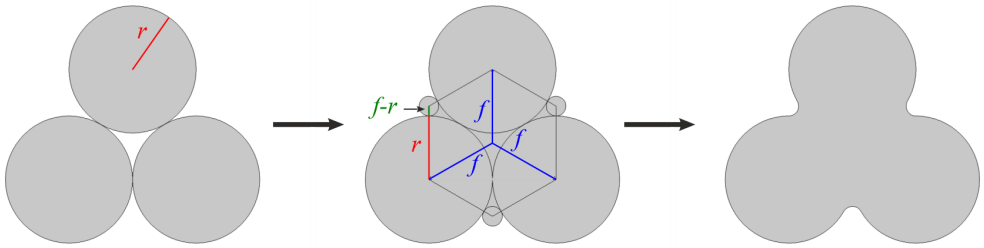

Figure 3.2: Three circles touching each other form the basis of the shamrock geometry (left). Small circles are placed in the adjacent junctions of circles to avoid sharp corners (center). Final feature of the shamrock that will be replied to form the crystal (right).

The crystal is formed by a triangular lattice with periodic distance a, as showns figure 3.3(a). The radius of each circle is parametrized as a function of the lattice period a, $r = na$ where n is a scalar going up to 0.25 which is the limiting case when every shamrock touches one another. The final unit cell is shown in figure 3.3(b) where t is the membrane thickness and the blue and red arrows indicate the two Floquet periodic conditions (applied to the indicated faces) used in simulations that will be discussed later in this chapter.

3.3.1 Irreducible Brillouin zone

The Irreducible Brillouin Zone (IBZ) of a periodic structure is determined by the type of lattice (e.g., square, triangular, etc), the symmetries of the repeated pattern, and the intrinsic properties of the material. The first Brillouin zone of a triangular lattice such as that presented in figure 3.3(a), is determined by a hexagon with side $4\pi/3a$, where a is the period of the structure [33]. If the phononic crystal is formed

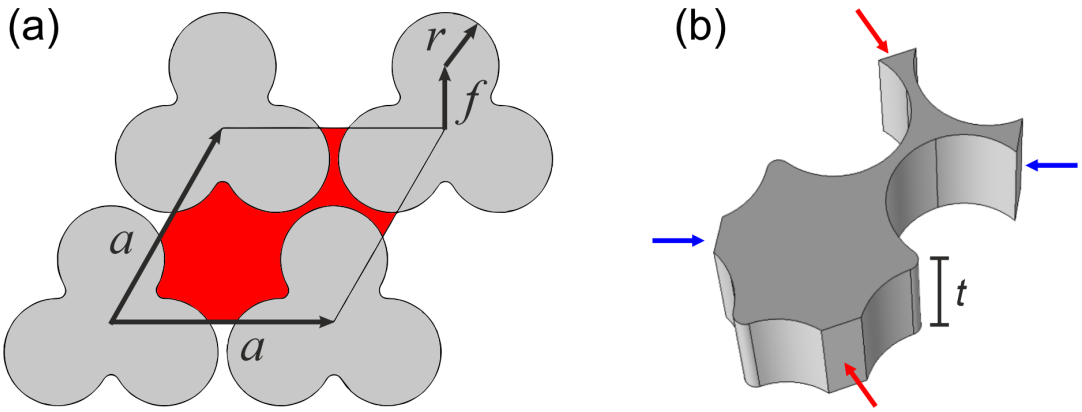

Figure 3.3: (a) Shamrock unit cell in the triangular lattice with the period of the structure a. (b) 3D shamrock unit cell indicating the thickness of the membrane t, and the faces where the Floquet periodic conditions are applied for simulation.

by shamrocks (that has a C_3 rotational symmetry) in an isoptropic material, the IBZ is determined by 1/12th of the first BZ as indicated by the region bounded by the $\Gamma KM\Gamma$ path in figure 3.4(a). Rotational symmetry of order n, C_n, means that rotation by an angle of $360°/n$, does not change the object. If the crystal is formed by squares (which have C_4 rotational symmetry) in the same isotropic material, the IBZ is determined by a quarter of the first BZ as shown by figure 3.4(b). However, if we consider the anisotropy of the material (as is the case for crystalline silicon), the IBZ for the shamrock crystal is now defined by the region bounded by the $\Gamma KLY\Gamma$ path described in figure 3.4(c).

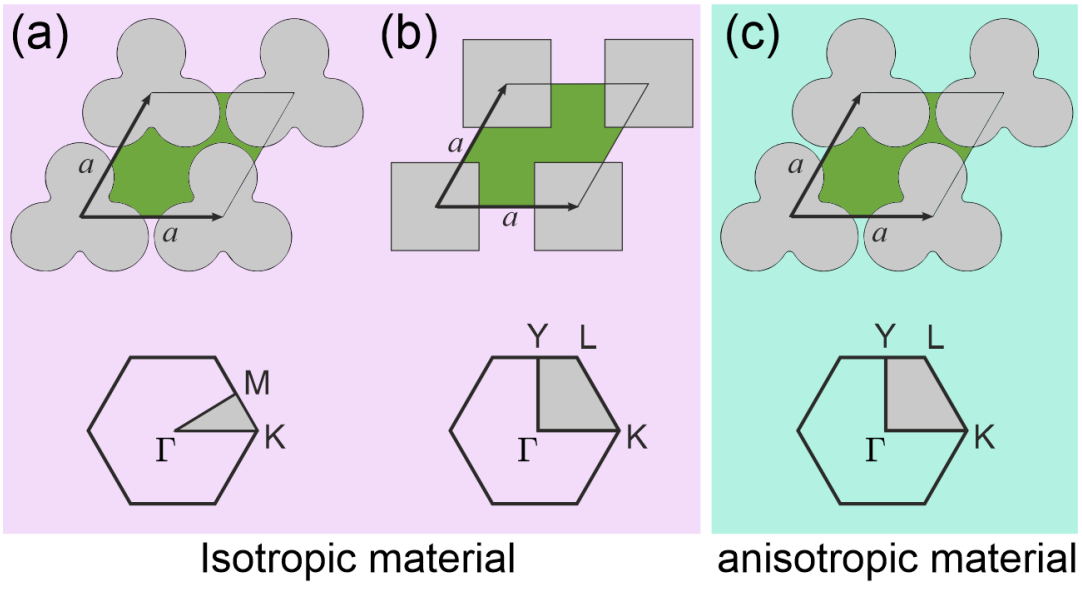

Figure 3.4: Irreducible Brillouin zone for a triangular lattice composed of (a) shamrocks (which have C_3 rotational symmetry) and (b) squares (wich have C_4 rotational symmetry), considering that the crystal is made in an isotropic material. (c) Irreducible Brillouin zone for shamrock crystal considering the anisotropy of the material.

The shamrock crystals were fabricated in the SOI platform. The density of silicon used for simulation is 2331 kg/m^3. Depending on the crystallographic orientation,

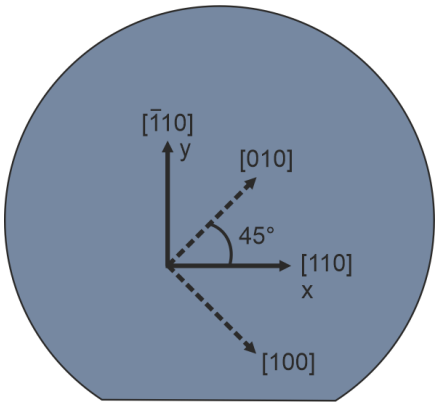

Figure 3.5: Miller index for the SOI wafer used in samples fabrication

the elastic matrix for silicon varies. For the [100] (x) and [010] (y) orientation, the elastic matrix is completely defined by the three coefficients C_{11} = 165.7 GPa, C_{12} = 63.9 GPa and C_{44} = 79.9 GPa. Considering the orientation of crystalline silicon presented in figure 3.5, in which [110] orientation coincides with x axis, the elastic matrix with coeficients C'_{ij} is given by:

$$\begin{pmatrix} 194.7 & 34.9 & 63.9 & 0 & 0 & 0 \\ 34.9 & 194.7 & 63.9 & 0 & 0 & 0 \\ 63.9 & 63.9 & 165.7 & 0 & 0 & 0 \\ 0 & 0 & 0 & 79.9 & 0 & 0 \\ 0 & 0 & 0 & 0 & 79.9 & 0 \\ 0 & 0 & 0 & 0 & 0 & 50.9 \end{pmatrix} GPa, \tag{3.1}$$

where $C'_{11} = C'_{22} = (C_{11} + C_{12} + 2C_{44})/2$, $C'_{33} = C_{11}$, $C'_{44} = C'_{55} = C_{44}$, $C'_{66} = (C_{11} - C_{12})/2$, $C'_{12} = (C_{11} + C_{12} - 2C_{44})/2$ and $C'_{13} = C'_{23} = C_{12}$.

3.3.2 Band structure for the IBZ contour path

The plane wave propagation in infinite two-dimensional periodic structures can be studied using Floquet-Bloch principles. In simple terms, Bloch's theorem (or Floquet's principle in the case of one-dimensional periodic structures) says that for any structure formed with the repetition of an identical unit cell, as is the case for the crystals studied here, the change in complex wave amplitude across a unit cell, due to a propagating wave without attenuation, does not depend upon the location of the unit cell within the structure [52]. Therefore, it is possible to study the wave propagation through the entire lattice by considering wave motion just in the unit cell. Bloch's theorem thus leads to enormous savings in the analysis of wave propagation in periodic structures. For the particular case of the shamrock structure, two periodic conditions are applied to the unit cell and are indicated in figure 3.3b with blue and red arrows. The phononic band structure was calculated using finite element methods (FEM) in COMSOL multhyphysics software to solve the 3D elastic wave equation:

$$\rho \frac{\partial^2 u_i}{\partial t^2} = \nabla \cdot (\rho c_t^2 \nabla u_i) + \nabla \cdot \left(\rho c_t^2 \frac{\partial \vec{u}}{\partial x_i} \right) + \frac{\partial}{\partial x_i} [(\rho c_l^2 - 2\rho c_t^2) \nabla \cdot \vec{u}], \tag{3.2}$$

where ρ is the density of the material, $\vec{u}$ is the mechanic displacement and c_t and c_l are the transverse and longitudinal velocities respectively. Figure 3.6(a) shows the

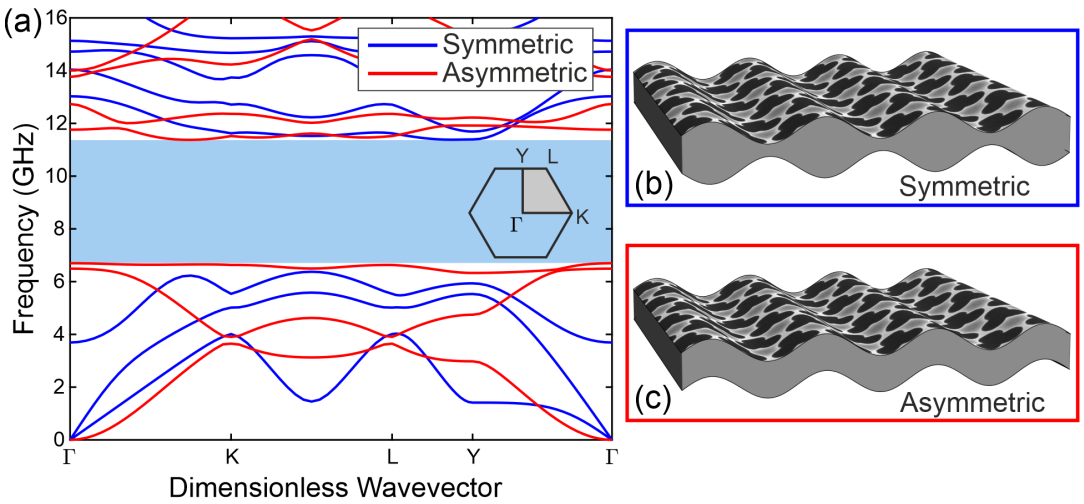

Figure 3.6: (a) Phononic band dispersion for a shamrock crystal slab with t= 220 nm, a=330 nm and r=0.22a along the $\Gamma KLY\Gamma$ path as indicated in the inset. Blue and red curves denotes symmetric and asymmetric modes with respect to the mid plane of the slab as indicated in (b) and (c) respectively. The band calculation was performed considering the anisotropy of the silicon when the [110] direction coincides with the x axis of the crystal.

phononic band dispersion calculated for a shamrock crystal slab with a thickness of $t = 220nm$, period $a = 330$ nm, and radius $r = 0.22a$ along the $\Gamma KLY\Gamma$ path as indicated by the inset. Blue and red modes represent the symmetric (3.6(b)) and asymmetric (3.6(c)) modes with respect to the mid plane of the slab. The light blue region highlights a region from 6.7 GHz up to 11.4 GHz between the 6th and 7th bands where no modes appear. Therefore there is a full gap in this structure with a width of 4.7 GHz and central frequency of 9.05 GHz which corresponds with a gap to mid gap ratio ($\Delta f / f_c$) of 52%. One particularity of this band structure is the almost flat band (dispersionless) in the lower edge of the gap. This contributes substantially to increase the density of phonon states around 6.5 GHz. Usually the band calculations are performed along the high symmetry directions because the extreme points (maximum and minimum) of all bands occurs along these directions. However it was shown that this only holds for certain crystallographic groups [53]. Therefore, one can use the IBZ contour to pre-detect band-gaps, but their extreme values must be confirmed considering the full IBZ.

3.3.3 Gap dependence on geometrical parameters

The particular shape of the shamrock favors the creation of phononic band gaps. As shown in figure 3.3a, the unit cell is composed of a large mass connected by small necks; this particular mass distribution enables the creation of wide full band gaps [33]. To illustrate this better, figure 3.7 shows the gap evolution as a function of the fraction r/a calculated for a membrane with a fixed thickness of 220 nm and four different periods. For all considered periods, if the radius of each circle composing the shamrock is small (below 0.12), there is no gap. For all four curves in figure 3.7 it can be seen that the bigger the radius, the wider the gap, as shown the insets of the unit cell for $r/a = 0.16$ and $r/a = 0.22$. The maximum value of the radius is $r = 0.25a$ which corresponds to the case when shamrocks touch one another but to not

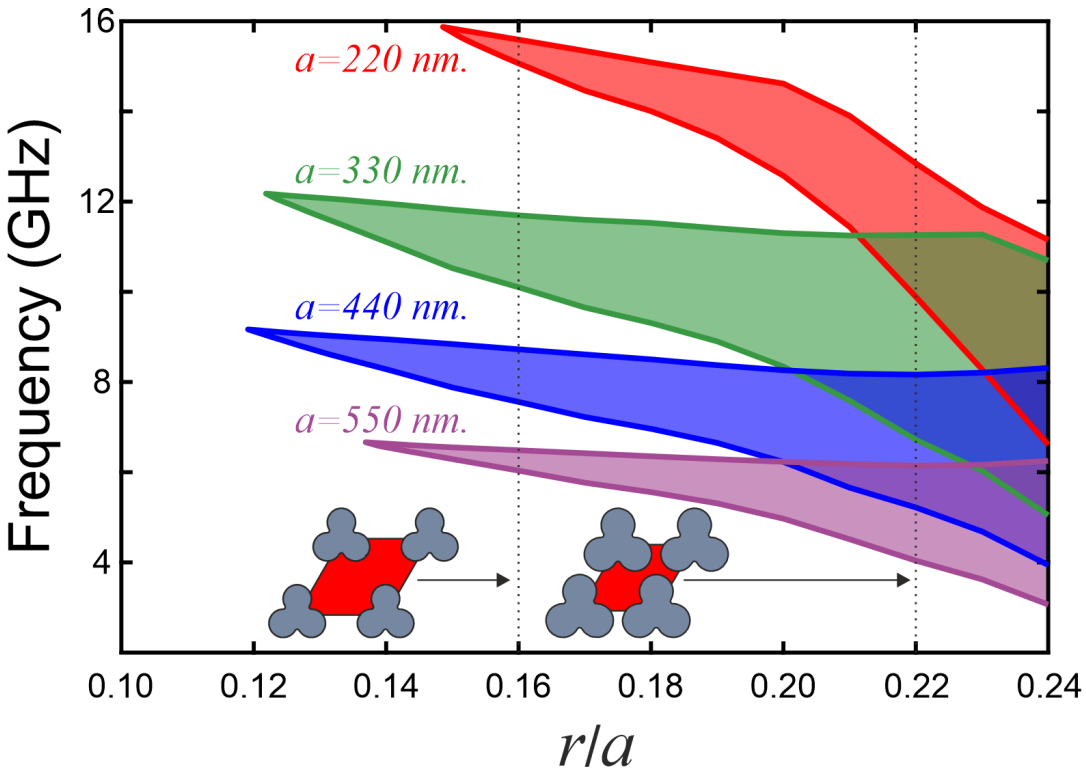

Figure 3.7: Gap dependence on radius r calculated for a fixed thickness membrane of 220 nm and four different periods of 220, 330, 440 and 550 nm. For all simulated periods the width of the gap also increases when the ratio (r/a) increases.

compromise the integrity of the fabricated crystals, we choose a radius of $r = 0.22a$ for all the shamrock crystals studied in this work.

Once we have chosen the optimal ratio r/a considering the fabrication limitations, the evolution of the full gap as a function of the period a can be studied. Figure 3.8 shows the gap width as a function of the period a calculated for a slab with a thickness of 220 nm and varying periods ranging from 100 nm until 600 nm. The gap starts to open around 14 GHz for a period of approximately 150 nm. From that point, as the period increases, the gap width starts to increase reaching a maximum of 6 GHz for a period around 300 nm before it begins to decrease again. The frequency is inversely proportional to the period a. High frequencies require small structures indicating a limitation set by nanofabrication. With this shamrock structure the central frequency of the gap can be tuned by changing the period a and obtain wider gaps up to 6 GHz. This shows the advantages of the shamrock crystal as a phononic insulator and also can be implemented in the fabrication of tunable phononic waveguides. Figure 3.7 also indicates the gap position for three particular periods of 220 nm, 330 nm and 440 nm, which were the periods chosen for fabrication.

3.4 Sample fabrication

The shamrock phononic crystals described in this chapter and the shamrock waveguides described in the next chapter were fabricated at the Technical University of Denmark (DTU) in the group of Prof. Søren Stobbe by Marcus Albrechtsen. They

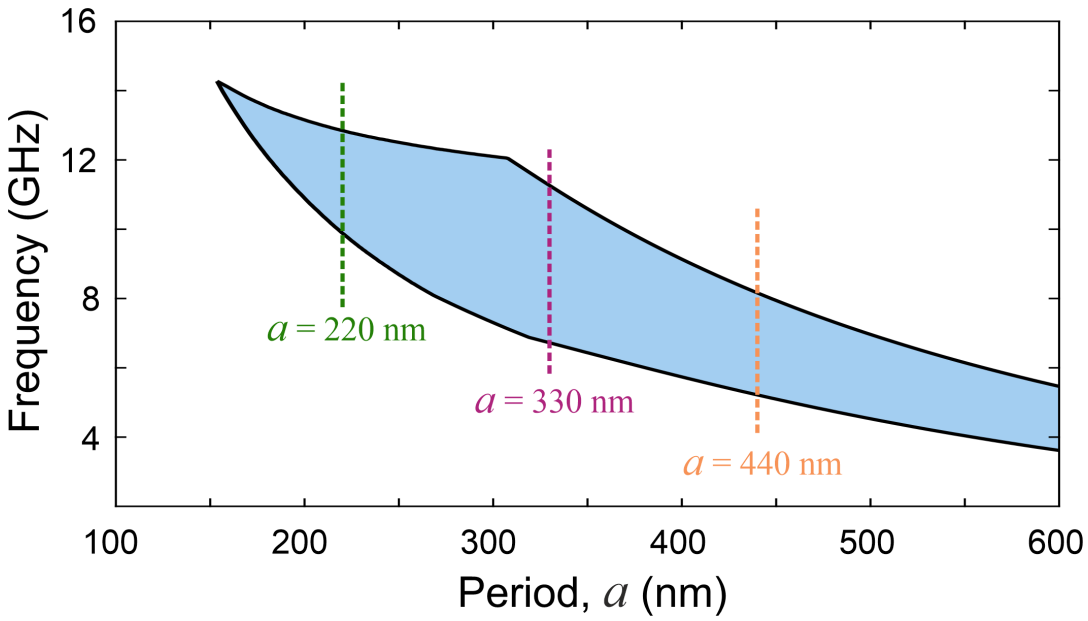

Figure 3.8: Gap dependence on period a calculated for a fixed thickness slab of 220 nm and fixed radius $r = 0.22a$ nm. The dashed lines highlights the gap position for the three fabricated crystals of $a = 220$, 330 and 440 nm.

were fabricated on chips cleaved from a commercial (SOITEC) 12-inch SOI wafer, which has a nominal 220 nm thick device layer and a 2 μm thick buried oxide layer. The lithography, dry-etching, and release etch of the suspended membrane was done as detailed in [54] with some minor changes. There they were able to fabricate a cavity which confine photons inside 8 nm width silicon bridges. As we do not need to make as small features for our shamrock phononic crystals, it was spin-coated onto the substrate a thicker (180 nm) softmask (Chemically Semi-Amplified Resist, CSAR6200.09), which enables to reduce the periodic sidewall roughness (scallops). The patterns were defined with a 100 keV 100 MHz JEOL-9500FSZ electron-beam writer with a 200 pA current and a dose density of 2.5 aC/nm^2 in the center, boosted by 10 % in the corners to compensate long-range proximity effects across the large crystals [55]. The foot print of the fabricated crystals was 50 by 50 μm. A proximity effect correction was implemented using the standard Gaussian approximation that takes the form:

$$\Psi(r) = \frac{1}{\pi\,(1+\eta)}\left[\frac{1}{\alpha^2}e^{-(r/a)^2} + \frac{\eta}{\beta^2}e^{-(r/a)^2}\right]. \tag{3.3}$$

Here the first Gaussian describes the size of the focused electron beam. The spot size has a full-width half-maximum that is approximately 3.3 nm in our case, since a 40 μm aperture and 200 pA was used. This is much smaller than the pitch of the crystals, and therefore the long-range scattering (> 1 μm distances) is effectively described by

$$\Psi(r) = \frac{1}{\pi\,(1+\eta)}\left[\pi + \frac{\eta}{\beta^2}e^{-(r/a)^2}\right], \tag{3.4}$$

and the intermediate- and short-range effects are neglected. The parameter β describes the range of the long-range scattering and η describes the fraction of total dose received from this effect. For 100 keV with a silicon substrate $\beta = (30 \pm 2)$ μm and $\eta = (0.7 \pm 0.4)$ depending on other parameters such as resist thickness. For the fabrication process described here the values were $\beta = 30$ μm and $\eta = 0.5$. In this

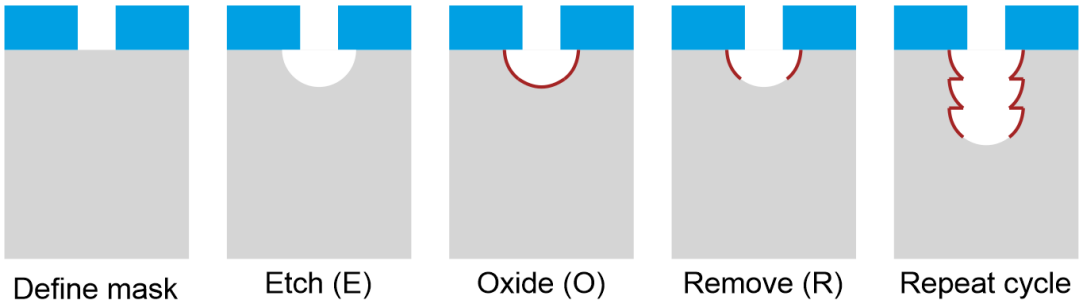

Figure 3.9: Schematic of the CORE, Clear (C), Oxide (O), Remove (R), Etch (E) cyclic etch process.

process the cyclic dry-etching process CORE [56] was also further modified, with 3 changes from the process described in Ref. [54]. CORE is a switched process based on 4 steps [54, 56], done cyclically in the following order:

1. The clear step (C), which purges the reactor to obtain a reproducible plasma in the following steps. The plasma is turned off during this step.
2. The oxidation step (O), which grows a thin layer of silicon oxide everywhere on the silicon surface using an ($\approx$ 50 mTorr) oxygen plasma with low DC bias; this step also etches the resist uniformly.
3. The bottom removal step (R), which uses a low density ($\leq$ 0.2 mTorr) SF_6 plasma, i.e., a large DC bias will sputter the SiO_x from the bottom of the patterned features. This step will also erode the resist.
4. The main etch step (E), which uses a dense ($\approx$ 50 mTorr) SF_6 plasma. This step etches silicon isotropically, forming so-called scallops, whose size is controlled by the time of this step. Since it is high pressure it has a low DC bias, which means that it does not erode the mask.

Figure 3.9 outlines the three main steps (starting with the first E-step in the process). The sequence is repeated until the pattern is fully etched (220 nm). Therefore, the size of the scallops, and implicitly the periodic sidewall roughness, is controlled by the duration of the E-step, with more cycles and shorter steps yielding less roughness. However, the number of possible cycles is limited by the thickness of the resist, which is eroded during the O and R steps. In Ref. [54], a thin resist (65 nm) is used to obtain high aspect-ratio features, though 10 cycles with 73 seconds etch-time is used to fully etch the sample. Here, we use a thicker resist (180 nm), which enables the etch in 14 cycles of 45 seconds.

As it was mentioned previously, we chose three different periods to fabricate and measured changes in the band gap frequencies. Figure 3.10 shows a Scaning Electron Microscopy (SEM) top view image of the fabricated samples with periods of 220, 330 and 440 nm with the same parameterized radius $r = 0.22a$. All the crystals have a full area of 50x50 μm.

3.4.1 Contour fitting and statistical analysis

The SEM images of the fabricated samples can be used to evaluate their quality. The average shape of the fabricated shamrock holes can be obtained from a statistical study of shapes extracted from the same SEM image. Each contour comes from a

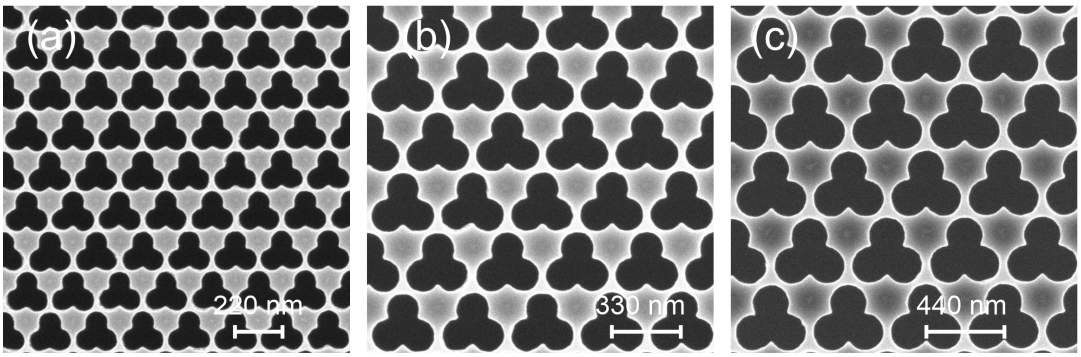

Figure 3.10: SEM images of the fabricated shamrock crystals with periods of (a) 220 nm, (b) 330 nm, and (c) 440 nm.

binarized version of the original SEM image adjusted to obtain the most accurate result. Because holes in SEM images appear in black, a limiting pixel value can be set and a new image can be createdin which all the pixels below these values will be black (holes) while the others above the same value will be white (structure). The accuracy can be adjusted changing the limiting pixel value and the fidelity of this approximation can be evaluated by superimposing the fitted contours and the original image as shows figure 3.11(a) for the crystal with a period of 330 nm. In this case were fitted 56 shamrock holes and figure 3.11(b) plots the ensemble of all contours (red dots) and their mean values (blue dots). The shapes of the individual fitted shamrocks are very similar which is a qualitative measure of the fabrication tolerance.

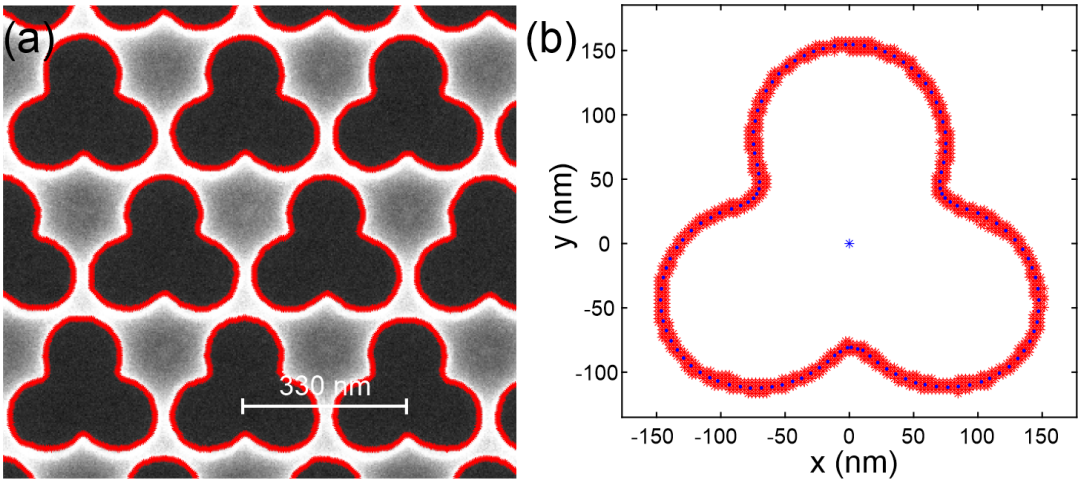

Figure 3.11: (a) Fitted contours in a shamrock crystal with a period of 330 nm. (b) Superposition of all the contours (red) and their mean values (blue points).

To quantify the degree of imperfection, we compare the mean value and standard deviation of the ensemble averaged area of the shamrocks with the nominal value. The fitted areas are obtained performing a numerical integral (in Matlab) of the coordinates showed in 3.11(b), and the nominal one, from the coordinates of the projected shamrock shown in figure 3.2. Figure 3.12 plots the histogram distribution of the fitted areas in nm^2 of each individual shamrock (in red), and the mean value (in blue). The gray line in figure 3.11 indicates the nominal area of the designed geometry. The difference between the average area, $5.12 \times 10^4 nm^2$, and the nominal

area, $4.91 \times 10^4 \text{nm}^2$, is attributed to the not fully resolved corners of the shamrock, as displayed in the inset of the figure. This clearly shows the significance of avoiding sharp corners in the unit cell geometry, which requires an accurate fabrication process. Although geometric inspection using SEM images has its limitations, this simple analysis shows the high quality of the fabrication process used here and also the simplicity and robustness of the pattern selected to create the periodicity.

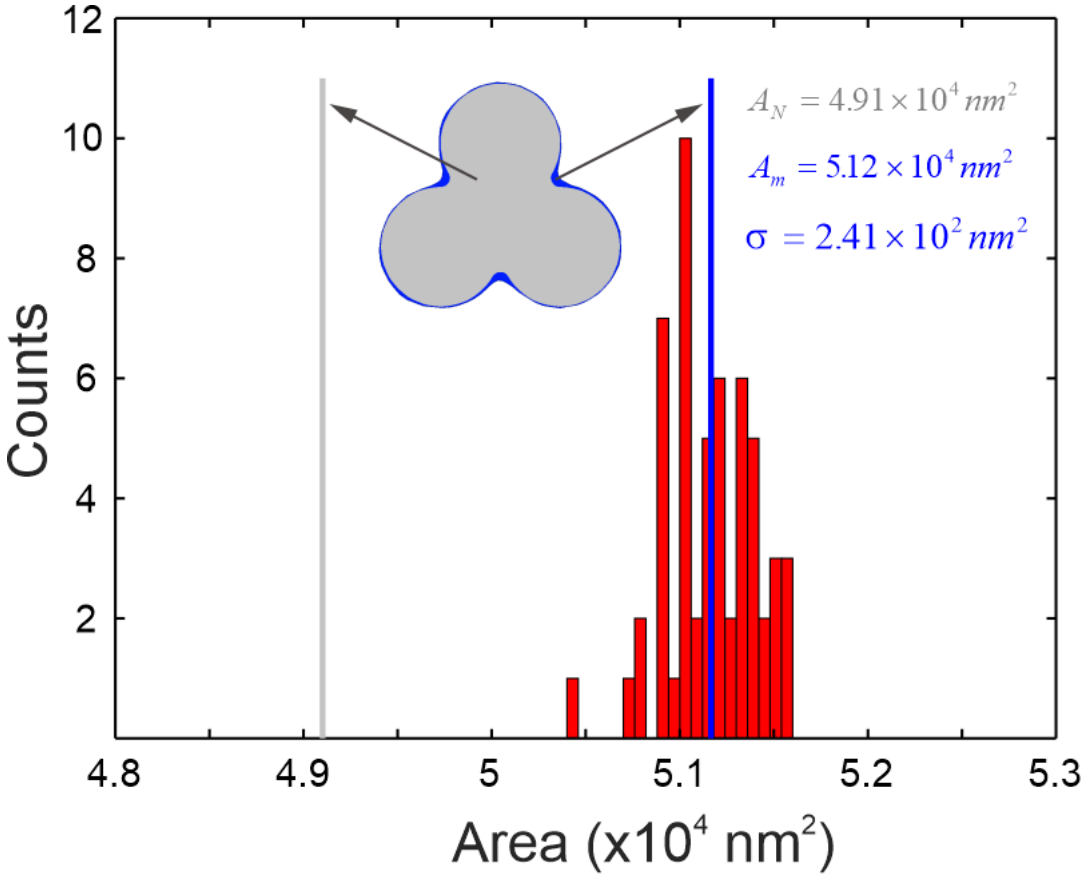

Figure 3.12: Histogram for the 56 fitted areas (red) and its mean (blue), compared with the nominal value of the designed area (gray). There is a small difference between the mean and nominal areas caused by the etching in the intersection of the circles as shown the inset.

Once the shamrock contours have been fitted, this information can be used to study the period fluctuation in the fabricated structure. This is done by finding the centroid of each fitted shamrock, the blue central point in figure 3.11(b), and calculating the distance between neighbours as indicated in figure 3.13(a). From these 56 contours we can extract 42 horizontal periods, like indicates the horizontal green arrow in the figure, and 40 vertical periods like indicates the diagonal green arrow. This results in 82 distances to make a statistical analysis as the one presented in figure 3.13(b). The obtained mean value for the period is 330.26 nm with a standard deviation of 1.28 nm. This further confirms the accuracy of the fabricated sample with a nominal period of 330 nm.

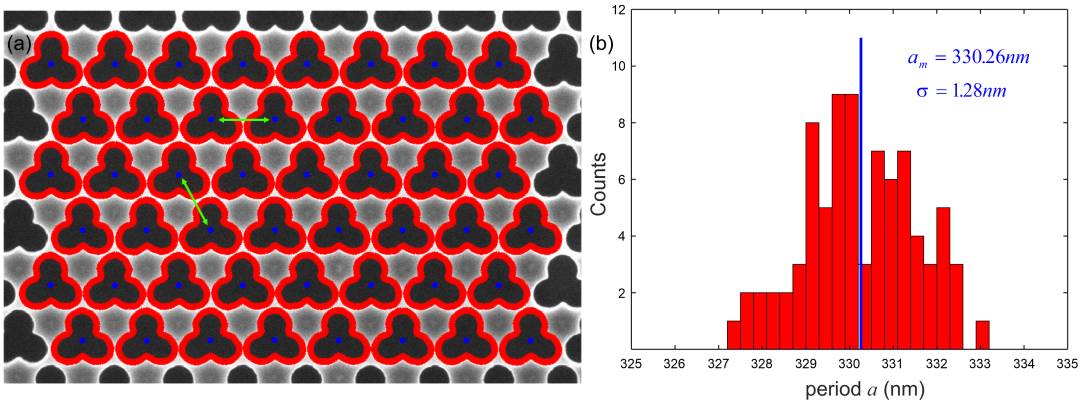

Figure 3.13: (a) centroids (blue points) for all the fitted shamrocks. The green arrows indicate the distances (periods) taken for the statistics. (b) histogram for the 82 obtained periods. The main value of the fitted periods is 330.26 nm with a standard deviation of 1.28 nm which is accurate compared with the projected period of 330 nm.

3.5 3D phononic dispersion relation and density of states

Taking advantage of the statistical study discussed in the previous section, the mean fitted shamrock (blue points in figure 3.11(b() can be used to build a more accurate crystal unit cell for implementation in COMSOL software to obtain the phononic band structure of the fabricated sample. Figure 3.14 shows the 3D dispersion relation obtained using the fitted unit cell for the crystal with period of 330 nm. The band structure is calculated for the entire first Brillouin zone. This is done by discretizing the reciprocal wavevectors k_x and k_y, for the IBZ highlighted in pink in the bottom part of figure 3.14 and then replicating the obtained bands for the rest of the first BZ. As before, blue and red curves denotes symmetric and asymmetric modes respectively. From this figure the gap extends along the entire first BZ, it means, is a full gap. From this full dispersion relation the phononic Density Of States (DOS) for the crystal can also be calculated, using the following expression:

$$DOS = \frac{N}{\Delta f \cdot V \cdot N_k}, \tag{3.5}$$

where N are the number of modes counted over the frequency range Δf (histogram of frequencies). V is the volume of the unit cell, obtained directly from COMSOL, and N_k is the number of points of the calculation mesh within the IBZ, this is, the discretization of k_x and k_y over IBZ. For this particular case Δf= 100 MHz, $V = 8.9760 \times 10^{-21}$ m^3 and N_k=176 points. Figure 3.14b shows the calculated DOS. The light blue region highlights the full mechanical band-gap from 6.7 GHz up to 11.4 GHz. In the bottom part of the gap, the DOS is particularly high compared with lower frequencies because of the red flat (dispersionless) band on the edge of the gap as shown figure 3.14(a). The same phenomenon occurs with the bands around 15 GHz that also increases the DOS.

To experimentally characterise this full gap, it was measured the scattering spectra along the simplified path $\Gamma KM\Gamma$ indicated in figure 3.14(a). This is sufficient to characterise the full width of the phononic gap as its limiting frequencies do not change with respect to the IBZ. Figure 3.15(a) shows the edges of the gap calculated along the IBZ, for the ΓP path, as a function of the rotation angle φ, as indicated

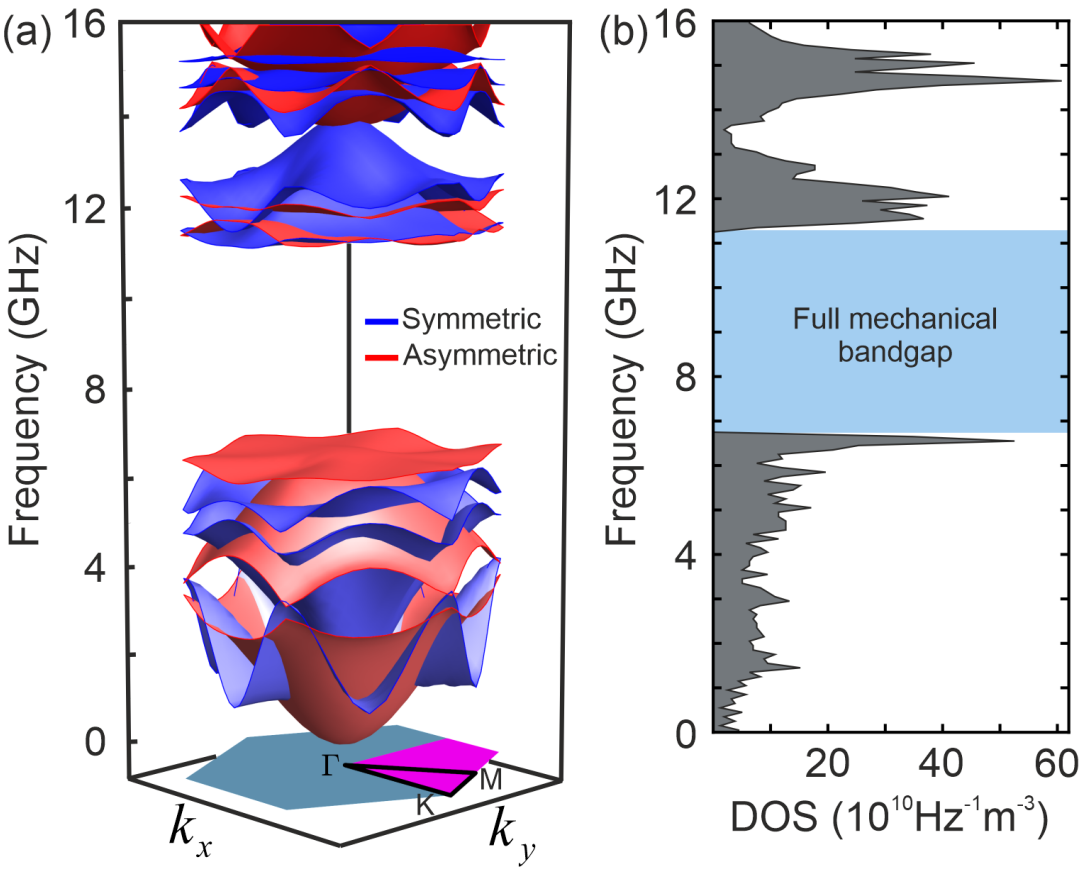

Figure 3.14: (a) Simulated 3D phononic dispersion relation over the first Brillouin zone, using the extracted geometrical parameters from SEM images for the crystal with a=330 nm. Blue and red curves indicates symmetric and asymmetric modes respectively. (b) Calculated phonon density of states (DOS) for the same structure. The light blue region highlights the full phononic band gap spanning from 6.7 GHz to 11.4 GHz.

in the inset. P is the point determined by φ at the edge of the IBZ. The lower edge of the gap is constant for all angles because the limiting value is in Γ for the entire IBZ as shown figure 3.15(b), where we plot the ΓP band dispersion for $\varphi = 15°$, $45°$, and $75°$. $\varphi = 0$ corresponds with the ΓK path and $\varphi = 90$ corresponds with the ΓY path.

3.6 Experimental reconstruction of the mechanical dispersion relation

Using Brillouin light scattering and the experimental setup described in chapter 2, it is possible to obtain the phononic band dispersion of the fabricated shamrock crystals. When incident light with wavevector $\vec{k}_i$ reaches the sample with a certain angle θ as show figure 3.16, a small part of the light is non-linearly scattered by the photoelastic (PE) or moving-boundary (MB) mechanisms, both discussed in chapter 2. For the measurement of shamrock crystals, considering that the structures are suspended and the thickness is only 220 nm, the scattering volume is small given the direction of the incident light. In addition, considering the large refractive index contrast between

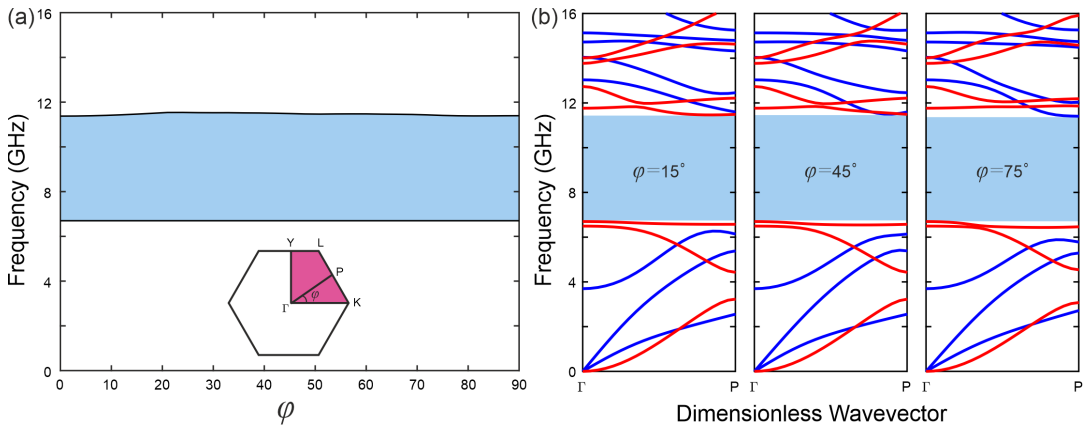

Figure 3.15: (a) Band gap edges for the a=330 nm. crystal. The lower edge is always constant as the limiting value is at the Γ point. (b) Calculated bands along the ΓP path that is indicated in the inset of (a), for φ=15°, 45°, and 75°.

the surrounding air (n=1) and the silicon crystal (n=4 for λ=532), the scattering process in this structure will be dominated by the MB mechanism. Therefore it can be proved the parallel mechanic wavevector $\vec{q}_{\parallel}$ in figure 3.16, by changing the angle θ and reconstruct the phononic band dispersion.

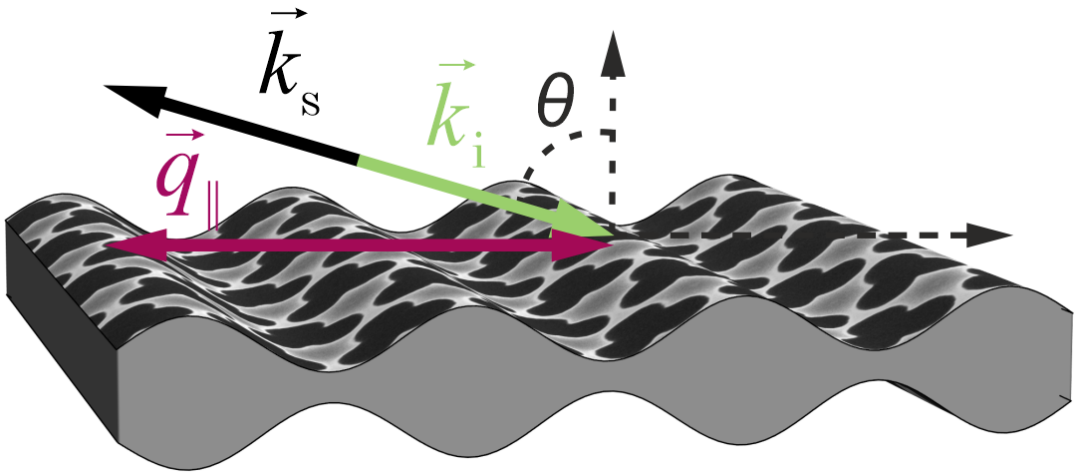

Figure 3.16: Schematic ilustration of Brillouin scattering with the phase-matching condition for the backward configuration used to measure the crystal. Here $\vec{k}_i$ and $\vec{k}_s$ represents the incident and the scattered light respectively, and $\vec{q}_{\parallel}$ is the parallel mechanic wavevector.

With the Tandem Fabry-Perot Interferometer described in the previous chapter, we measure the shamrock crystal. Figure 3.17 shows the obtained spectrum for the crystal with a=330 nm taken with an incident angle of 32.5° which corresponds with the high symmetry point K in the reciprocal space. The spectrum is symmetric because Stokes and Anti-Stokes contributions are equally likely in a stochastic process such as spontaneous Brillouin scattering [32, 57]. The central peak corresponds with Rayleigh scattering and the other peaks, enumerated from 1 to 7, correspond with the vibrational frequencies of the phononic modes of the crystal. The amplitude depend on the scattering efficiency of each mode with the incident laser light [58],

which is proportional to the displacement of the boundaries. The phonon frequencies can be obtained by fitting each of the observed peaks to lorentzian line shapes and extracting the mean value between the resonant frequencies of the Stokes and Anti-Stokes components.

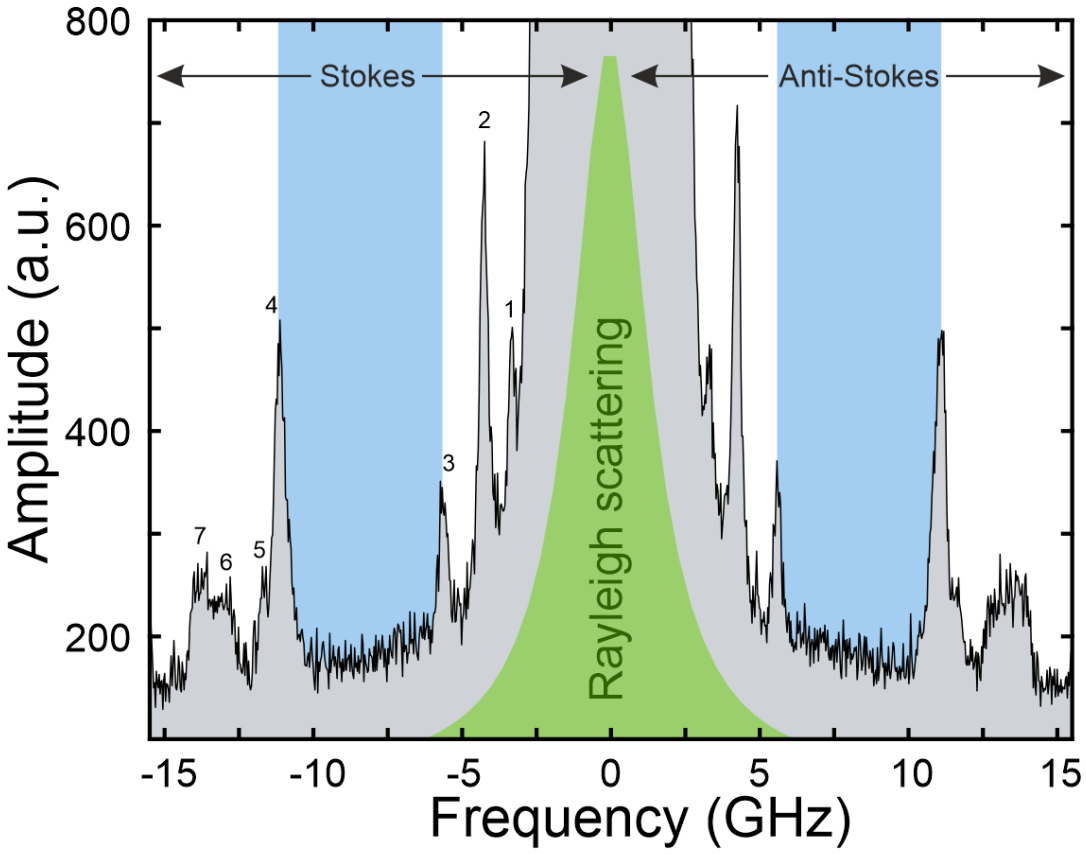

Figure 3.17: Measured Brillouin scattering spectrum for an incident angle of θ=32.5° with p-polarized light. The green central peak stems for elastic Rayleigh scattering. Negative and positive frequency peaks correspond to Stokes and anti-Stokes contributions respectively. The light blue region highlight the mechanical gap.

The light blue regions in figure 3.17, going from 5.6 GHz until 11.1 GHz shows that no peaks appear in this frequency window. This is the evidence of the mechanical gap. One spectrum alone can not confirm a gap as it is possible that there are modes that do not scatter enough light to be detected. To confirm that we are dealing with a full mechanical gap, we take the same measurement for different angles using the same incident power (2.5 mW), the same focusing lens with 3 cm of focal length, and the same acquisition time of 24 hours for each spectrum.

Figure 3.18 shows the calculated band structure (continuous lines) and experimental measurements (black dots) from Γ (0°) until K (32.5°). We measure from 6° until 30° with a step of 3° and the additional angle for K. Measurements at smaller angles or in the Γ point (at zero degrees) are rather challenging to obtain in the backscattering configuration because the specular elastic reflected signal is so strong that it completely masks the relatively much weaker Brillouin scattered signal. The minimum angle for acquisition depends on the lens used to focus and collect the scattered light. This is given when it is possible to block or separate the backscattered

signal and the strong specular reflected signal. The specular signal must not enter back into the collection system.

As before, blue and red curves indicate symmetric and asymmetric modes. The green region on the bottom of the spectra indicates the frequency window that is masked by the strong Rayleigh peak also indicated in green in figure 3.17. The experimental measurements in figure 3.18 confirm the existence of the gap at least for the ΓK direction; although there is poor correlation between experiment and simulations. This mismatch between theory and experiment is obtained despite the fact that it was explored the fabricated geometry through the SEM statistical analysis to obtain the more accurate geometrical parameters for simulations as was discussed in subsection 3.4.

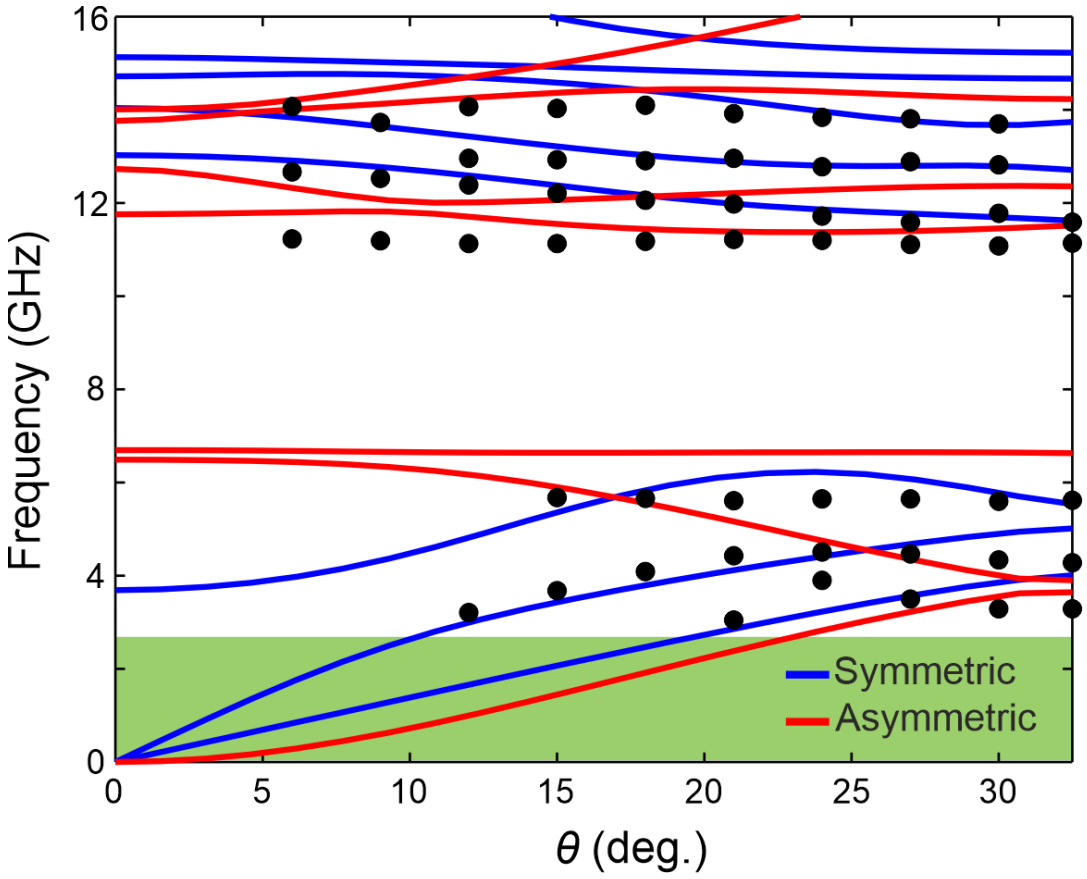

Figure 3.18: Calculated band structure (solid lines) for the a=330 nm crystal from Γ (0°) until K (32.5°). Black dots represents fitted frequencies measured each 3°. As before, blue and red lines represents symmetric and asymmetric modes. The green region indicates the frequency window that is masked by the central Rayleigh peak. The agreement between simulations and experiment is not good.

There is additional information from he fabricated crystals that can not be extracted from the original SEM images and it is the vertical profile of the eroded hollows in the structure. In the previous simulations it was assumed perfectly straight sidewalls to build the unit cell as shown figure 3.3(b). Due to imperfections in the fabrication process, during Reactive Ion Etching (RIE), or the CORE process presented schematically in figure 3.9, the wall can be eroded with a certain angle. Figure 3.19 shows a Focus Ion Beam (FIB) cut from a fabricated shamrock crystal. The SEM images

show imperfections in the bottom and vertical walls of the suspended crystal. This is not the same structure for which measurements are presented in figure 3.18, but is a good illustration to note how fabrication processes can modify the unit cell of the projected crystal.

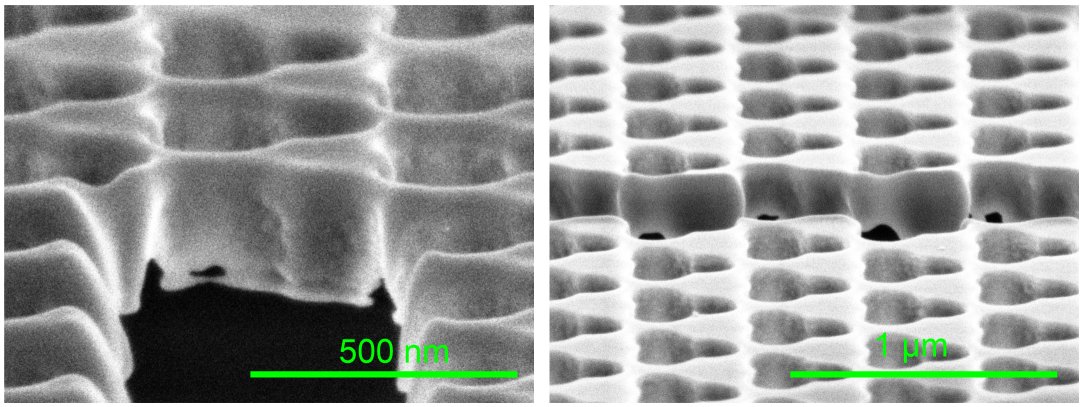

Figure 3.19: Focus ion beam cuts in a suspended shamrock crystal fabricated in silicon. The SEM images shows how the fabrication process can modify the unit cell of the designed crystal.

This suggest that modifications in the vertical profile of the unit cell need to be introduced to accurately calculate the band structure. Figure 3.20 shows the simulated bands for the same crystal as figure 3.18, this time considering a 4° tilt in the sidewalls of the unit cell as highlighted by the red lines in the inset. It is worth clarifying that the measured crystal itself was not cut with a FIB, and that the angle was adjusted only in the COMSOL model to obtain the best correlation between simulations and experiment. Figure 3.20 shows a good agreement between theory and experiment with a close fit between the edges of the gap. The figure also shows that it is possible to track some bands when changes the angle. In this figure all the bands are purple as vertical symmetry in the membrane is lost due to this sidewall tilt. Some bands are invisible to the measurement technique and as the mode profile does not produce enough surface displacement to scatter the minimal amount of light necessary to be detected by the TFP interferometer.

These results shows the importance in considering all the geometrical parameters of the fabricated sample. Fluctuations in the sidewall profile strongly modify the band structure of the crystal, even more than imperfections in the crystal pattern. The lower edge of the gap moved from 6.7 GHz to 5.8 GHz at the Γ point, a shift of almost 1 GHz of frequency when considering a tilt of 4°. This corresponds with a lateral difference of 15 nm approximately at the top and bottom face of the membrane.

With the TFP interferometer it is possible to probe different crystallographic directions of the reciprocal space and reconstruct the band diagram. Figure 3.21 plots the dispersion relation calculated along the $\Gamma KM\Gamma$ path, indicated in the bottom part of figure 3.14. The intensity color scale represents the normalized coupling coefficients for the MB perturbation. Black dots are the experimental measurements and the vertical dotted line indicates the frequencies obtained from the measured spectrum showed in figure 3.17. The inset indicates the thickness of the silicon plate and the deviation of 4° considered in simulations and the green area denotes the masked region by the Rayleigh peak. This graph also shows that the gap is present in other

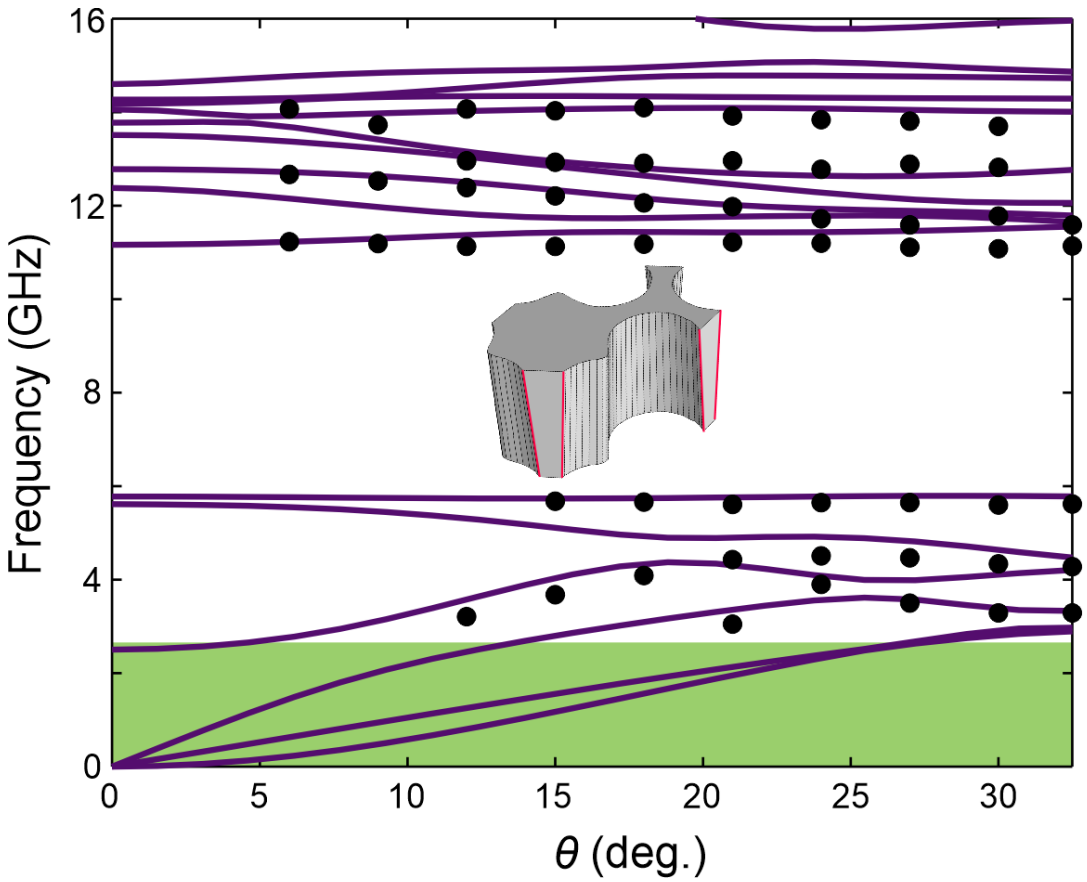

Figure 3.20: Calculated band structure (solid lines) for the a=330 nm crystal from Γ (0°) until K (32.5°) considering tilted sidewalls with 4° of deviation angle. Black dots represents the fitted frequencies. With this small correction, simulation and measurements show closer agreement.

paths of the reciprocal space and is the experimental confirmation of a full phononic bandgap.

To measure different paths in the reciprocal space, different rotations of the sample are required. For the ΓK path the angle θ should be changed as indicated in figure 3.21(b) where the green arrow represents the incident laser. In this case the ΓK path is aligned with the x axis as indicate the yellow line in the inset. Here, the value of the maximum angle θ is calculated from the relation $q_{\parallel} = |\Gamma K| = \frac{4\pi}{3a} = \frac{4\pi}{\lambda_i} \sin\theta$.

To map the ΓM direction, we rotate the sample 30° to align the ΓM path with the horizontal direction as indicated in the inset of figure 3.21(d) and, from that position, we rotate the angle θ. Here, the maximum angle is indicated by $q_{\parallel} = |\Gamma M| = \frac{2\pi}{\sqrt{3}a} = \frac{4\pi}{\lambda_i} \sin\theta$. Mapping the KM path requires the simultaneous variation of two specific angles α and θ to measure the intersecting point of the blue segment and the horizontal direction, as depicted in figure 3.21(c).

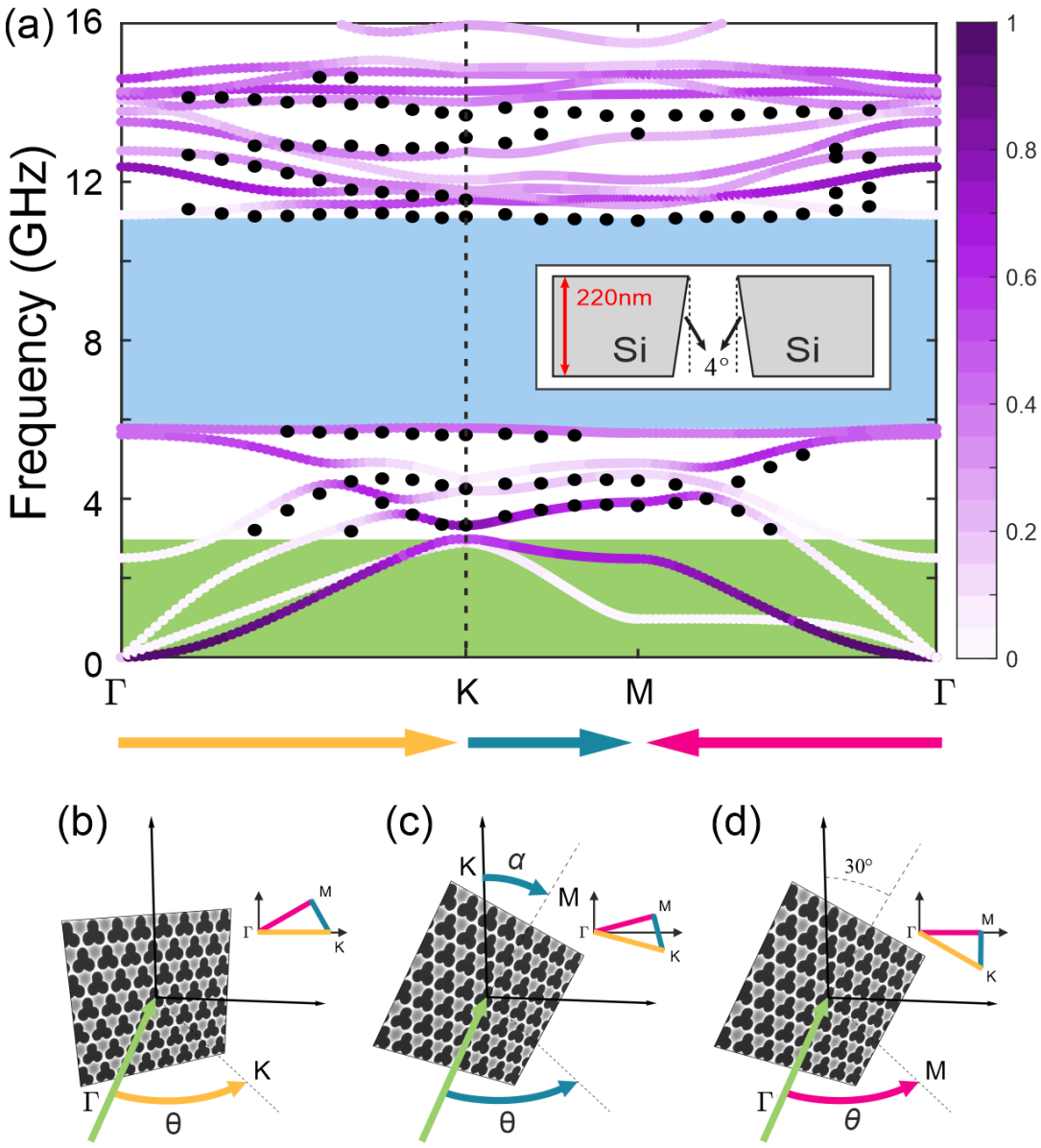

Figure 3.21: Calculated dispersion relation based on the geometrical parameters obtained from SEM images of the fabricated samples that include a 4° sidewall angle correction in the vertical profile (inset). The black dots represent the measured frequencies of vibrational modes for different angles and the vertical dotted line indicates the frequencies obtained from the measured spectrum shown in figure 3.17. The intensity color scale represents the normalized coupling coefficients for the moving-boundary perturbation. (b)-(d), The direction in which the sample is physically rotated to scan along the highest-symmetry directions ΓK (b), KM (c) and ΓM (d). The green arrows indicate the direction of the incident laser light while the other colored arrows correspond to the rotation direction during measurements, which represent (and are color-consistent with) the highest-symmetry direction indicated in (a).

3.7 Tunability of the mechanical gap with geometrical parameters

The mechanical gap of the shamrock crystal can be tuned by changing the period of the structure as shows figure 3.8. Phononic crystals with periods of 220 and 440 nm also were fabricated (see figure 3.10), and characterized using BLS spectroscopy. Figure 3.22 shows the experimental band reconstruction for crystals of 220 nm (a), and 440 nm (b). Solid lines are simulated bands and black dots are the measured frequencies for different angles. Here we also applied a 4° correction to the vertical profile. For both crystals the full gap could be measured, experimentally validating gap tunability.

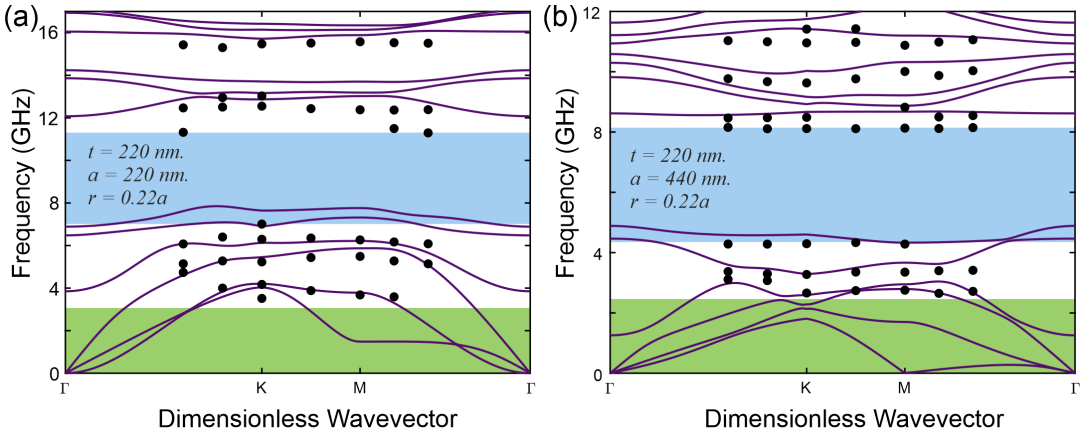

Figure 3.22: Experimental band reconstruction for shamrock crystals with periods of (a) 220 nm and (b) 440 nm.

The correlation between experiment and theory for the crystal with a=220 nm in figure 3.22(a) is less accurate as for such a small crystal, the geometry fluctuations are bigger and the projected/simulated geometry differ more with the experiment. Even with this limitation, the experiment shows a similar trend for the bands, for example, on the upper side of the gap, but with a shift in frequency.

3.8 Optical dispersion relation for shamrock crystal

The shamrock crystal also presents a complete gap for TE optical modes in the THz regime. It makes this structure an optomechanic or a phoxonic crystal. Figure 3.23(a) shows the optical band structure for the crystal with a = 330 nm calculated along the optical IBZ. Here, because it is assumed the same refractive index for all the material, the IBZ is determined by the $\Gamma KM\Gamma$ path. The grey zone indicates the light cone, the location of the guided modes, and the continuum where the modes are extended in the air. Between the first and the second band appear a complete gap below the light cone from 350 THz up to 350 THz approximately. This corresponds to wavelengths between 1000 nm and 860 nm respectively.

Figure 3.23(b) shows the TE gap evolution as a function of the period a, considering a thickness of t = 220 nm and a radius of $r = 0.22a$. The y axis is given in terms of the wavelength instead of frequency to help in the design for a desired λ. For example, with a period of 600 nm, a shamrock optomechanic crystal has an optical

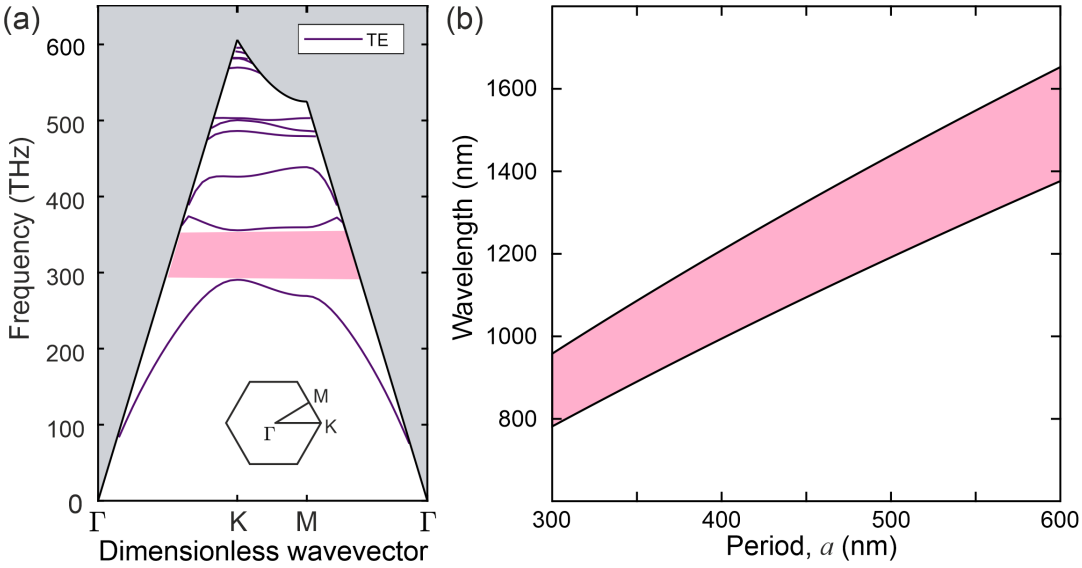

Figure 3.23: (a) Optical dispersion relation for TE modes in a shamrock crystal with $a = 330$ nm. The grey area indicates the light cone and the pink area highlights the complete band gap. (b) TE gap evolution as a function of the period for the shamrock crystal.

gap centered at $\lambda = 1550$ nm (telecom wavelength), and a phononic gap of 2 GHz centered at 4.5 GHz approximately, as indicates figure 3.8. This implies that such a structure could have interesting applications in optomechanics because allows the guiding and co-localization of optic and mechanics waves in the same structure and in a small volume. Furthermore, the overlap and coupling between photonic and phononic fields is enhanced. The next chapter will explain how to find the best configuration to build these waveguides.

3.9 Conclusions

This chapter provides a detailed description of the Shamrock system and their advantages, all this supported by experimental evidence. The main conclusions are summarized below

- The particular shape of the shamrock feature allows the appearance of wide frequency gaps. A bigger shamrock radius leads to smaller necks width in the unit cell that as a consequence produces a wider frequency gap in the phononic dispersion relation.
- The frequency gap of this system can be tuned by changing the period of the structure. It was experimentally measured in three different fabricated crystals obtaining a gap tunability from 4 GHz up to 12 GHz approximately.
- The statistical analysis from SEM images shows the quality of the fabricated samples. Fluctuations in shape and position of crystals are small and almost negligible. This fact is reflected at the time to match theory vs. experiment.
- It was shown that geometrical robustness is crucial for the proper band engineering. minimal deviations in the vertical profile of the drilled shamrock holes causes large frequency shifts.

Chapter 4

Phononic waveguides

4.1 Introduction

One direct application of crystals with bandgaps is the construction of defect waveguides and cavities. The same idea is applied for light (photons) and mechanical waves (phonons). In this chapter, I present direct experimental detection of hypersonic guided modes measured in the shamrock phononic waveguides using Brillouin light scattering spectroscopy to detect these modes at room temperature and with no external excitation. The tunability of the mechanical gap in shamrock crystals also allows the tunability of guided modes. Furthermore we can control the numbers of modes propagating in the waveguide by changing the waveguide width. These results shows that we are designing structures that can vibrate just by the excitation of thermal phonons and furthermore enables the propagation of waves with low energy consumption.

4.2 Defect-line waveguides

In 1966, Charles Kuen Kao carefully calculated how to transmit light over long distances via optical glass fibers [59]. He realized that by carefully purifying the glass, thin fibers could be manufactured that would be capable of carrying huge amounts of information over long distances with minimal signal attenuation and that such fibers could replace copper wires for telecommunication [60]. Thanks to the invention of laser, light can be guided through the optical fibers based on the principle of total internal reflection as shown in figure 4.1a. A small change of the refractive index between the core and the cladding ($n_{co} > n_{cl}$) enables the light to propagate through the higher index medium over long distances with low attenuation (0.2 dB/km for λ=1550 nm). This fact was a huge step for telecommunications because lowering costs in signal amplification, in addition to leading to a Nobel prize for Charles Kao. If it is required to guide mechanical waves instead of light, it is not possible to apply the same principle because acoustic impedance of solid materials are high and close in value and it is not possible to realize index guiding with large impedance contrast for elastic phonons; elastic waves will leak to the walls of the waveguide. If the walls can not absorb the mechanical waves because the surrounding medium of the waveguide have a bandgap for certain range of frequencies, The wave have to stay in the core of the waveguide. This is the principle of defect waveguides [61–63] made with phononic and photonic crystals as illustrates figure 4.1b. Defect waveguides are based in the confinement of waves in a medium surrounded by crystals that posses a full bandgap. The same principle it is applied to build the shamrock waveguides.

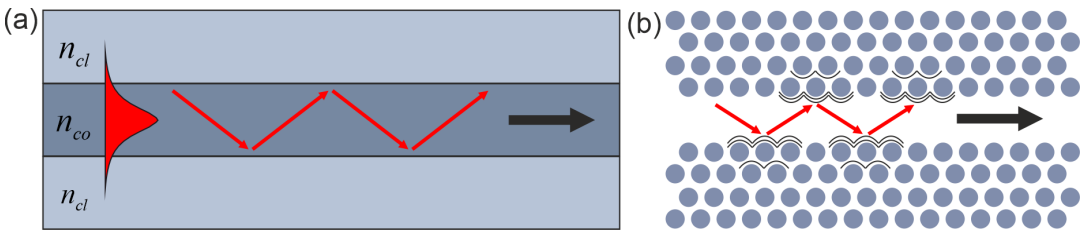

Figure 4.1: (a) Total internal reflection used to guide light in optical fibers. n_co have to be higher than n_{cl}. (b) Waveguiding by mean of a defect line inside two photoni/phononic crystal with a band gap. Waves can not propagate through the crystal and therefore is guided within the defect.

4.3 Shamrock waveguides

Given the geometry of the shamrock feature, it is possible to create three diferent configurations of defect waveguides and it is when the surrounding shield crystals are pointing in the same direction, back to back, and front to front as figure 4.2 (a), (b) and (c) indicates respectively. The black dotted line indicates the waveguide in each case. The different waveguide configurations are possible because the c_3 rotational symmetry of the shamrock and it is not possible for example with a crystal composed of circles or squares. It is possible to have three more configurations of waveguides if it is displaced the upper crystal half period in the horizontal direction with respect to the lower one, refereed as glide-plane waveguides (GPW) [64, 65], employed to study the chirality of guided modes, with possible applications in non-reciprocal devices. These waveguide configurations are not considered in this work. The defect waveguides are only periodic in x direction as shown in figure 4.2; therefore there is no Brillouin zone in this case and the wavevectors in the reciprocal space are limited to between 0 and π/a.

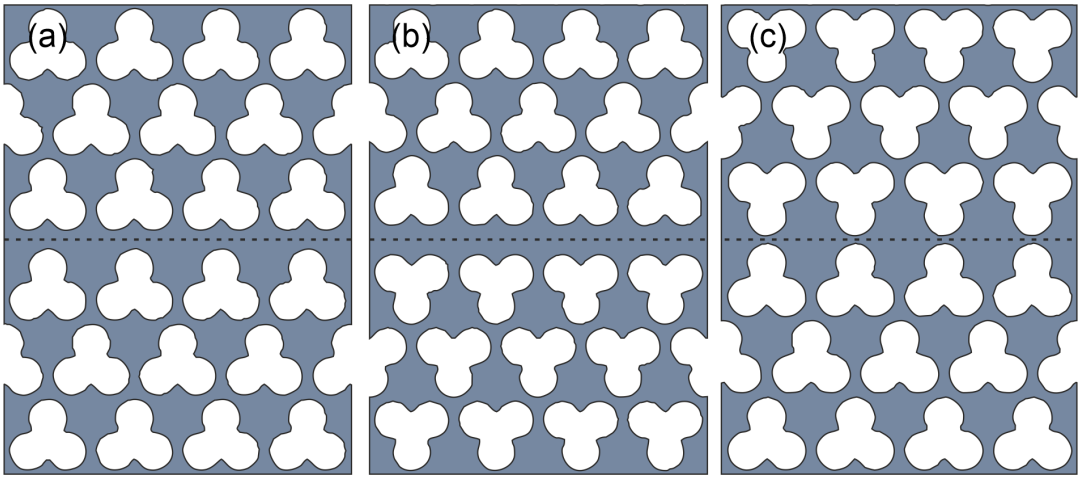

Figure 4.2: (a) Total internal reflection used to guide light in optical fibers. n_co needs to be higher than n_{cl}. (b) Waveguiding by means of a defect line inside two photonic/phononic crystal with a band gap. Waves can not propagate through the crystal and therefore have to propagate in the defect.

4.3.1 Unit cell for shamrock waveguides

The Floquet periodic conditions discussed in the previous chapter also can be applied here to simplify the simulation of the whole structure to determine the guided modes for each configuration. Figure 4.3 shows the construction of the unit cell for the waveguide starting from the shamrock crystal. The yellow features indicate the shamrocks that will be removed to form the waveguide. d is the distance between the shamrocks closest to the interface. For the case of figure 4.3 $d = 2a\sin(60)$. For later designs, we will use the parameter nwg to vary the width of the waveguide as a function of d, where the new width is defined as $D = nwg * d$. For waveguide fabrication we chose three different values: nwg= 0.6, 0.8 and 1.

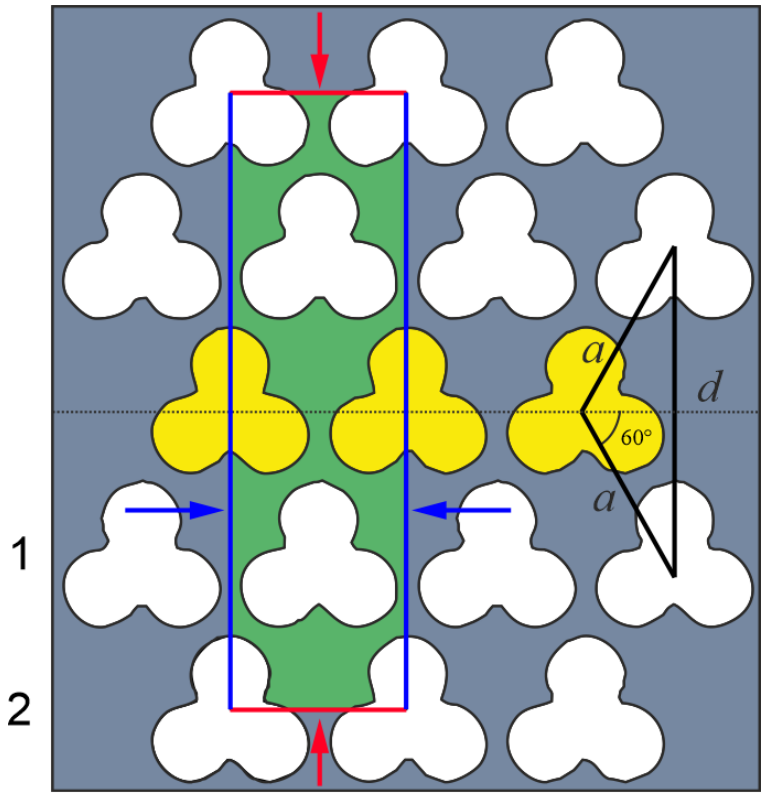

Figure 4.3: Unit cell construction for the shamrock waveguide. a is the period of the structure, d is the shamrock-shamrock distance at the interface. The green area represents the unit cell. Blue arrows indicate the faces for Floquet periodic conditions, red arrows indicate faces for the low reflecting boundary condition in simmulations and the numbers represent the amount of rows to build the unit cell.

The green area indicates the unit cell of the waveguide. The width of the unit cell is a, therefore the reciprocal wavevectors range from 0 to π/a. Blue arrows indicate the faces where the Floquet periodic conditions are applied and red arrows indicate the ends of the waveguide where low reflecting boundary conditions are applied, to avoid the appearance of spurious or reflecting modes. In all simmulations presented here, the unit cell always ends in the middle of the last row of shamrocks as shown figure 4.3 and not in the space between rows. This convention was adopted here because it reduces or avoids the appearance of spurious modes. Finally the numbers indicate the amount of rows used to build the unit cell. For all the configurations, each side of the waveguide has 12 rows.

4.3.2 Band dispersion for shamrock waveguides

Figure 4.4 shows the dispersion relation for the three waveguide configurations presented in figure 4.2, calculated from 0 to π/a (k_x is normalized from 0 to 1). The bands are calculated for the waveguide with period $a = 330$ nm, radius $r = 0.22a$, thickness $t = 220$ nm and $nwg = 0.6$. The three configurations present symmetric and asymmetric guided modes in which the mode deformation is concentrated at the interface as illustrated by the selected mode profiles for $0.8\pi/a$ to the right of each graph.

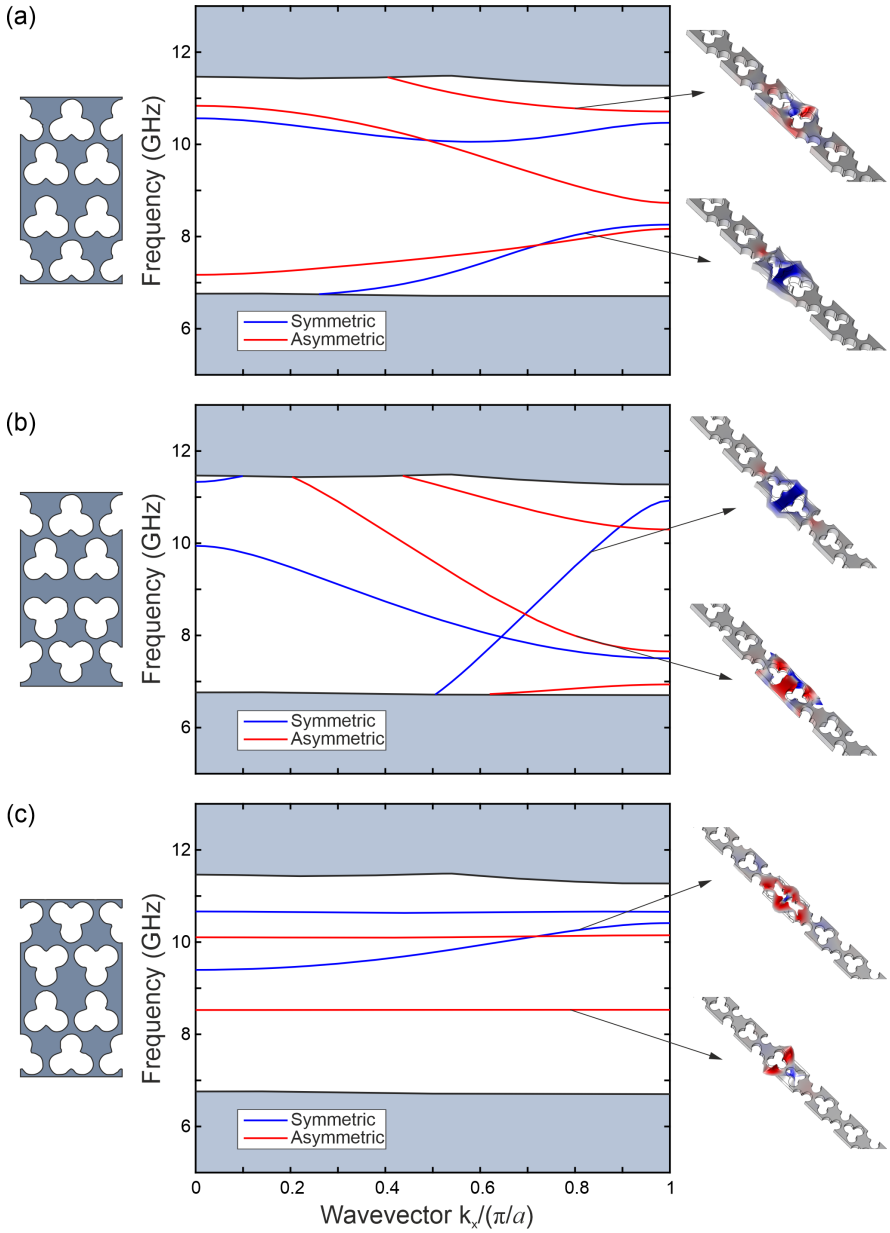

Figure 4.4: Phononic dispersion relation for the three waveguides described in figure 4.2. The gray areas above and below the gap corresponds with the bulk crystal modes. Blue and red curves represent symmetric and asymmetric modes respectively. Insets in the left indicate the type of interface and insets on the right illustrate the mode profile when $k_x/(\pi/a) = 0.8$ for the pointed modes.

Configurations (a) and (b) present five and six guided modes respectively and the modes vary significantly in frequency inside the gap as the wavevector changes. Some of the modes almost completely cross the gap. On the other side, the configuration shown in figure 4.4(c) presents less guided modes than the other two variations, and the curves remains apart except for one crossing of two bands. Beside that, three of the bands seems to be completely dispersionless (flat bands). These characteristics facilitates the identification of modes in experiments and therefore configuration (c) is the most suitable for this study. This configuration allows a better band engineering of the guided modes and it seems that the modes are strongly confined inside the gap.

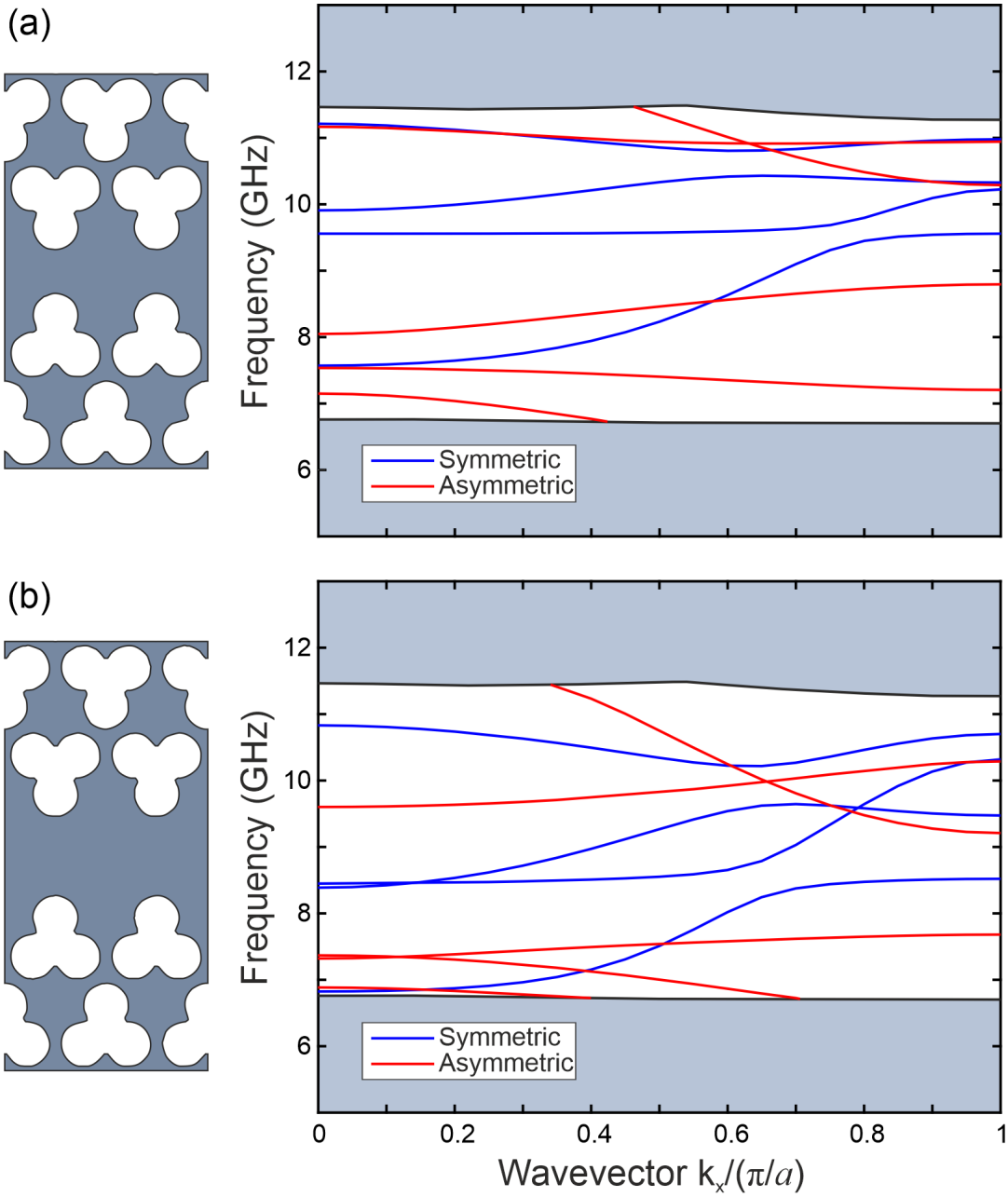

Figure 4.5: Phononic dispersion relation for the front-front waveguide configuration with $nwg = 0.8$ (a), and $nwg = 1$ (b). The bands are calculated for $t = 220$nm, $a = 330$ nm, and $r = 0.22a$.

Once that the waveguide configuration has been defined, it is interesting to see what occurs when the parameter nwg increases. Figure 4.5 shows the phononic dispersion relation for $nwg = 0.8$ (a), and $nwg = 1$ (b) calculated with the same geometrical specifications used to obtain the bands in figure 4.4. As the width of the waveguide increases, more guided modes starts to appear inside the gap. Comparing figures 4.5 (a) and (b), the guided modes appear or enter in the gap from the top edge and decrease in frequency, going to the bottom edge of the gap, as nwg increases.

4.4 Experimental detection of hypersonic guided modes at room temperature

Figure 4.6 shows a SEM image of the shamrock waveguide fabricated in the same SOI platform described in the previous chapter with a thickness of $t = 220$ nm. The period of this structure is $a = 440$ nm, and the radius is the same as in the previous cases $r = 0.22a$. The width of the waveguide is $nwg = 0.8$, which in the fabricated sample corresponds with a minimum waveguide distance of 184 nm as it is indicated in figure 4.6. To calculate this distance from the nominal parameters the expression $w = D - 2(f + r)$ can be used, which results in $w = nwg2a \sin 60 - 2(2/\sqrt{3} + 1)r$.

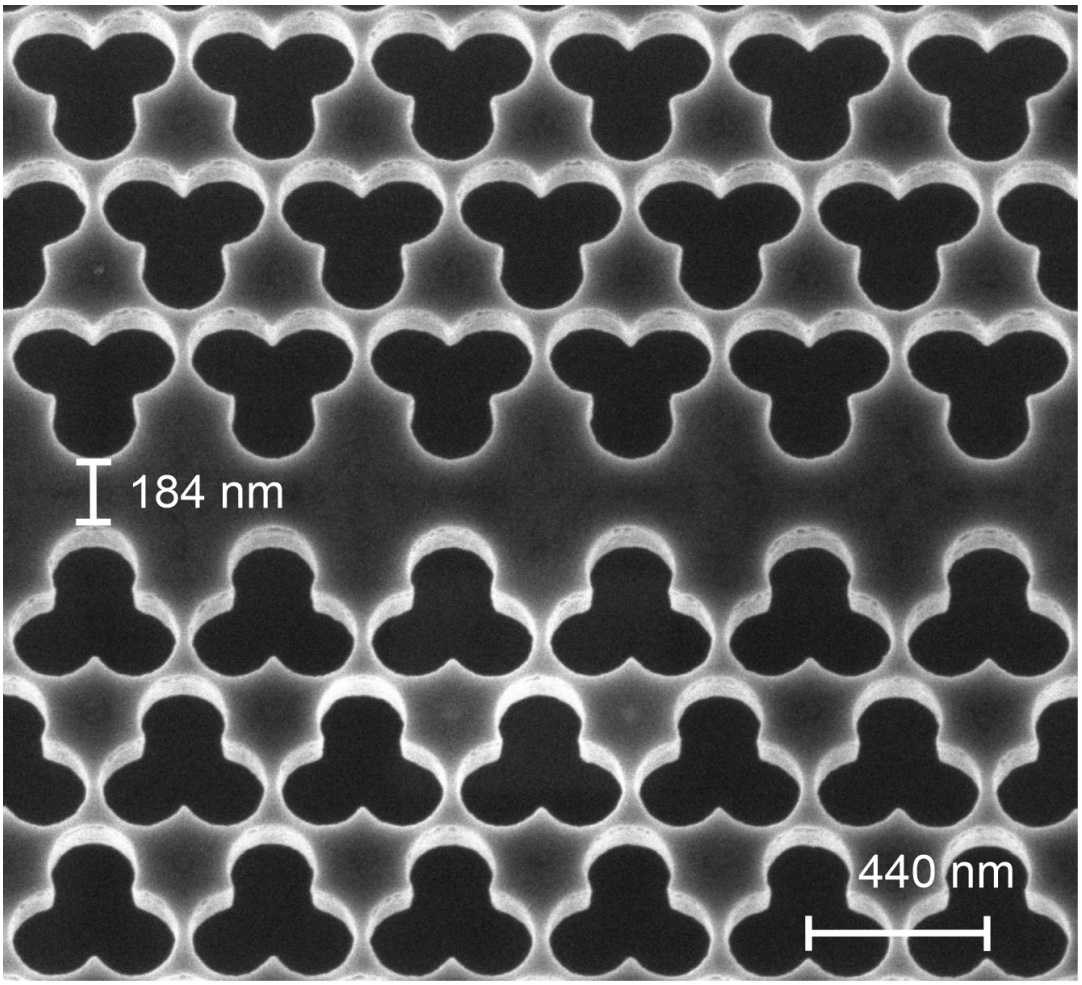

Figure 4.6: SEM of the fabricated shamrock waveguide with $a = 440$ nm and $nwg = 0.8$. The minimum shamrock distance at the interface is $w = 184$ nm.

Figure 4.7 shows the Brillouin spectra measured on the waveguide (top) and on the surrounding phononic crystal (bottom), as specified in the insets, taken at the same incident angle of 23.8°. The blue region indicates the phononic band-gap of the structure. The two peaks measured within this gap in the top panel at 5.7 GHz and 7.1 GHz are clear experimental evidence of mechanical vibrations confined in the phononic waveguide.

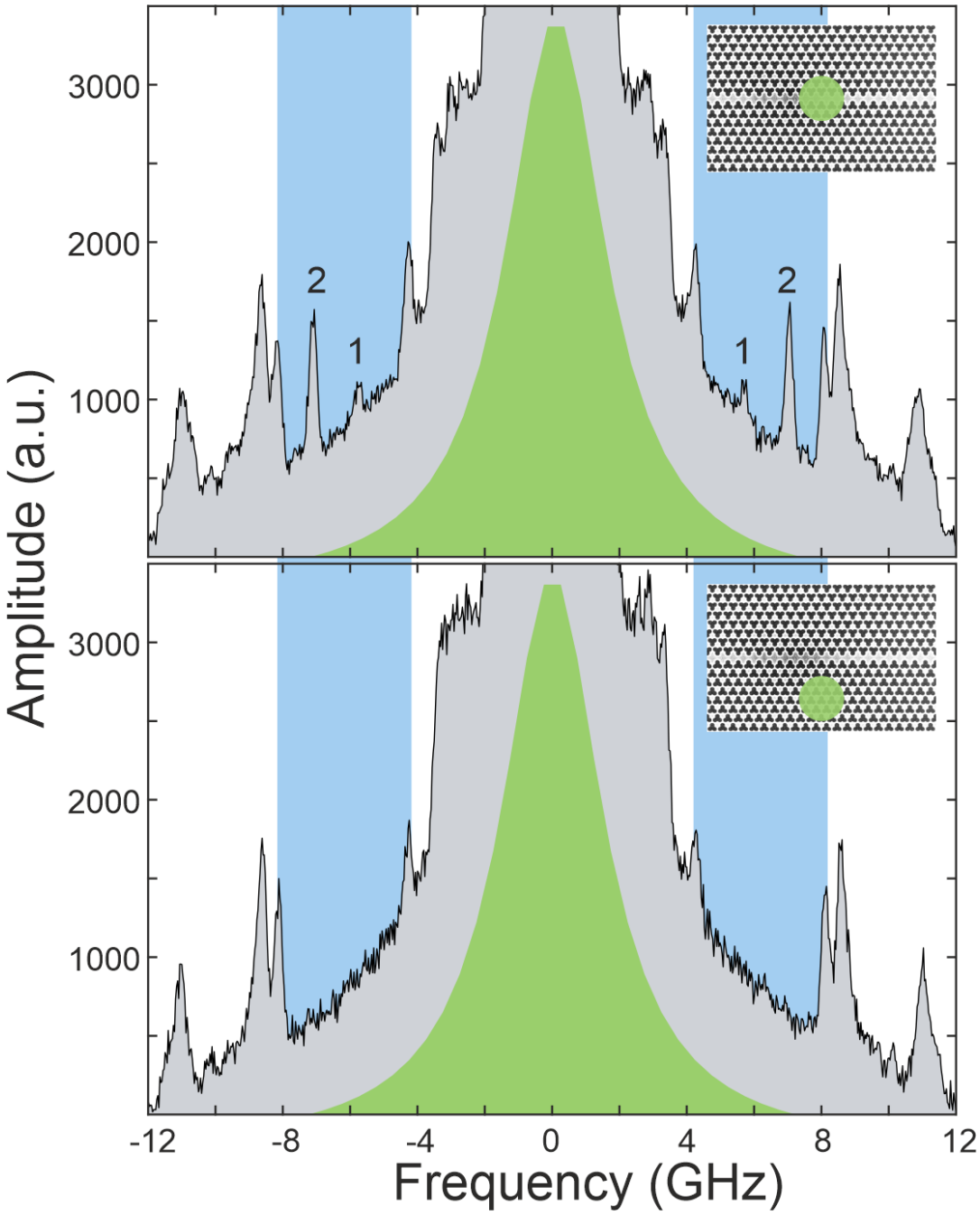

Figure 4.7: Measured Brillouin scattering spectra in the waveguide (top) and surrounding phononic crystal (bottom) as is illustrated in the insets, for an incident light angle of 23.8°. The spectral width of the measured gap is indicated by the blue regions. Two peaks whose frequencies correspond with the guided modes of the system appear inside the gap in the spectrum of the waveguide (top).

To detect these confined modes, it is necessary to focus the light on the waveguide with a long-working distance microscope objective to reduce the spot size of the incident light down to 1.2 μm. In doing so, we reduce the contribution of the Brillouin scattered signal from the crystal while increasing the contribution from the waveguide. For the measurements of these waveguide structures, the background is higher due to a greater collection of reflected and linearly scattered light relative to that of the 3 cm focal length lens used to measure the crystals described in the previous chapter.

Figure 4.8 plots the dispersion relation of the waveguide accounting for the 4° correction of the vertical sidewalls. The same angle correction described in chapter 3 was implemented here because the structures where fabricated on the same chip. The color intensity of the bands corresponds to the normalized coupling coefficient for the moving-boundary perturbation. The fully shaded regions above and below the gap correspond to the bulk crystal modes and define the band-gap edges of the structure. The calculated dispersion relation exhibits nine guided modes but only two (which are indicated with their associated mode profiles) are detected in the experiment. We attribute this to be because of the elastic displacement of these modes, which is predominantly out-of-the plane, while the other calculated guided modes displace the structure primarily in-plane.

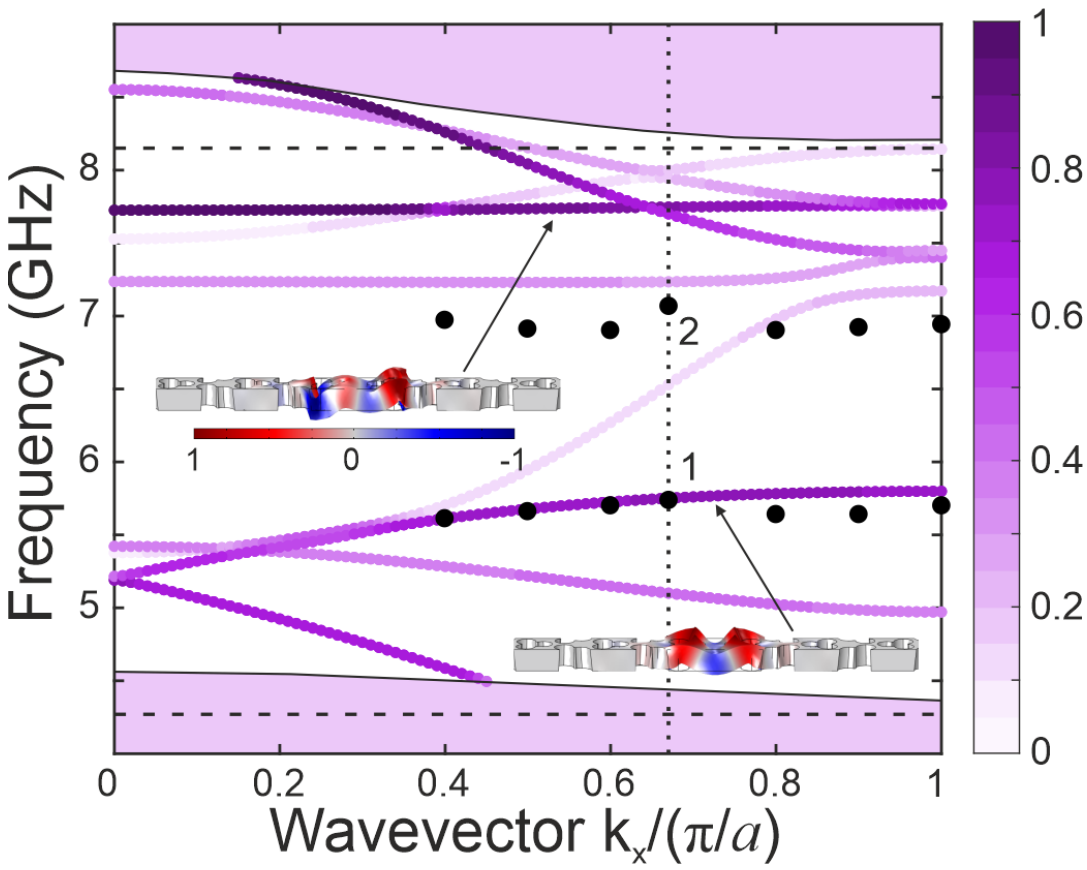

Figure 4.8: Calculated dispersion relation of the waveguide. The intensity colour scale represents the normalized coupling coefficient for the moving-boundary perturbation. The horizontal and vertical dotted lines indicate the mechanical band edges and phononic wavevector, respectively, while the black dots represent the frequencies of measured peaks. The insets show the mode profiles for the indicated bands where the colour represents the normalized out-of-plane displacement.

The horizontal dashed lines highlight the edges of the band-gap measured in figure 4.7, and the black dots correspond to the frequencies of the guided modes measured at different angles. The angle $\theta = 23.8°$ corresponds to a normalized wavevector of 1.34. this number is obtained from $q_{\parallel} = \frac{n\pi}{a} = \frac{4\pi}{\lambda}\sin\theta$ and solving n, or $k_x/(\pi/a) = 0.66$ over the first periodic zone of the waveguide. The two black dots (1 and 2) coincide with the measured frequencies and wavevector in figure 4.7. We assume that the measured peak around 7 GHz corresponds with the darker flat mode around 7.7 GHz and not with the lighter curve that it is spectrally closer to.

There is a difference of approximately 700 MHz for this band while the other peaks agree very closely with the calculated band. A possible explanation comes from figure 3.22(b); the upper limit of the measured gap is shifted in frequency with respect to the calculated bands. Therefore the guided modes inside the gap also will be shifted to a lower frequency. The lower limit of the measured gap has a better agreement with calculated bands, compared with the upper edge of the gap, and it is also extended to the lower detected guided mode in figure 4.8. The detection of these two modes is a clear fingerprint of the existence of guided modes along the Shamrock waveguide.

4.5 Conclusions

This chapter gives detailed information of the waveguide design and experimental evidence of hypersonic guided modes. The main conclusions are summarized below

- A direct consequence of the gap tunability is the frequency tunability of the guided modes. It offers flexibility in the design of structures looking for specific technological applications.
- From the three possible configurations of shamrock waveguide, the front-front configuration offers the best mode confinement, in addition to being the ideal case for experimental detection due to the large interfacial area relative to the other configurations. It increases the possibility to detect scattered photons coming from the interface.
- Experimental detection of guided modes is more complicated than crystal band structure characterization. Only a few of the guided modes scatter enough light to be experimentally detected.
- The guided modes reported in this work were measured at room temperature and with no external excitation. The device is vibrating just by the action of thermally excited phonons. This result says that it is possible to engineer the frequency of the guided mode and the phononic waveguide can carry information as a passive device.

Chapter 5

Quantum spin Hall effect in optomechanic crystals

5.1 Introduction

Topological bosonics has been garnering significant attention due to the promise of back-scattering free propagation of information, resulting from topologically protected states. While significant advancements have been made in topological photonics and phononics independently, a platform which combines the two could lead to improved understanding and applications involving fundamental light-matter interactions between trivial and topologically protected bosons. The design of topologically protected photonic and phononic crystal insulators is presented in this chapter brought together onto one platform based on the quantum spin hall effect (QSHE) at the nanoscale. How topological insulators and ordinary insulators can be obtained in both the optics and mechanics is demonstrated by a simple tuning of the geometric parameters.

5.2 Approaches to obtain Topological Invariants for bosonic systems

The topological properties of the eigenstates of an insulator depend strongly on the symmetries of the system. Symmetry and topology are strongly linked to each other [66]. While symmetry tells us what operations leave the system invariant, topology is invariant under a set of continuous transformations. Indeed, breaking particular symmetries of the system may induce a topological phase transition. The most prominent and first observed approach is the breaking of the time-reversal symmetry in certain solids by the presence of an external magnetic field, referred as the quantum Hall effect [22]. This is not the only type of topological insulator. By breaking spatial or parity symmetries, it is possible to induce further types of topological insulators: the quantum Spin-Hall effect or the quantum Valley-Hall effect. There is an ever increasing variation of topological insulators [67] which have inspired analog insulators for bosons – electromagnetic radiation or mechanical vibrations in solids. For each existing topological insulator originated from a particular symmetry breaking, probably a counterpart in photonic and phononic systems will exist.

5.3 Pseudospin for light and mechanical vibrations

Breaking time-reversal symmetry in optics and mechanics is challenging. While magnetic fields strongly act on charged fermions, the physical effects that induce such a breaking for light are in general very weak. The first attempts to obtain photonic topological insulators exploited the Faraday effect in dielectric nonreciprocal media [28]. An alternative approach to obtain a topological insulator without the application of an external magnetic field is the quantum Spin-Hall effect [68]. However, this imposes another challenge: bosons have integer spin meaning that the bosonic quantum-spin Hall effect cannot naturally guarantee Kramers degeneracies. To induce a Bosonic analogue of the quantum-spin Hall effect, an artificial pseudospin must be engineered by polarization or modal hybridization [69]. The main idea under this approach is to obtain a system with a double dirac point in Γ with four degenerate modes that will serve as a basis to build up the two opposed artificial pseudospin with different polarization or modal properties. The system is modified geometrically to split the double Dirac point and create a gap in which two topological edge modes with the artificial pseudospin will appear. This has been achieved experimentally, both for THz photons [70, 71] and KHz phonons [72], independently.

5.4 Shamrock optomechanic topological crystal

Here the design towards achieving an analogue of the quantum spin Hall effect is described for both GHz phonons and THz photons within the same nanostructure. This design follows the strategy presented in reference [69] where a honeycomb lattice is deformed to create two crystals with different topological invariants that allows the appearance of topologically protected edge modes. The hexagonal array of shamrocks presented here combines the results of a hexagonal array of triangles [70, 71], that produces a topological optical interface, and the results of a hexagonal array of circles [72], that produces a topological mechanical interface. Figure 5.1(a) shows the projected geometry composed of the same shamrock feature described in the previous chapters. The material should be isotropic to not introduce any anisotropy that can break the symmetry along any direction of the superimposed periodic structure. The nominal thickness of the 2D membrane is $t = 250$ nm.

This periodic structure can be seen as a triangular array of parallelograms each with two shamrock holes as shown in the red inset. The resulting period of such a unit cell is s, also indicated in red. The same crystal also can be arranged to have a unit cell composed of a triangular array of hexagons with six shamrock holes inside as indicates the blue inset in figure 5.1(a). The period of this array is a, that is related to s by $a = \sqrt{3}s$, and the size of the large unit cell (blue) is three times the size of the small unit cell (red). When the considered material to build the optomechanic insulator is isotropic, the sides of the hexagon s must be integer multiples of the thickness t; otherwise the mechanical topological behavior will not be present. For the model of isotropic silicon considered here $s = 2t = 500$ nm.

Figure 5.1(b) details the hexagonal unit cell. p is the distance from the center of the unit cell to the center of each shamrock as indicated by the circle. This distance is one third the period, $p = a/3$, as indicated by the light blue lines in 5.1(a). The radius of each circle composing the shamrock is parameterized in terms of the side of the hexagon, $r = nr \cdot s$, and $f = 2r/\sqrt{3}$ as before.

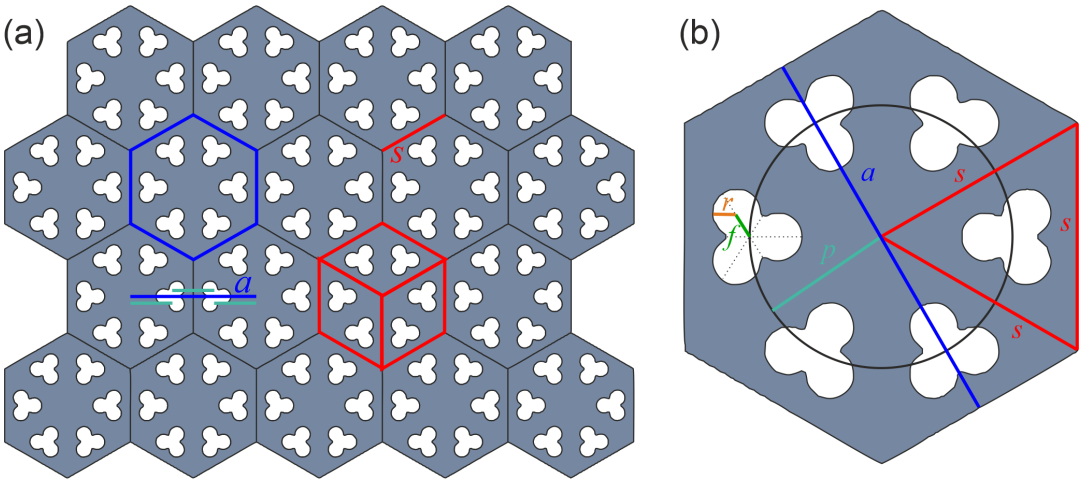

Figure 5.1: (a) Hexagonal array of shamrocks in a 2D silicon membrane. This crystal can be seen either as a triangular array of parallelograms with period s (red), or as a triangular array of hexagons with period a (blue). (b) Hexagonal unit cell of shamrocks. $t = 250$ nm, $s = 2t$, $a = \sqrt{3}s$, $p = a/3$, $r = nr \cdot s$, $f = 2r/\sqrt{3}$.

For the purpose of comparing the difference of choosing the small or big unit cell, the mechanical and optic dispersion relation will be considering in each case. Figure 5.2 shows the mechanical (a), and optical (b) dispersion relation calculated for the crystal described in figure 5.1, obtained from the simmulation of the small (red) unit cell. For this calculation $nr = 0.117$, which gives a shamrock radius $r = 58.5$ nm. The mechanical dispersion relation in figure 5.1(a) is duplicated along the x axis (dimensionless wavevector), to demonstrate the existence of a double Dirac point in Γ at 6.6 GHz. Consequently, this means that there will be four different modes with the same frequency in Γ.

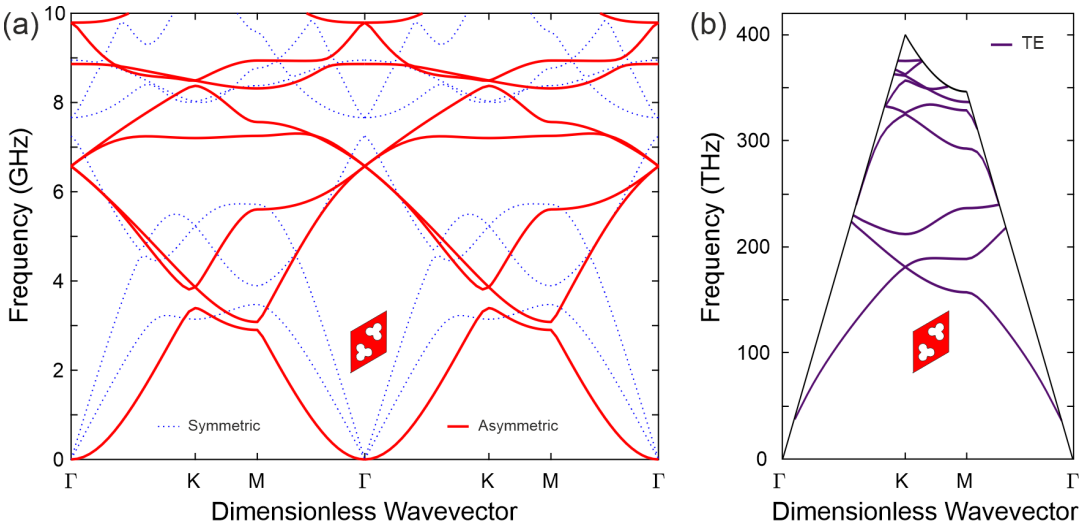

Figure 5.2: (a) mechanical dispersion relation for the small unit cell shown in the inset. There is a double Dirac point in Γ at 6.6 GHz. (b) Optical dispersion relation for TE modes also considering the small unit cell. There is a single Dirac point in K at 181.2 THz.

From the optical dispersion relation for TE modes in figure 5.1(b), there is a single Dirac point (two modes with the same frequency), in K at 178.5 THz. For the

emulation of the QSHE, the existence of a double Dirac point in Γ is necessary to hybridize two pair of modes and obtain two interface modes with artificial pseudo spin. The mechanical dispersion relation already fulfills this requirement. To have a hybrid insulator, the optical dispersion relation also needs to have the two Dirac points in Γ. To solve this issue, it is necessary to obtain the dispersion relation considering the large hexagonal unit cell.

Figure 5.3 shows the mechanical (a), and optical (b) dispersion obtained from the simulation of the hexagonal (big) unit cell. For the mechanical dispersion relation, the double Dirac point in Γ at 6.6 GHz remains unchanged. For the optical dispersion relation, a double Dirac point in Γ appears at the same frequency of 178.5 THz. This change in the dispersion relation is a consequence of the band folding in reciprocal space [69].

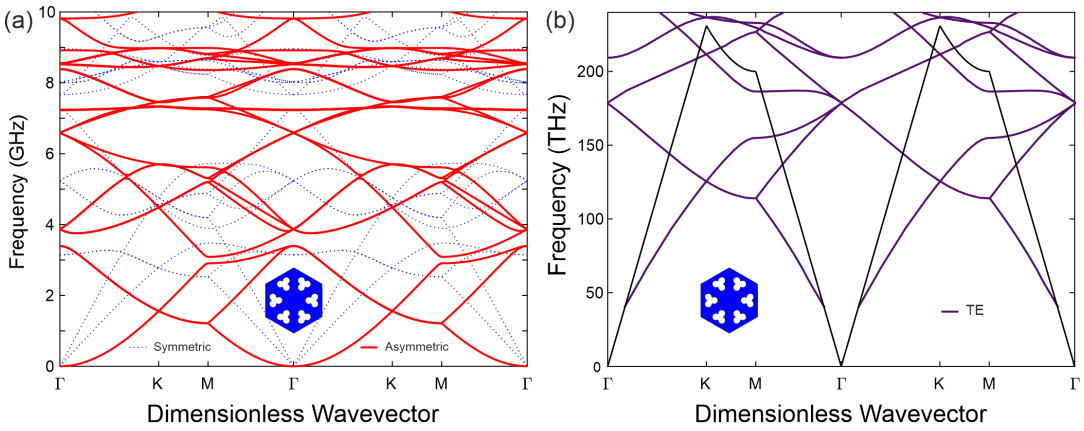

Figure 5.3: (a) mechanical dispersion relation considering the hexagonal unit cell. The double Dirac point in Γ remains at the same frequency. (b) Optical dispersion relation for TE modes also considering the hexagonal unit cell. In this case there is a double Dirac point in Γ at the same frequency of 178.5 THz.

5.5 Band folding

To illustrate the origin of the double Dirac point in Γ when the hexagonal unit cell is considered, figure 5.4 shows the optical dispersion relation for small (red) and big (blue) unit cells, and their respective Brillouin zones. Given that the Brillouin zone is inversely proportional to the period of the structure ($|\Gamma K| = 4\pi/3a$), the red unit cell will have a bigger Brillouin zone. It is tilted with respect to the blue one 30 degrees because the small unit cell is also tilted 30 degrees in the direct space with respect to the big one.

The dispersion relation in the small unit cell is considered along the $\Gamma KM\Gamma$ path, indicated by the green, yellow and purple segments in the reciprocal space. The green ΓK path in the red Brillouin zone is equivalent to the $\Gamma M\Gamma$ path in the blue Brillouin zone, as the green arrow also indicate in the dispersion relation on the right. Therefore, the Dirac point located in K for the small unit cell is now in Γ considering the big unit cell. The yellow segment KM in the red Brillouin zone is equivalent to the ΓM path in the blue unit cell. Finally, the purple path $M\Gamma$ in the red Brillouin zone is equivalent to the $MK\Gamma$ path in the blue Brillouin zone. This is also evident if

the reciprocal space is artificially folded along the dashed gray line. the yellow path will coincide with the position of the ΓM path in the first and centered blue hexagon.

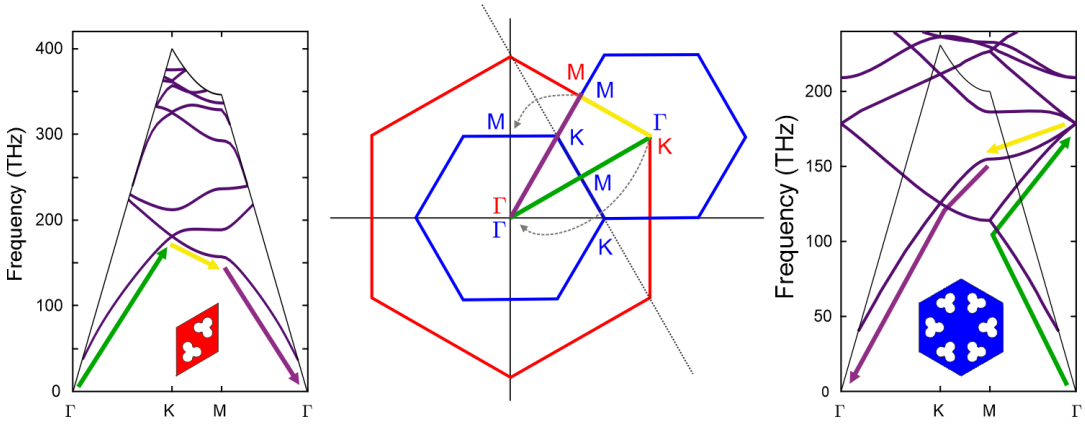

Figure 5.4: Band folding scheme considering the optical dispersion relation for the small (left) and big (right) unit cells. The central scheme shows the Brillouin zone for both unit cells and also the high symmetry points in each case. The green, yellow and purple $\Gamma KM\Gamma$ path in the Brillouin zone corresponds with the $\Gamma M\Gamma MK\Gamma$ path in the blue Brillouin zone.

5.6 Opening a gap for the double Dirac point

Once there is a system that fulfills the requirements to have a double DP for the mechanical and optical dispersion relations, the next step to create topological edge modes is to perturb the system to open a gap inside the double DP and obtain two different topological insulators in which the mode profile for the upper and lower bands of the gap are inverted in both insulators. The way to do that is to displace the shamrocks inwards and outwards as shown figure 5.5.

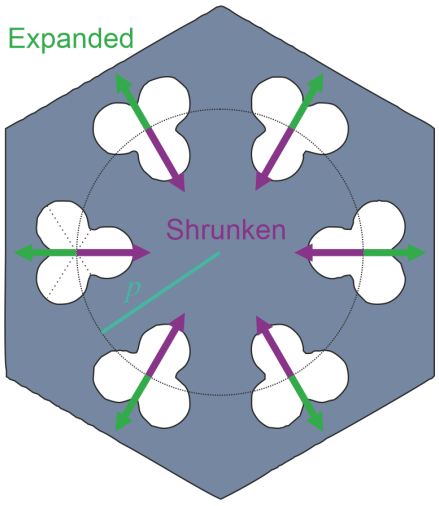

Figure 5.5: Unit cell perturbation to split the Dirac point. All the shamrocks move inwards the same distance (shrunken), or all the shamrocks move outward (expanded).

When all the shamrocks are displaced inwards or outwards, the unit cell is called shrunken or expanded respectively. Once the center of the shamrocks does not coincide with the position p, it is no longer possible to replicate the crystal with the small unit cell, only with the hexagonal one. The displacement of the shamrocks is given in terms of p as $R = np \cdot p$, where R is the distance from the center of the hexagonal unit cell to the center of each shamrock and np is an scalar. np greater than one means expanded and less than one means shrunken. Therefore it is possible to obtain two different crystals, one with the shrunken unit cell and another with the expanded unit cell. Figure 5.6 presents the mechanical and optical dispersion relation for shrunken ($np = 0.95$) and expanded ($np = 1.05$) crystals, only in the vicinity of the Γ point and with frequency close to the DP.

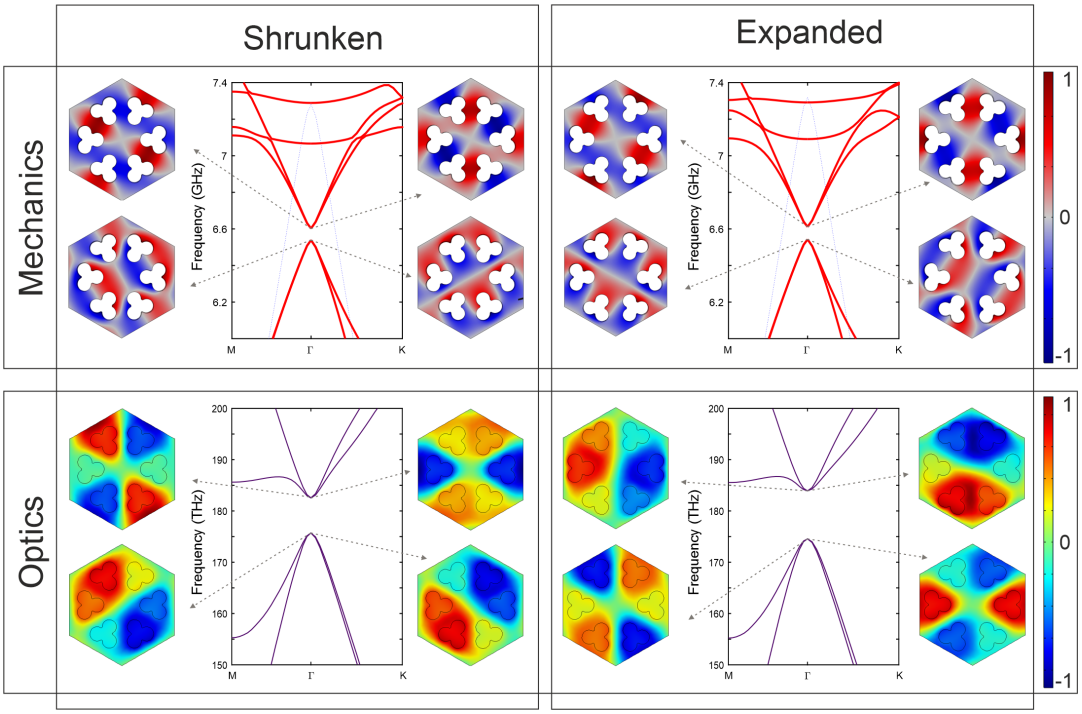

Figure 5.6: Mechanical and optical dispersion relation for the shrunken ($np = 0.95$) and expanded ($np = 1.05$) crystals. The inset shows the mode profile for the out of plane displacement, U_z for the mechanics, and out of plane magnetic field, H_z, for optics. There is band inversion for the optical profiles but it is not achieved for the mechanical profiles.

For all the cases it is possible to open a gap. For the shrunken crystal, the gap opens from 6.54 to 6.60 GHz for the mechanics and from 175.7 to 182.6 THz for the optics. For the expanded case, the mechanical gap opens from 6.54 to 6.61 GHz and the optical gap from 174.6 to 183.9 GHz. The insets display the mode profiles at the edges of the gap as the dashed arrows indicates. For the mechanical part, the out of plane displacement U_z is shown, and for the optical part, the out of plane magnetic field H_z is shown. From the optical part it is possible to observe that the mode profiles appearing in the lower bands for the shrunken case, appear in the upper bands for the expanded case, and vice versa. This is the band inversion for the shrunken and expanded crystals. On the other side, with the mechanical mode profiles is not happening the same. Besides the existence of a gap inside the double DP, the band inversion is a requirement to build a topological interface waveguide. This phenomena can be explained with bulk-edge correspondence.

5.7 Chern number and bulk-edge correspondence

Topologies for photonic and phononic systems are defined on the dispersion bands in the reciprocal space. The Chern number C is the topological invariant of a 2D dispersion band, as the systems presented here. This number characterizes the quantized collective behavior of the wavefunctions on each band [73]. Once the bands are defined in terms of a topological invariant, they change only discretely and will not respond to continuous small perturbations [23, 24, 74–79]. This is the case of a ball and a spoon, or a donut and a mug; the latter couple have one hole ($g = 1$), and the former have no holes ($g = 0$). They are topologically equivalent despite the differences in shape.

The numerical calculation of the Chern number for the system presented in this chapter is out of the scope of this work; but it can be deduced by analogy from similar works in photonics [70, 71] and phononics [72]. These references state that the Chern number for the four bands that splits to form the gap are $C = 0$ for the shrunken geometry and $C = \pm 1$ for the expanded case. Crystals with $C = 0$ are denominated trivial or ordinary insulators (OI) and crystals with $C \neq 0$ are denominated non-trivial or topological insulators (TI). The topological edge modes appear at the interface of two crystals with different topological invariant or Chern numbers as in the system shown in figure 5.7(a), composed of a shrunken crystal (OI), joined with a expanded crystal (TI).

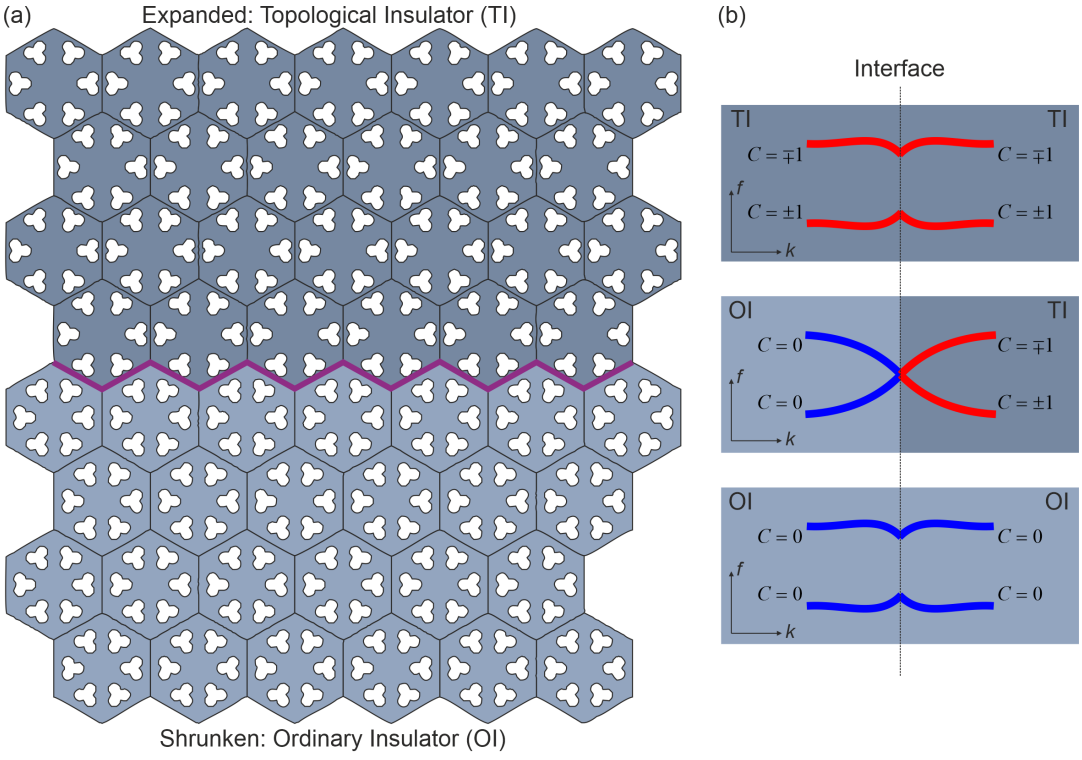

Figure 5.7: (a) Topological waveguide, highlighted in purple, formed at the interface of a ordinary insulator (OI) and a topological insulator (TI). (b) Topological phase transitions at the interface of OI and TI insulators. Blue and red curves represents bands with $C = 0$ and $C = \pm 1$ respectively. The gap has to close at the interface of a OI-TI system to equalize the Chern numbers. It ensures the existence of topologically protected edge modes.

In this system there is no space between both crystals acting as the waveguide. Here the waveguide is the interface highlighted in purple that is topologically different from a trivial waveguide, composed by two crystals with the same topological invariant. If the two crystals have the same Chern number, they can directly connect across the interface without closing the frequency gap. This is illustrated in figure 5.7(b). The background color indicates the crystal geometry and blue and red curves indicate bands in the reciprocal space with Chern numbers 0 and ± 1 respectively. In the upper (TI-TI) and lower (OI-OI) case, bands do not need to close to equalize the Chern numbers.

If both crystals have different C, as the case illustrated in the middle of figure 5.7(b), will exist necessarily a topological phase transition at the interface. The gap will close, all the Chern numbers will be neutralized, and then the gap will open again. This phase transition ensures edge states at the interface of both crystals and their existence is guaranteed by the different topological invariant on each side of the interface. The number of edge modes appearing at the interface is the difference of the Chern numbers associated with the bands below the gap [73, 80, 81]. In the system studied here, there are two bands in the lower part of the gap with $C = \pm 1$ (TI), that interfaces with two bands with $C = 0$; therefore there will be two modes appearing at the interface. This is known as the bulk-edge correspondence principle [80, 82].

5.8 Band inversion for phonons and photons

Considering the hexagonal shamrock system presented in figure 5.6, the band inversion for the photonic profiles suggest that both crystals have different Chern numbers, being $C = 0$ for the shrunken and $C = \pm 1$ for the expanded. on the other hand, the absence of band inversion for the phononic profiles suggest that both crystals have the same topological invariant and therefore the existence of topological edge modes will not be ensured.

From numerical simulations of the phononic dispersion relations, by decreasing the size of the shamrocks, placed at the fixed position p with the same period and thickness, a frequency bandgap started to appear. Even more interesting was the observation that by displacing the smaller shamrock around the position p, the gap started to close again. This fact suggests that reducing the size of the shamrocks causes a change in the position of the DP. For the photonic dispersion relations is not the same case because the DP is always at position p, no matter if the shamrocks increases or decreases in size. For example, when reducing the radius of the shamrock from $0.117a$ to $0.110a$, the DP moves from position p to position $1.06p$. There is another DP on the opposite position with respect to p at $0.94p$. Figure 5.8 illustrates this for the mechanical (a), and optical (b) cases and the inset represents the A, p, and B positions in the unit cell. The y axis indicates the frequency, and DP indicates the frequency at which the blue and red bands closes. The bands are indicated with different colors to represent the different mode profiles.

From the optical part in figure 5.8(b), mode profiles invert in p as shown figure 5.6. For the mechanical part, the band inversion has a different and interesting behavior. The mode profiles change with the position A with a maximum gap width at p. The gap once again closes in B, and the mode profile once again varies at distances greater than B. This particular behavior can help to understand what happens when the DP

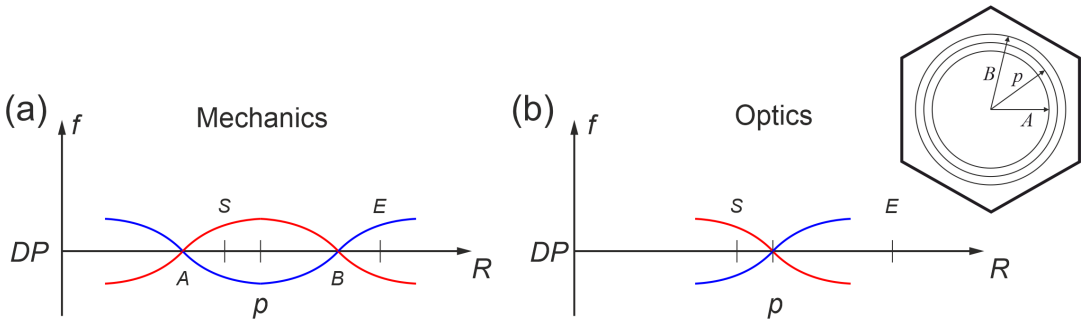

Figure 5.8: (a) Mechanical and optical (b) band inversion around the DP as the radial distance of shamrocks changes. There is a double band inversion for the mechanical profiles at points A and B. S and E represents the optimal positions for shrunken and expanded respectively, for a hybrid topological crystal.

is located at p. If the radius of the shamrock is increased from $0.110a$ to $0.117a$, points A and B start to get closer to p and finally coincide for $r = 0.117a$. This means that the mode profile for frequencies higher than the DP always will be blue, and red for lower frequencies, as observed in figure 5.6.

Therefore choosing a distance greater than B is necessary for the expanded case to have blue profiles above the DP, both in optics and mechanics (position E), and a distance between A and p to have red profiles above the DP in optics and mechanics (position S). There are three constraints for the optimal design: first, the position E can no be to far from p because the optical gap starts to lose its shape. Second, the position S can not be to close to p because the optical gap will be to small. Third, the positions A and B can not be to close to p because the mechanical gap will be to small.

With all these constraints we have chosen for our hybrid model $r = 0.110a$, $S = 0.97p$, and $E = 1.08p$, considering the same period $a = \sqrt{3} \cdot 500$ nm, and thickness $t = 250$ nm. The mechanical and optical dispersion relations for this system are presented in figure 5.9. In this case it is possible to infer that the topological invariants are different for both crystals, being $C = 0$ for shrunken, and $C = \pm 1$ for expanded. This is an optimal system to obtain phononic and photonic topological edge modes simultaneously at the same interface.

5.9 Mode hybridization and topological helical states

The four modes that compose the edges of the gap hybridize into two modes that form an orthogonal basis for the topological guided modes. To illustrate this, the mechanical mode profiles are presented in figure 5.10. The degeneracy of the bands on each side of the DP correspond to p_x, p_y (-like) and d_{x2-y2}, d_{xy} (-like) crystal modes which are similar to p and d orbitals of electrons [72]. These modes are classified with respect to the symmetry of the axes x' and y', $\sigma_{x'(y')} = \pm 1$, being even (+1) or odd (-1) with respect to x' or y' axis. Here $\sigma_{x'}, \sigma_{y'}$ = 1,-1; -1,1; 1,1; and -1,-1, for p_x, p_y, d_{x2-y2}, and d_{xy} respectively. The pair p_x and d_{x2-y2} hybridize to form a symmetric mode S, and the pair p_y and d_{xy} hybridize to form an asymmetric mode A, both with respect to y.

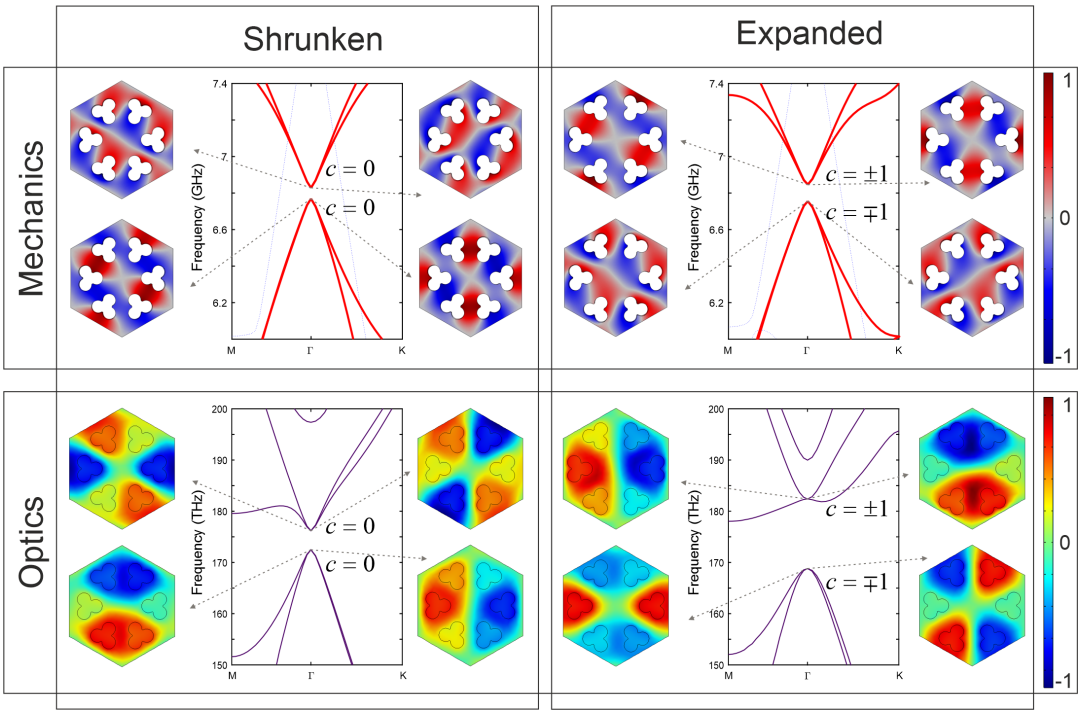

Figure 5.9: Mechanical and optical dispersion relation for the shrunken ($np = 0.97$) and expanded ($np = 1.08$) crystals. The inset shows the mode profile for the out of plane displacement, U_z for the mechanics, and out of plane magnetic field, H_z, for optics. There is band inversion for optical and mechanical mode profiles profiles.

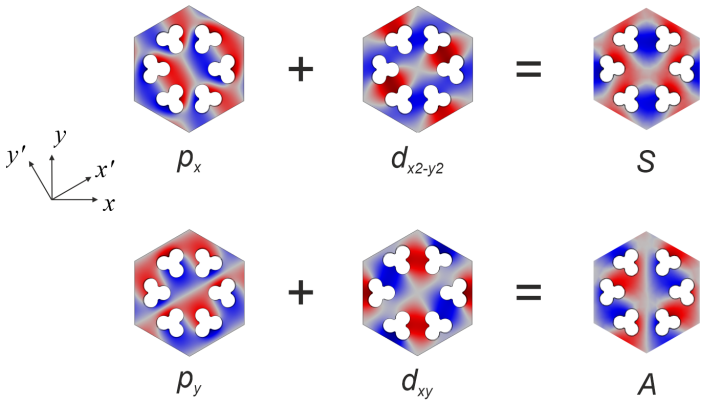

Figure 5.10: Representation of the mechanical mode hybridization. Both of the modes from the upper and lower band hybridize respectively to form two new orthogonal modes that are the basis of the two topological helical edge modes.

Figure 5.11(a) shows the phononic dispersion relation of asymmetric modes for the waveguide composed of the shrunken ($np = 0.97$), and expanded ($np = 1.08$) system presented in figure 5.9. There are two guided modes inside a small gap spanning 6.75 GHz to 6.92 GHz represented with purple and green dots. The insets show the mode profile of each mode, the helicity, and the artificial elastic pseudospin. To understand the helicity of these modes, figures 5.11 (b) and (c) show the temporal evolution of the edge modes over half a period, divided in seven equally spaced frames. For the mode represented with purple points, at $t = 0$, the mode profile of the guided mode resembles the A mode presented in figure 5.10.

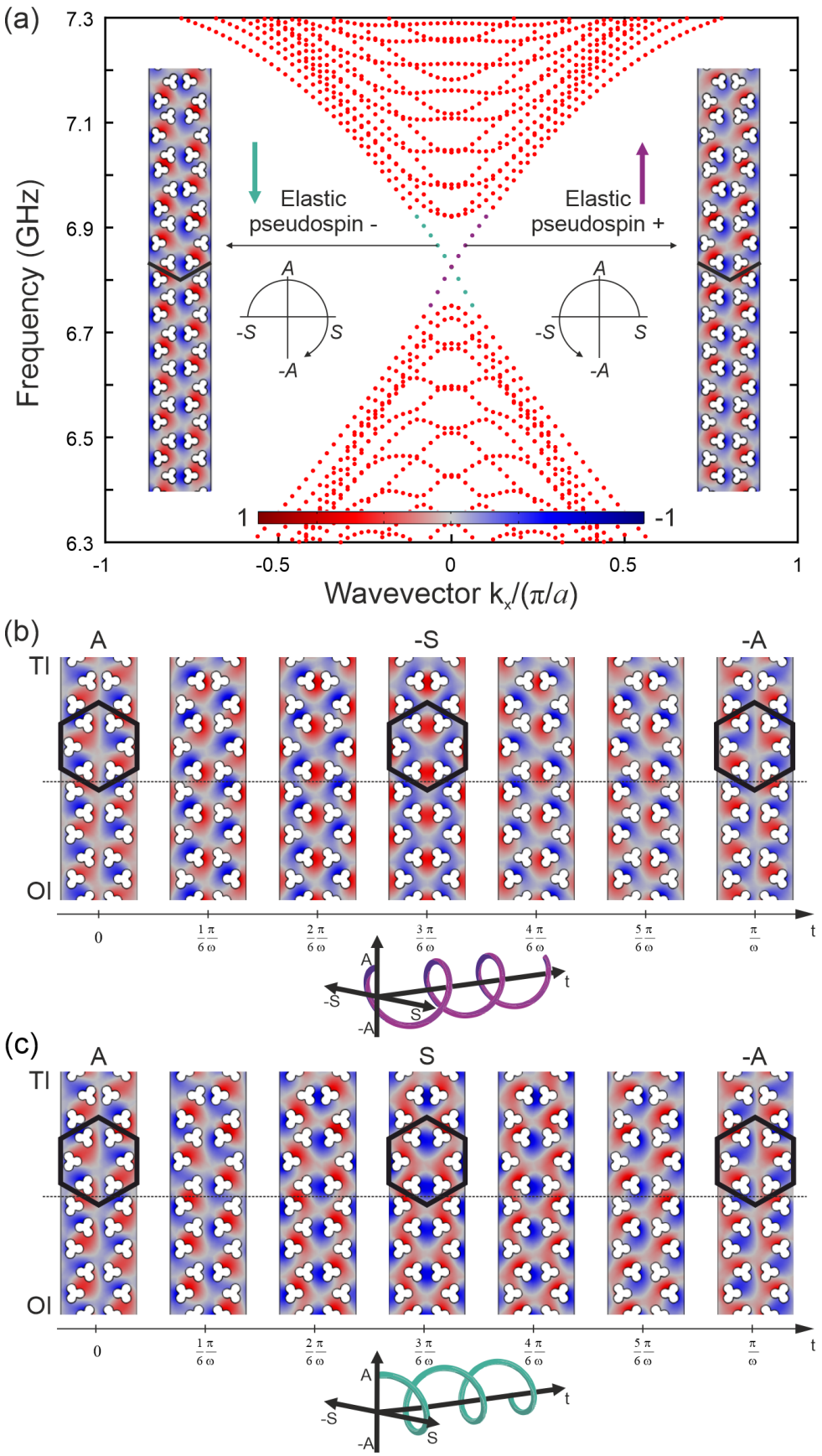

Figure 5.11: (a) Phononic dispersion relation of asymmetric modes for the topological waveguide composed of the shrunken ($np = 0.97$) and expanded ($np = 1.08$) crystals. (b), (c) temporal evolution of the elastic pseudospin up and down respectively.

After a quarter of the period, the mode profile now resembles the S mode but with inverted colors, it means $-S$. Finally after a half of the period, the mode profile resembles the $-A$ mode. This means that the helical mode can be described in terms of the basis S/A as a time-dependent anti-clockwise elastic pseudospin $+$ as $S + iA$. The other mode represented with green dots can be represented as a time-dependent clockwise elastic pseudospin $-$ as $S - iA$. The profile of both modes are the same but evolve in time with different helicity. With the system presented in figure 5.9, there will be four topological modes that can propagate at the interface, two optical and two mechanical modes each of them with different helicity which also favors the nonreciprocal wave propagation.

5.10 Samples fabrication and experimental limitations

Figure 5.12 shows a SEM image of the system described in figure 5.9. The structure was made in a nanocrystalline silicon plate with a thickness of 250 nm. This structure imposes different challenges for the experimental characterization. For the mechanical part, the measurements can not be taken with the BLS spectroscopy setup described in chapter 2, because this system can not resolve a small frequency gap of 170 MHz as the one presented in 5.11(a). A good resolution of the frequency gap is necessary to favor the detection of edge modes inside it. Even if the structure is optimized to be not hybrid but just a mechanical topological insulator, the change of the mass distribution by the displacement of the shamrock features inside the unit cell is not enough to open a gap bigger that 250 MHz.

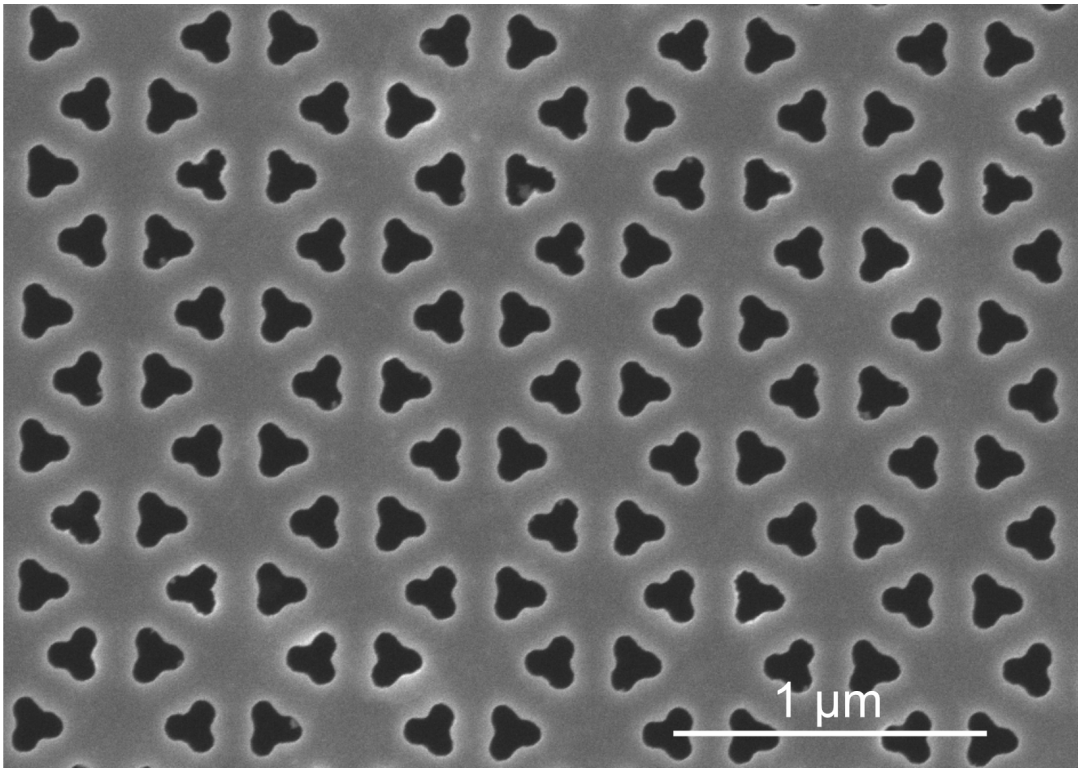

Figure 5.12: SEM image of the fabricated topological waveguide in nanocrystalline silicon.

For the optical part, this kind of structure also present difficulties at the time to be characterized. Figure 5.3(b) shows that the double DP for THz photons is above the light cone meaning that they are leaky and not guided modes. This requires for example, the implantation of quantum emitters inside the system to enhance the out of plane light detection [71], and far-field radiation detection systems [83].

5.11 Conclusions

This chapter presents in parallel the numerical construction of a topological phononic-photonic system based on an hexagonal array of shamrock features. The main conclusions are summarized below

- The necessary requirements that a system must fulfill to support topological edge modes are: a double DP in Γ, splitting of the DP through geometrical perturbation, and band inversion of the edge modes of the structures that composes the interface.
- The position p for the DP in the optical and mechanical dispersion relations, imposes an additional restriction in the design of an hybrid structure.
- Experimental detection of topological modes is challenging. Besides geometrical complexity imposed by the small displacement of shamrock features for shrunken and expanded crystals, the small gap width produced by this mass redistribution is not enough to be measured by the BLS spectroscopy system.

Chapter 6

Quantum Valley Hall efect in phononic crystals

6.1 Introduction

A different approach for the quantum spin Hall effect (QSHE) to obtain topological edge states is the quantum valley Hall effect (QVHE). Both models do not require external gauges as magnetic fields or air flow currents to break the time reversal symmetry. Topology is achieved just by breaking the geometry of the system as was shown in chapter 5 for QSHE. In this chapter the design of topologically protected phononic crystal insulator is presented based on the QVHE at the nanoscale to obtain hypersonic (GHz) topological edge modes. Here the influence of the isotropy in the material is explored to obtain the Dirac points required for the model to develop the Valley approach.

6.2 Valley Hall effect

Hexagonal two-dimensional crystals, such as graphene and transition-metal dichalcogenides, exhibit a pair of degenerate bands at the K and K' valleys in reciprocal space [27]. In the solid state, the valley electrons have non-trivial Berry curvatures, and this fact causes anomalous quantum Hall states in graphene [84]. The same ideas have been translated to bosonic systems to build the Valley Hall analogy in photonic crystals and shows topological protected transport of light at telecom wavelengths [85]. For the case of mechanical waves, the same analogy has been applied to obtain protected transport of phonons at KHz [30], MHz [86] and GHz [31] frequencies. Such Two-dimensional chiral states are topologically protected as long as there are no inter-valley scatterings generated by geometrical defects.

In this chapter it was elaborate the same idea to design a phononic topological crystal that can be fabricated in SOI platform to obtain topological phononic edge states with frequencies above 10 GHz. The process to obtain this is first find a crystal geometry with an isolated Dirac point in K; it generally is found in cystals with hexagonal geometry. After that, break the C_6 symmetry to release the degeneracy of the Dirac point and open a gap, and finally build the interface waveguide to obtain the topologically protected edge mode.

6.3 Valley topological phononic crystal

Figure 6.1(a) shows the Valley Hall phononic crystal with periodic distance a. The unit cell in figure 6.1(b) is inspired once again in the shamrock geometry. The difference with previous geometries is that this time the shamrock is not drilled in the plate, but is now part of the suspended material. the shape of the crystal is composed of the same three tangential circles of radius r but now the geometry is filled in the circle intersections up to the tangential line between each two circles. The final shape is a rounded triangle and the unit cell is composed of two of these rounded triangles inverted among them, separated by a distance s and interconnected with walls of width w.

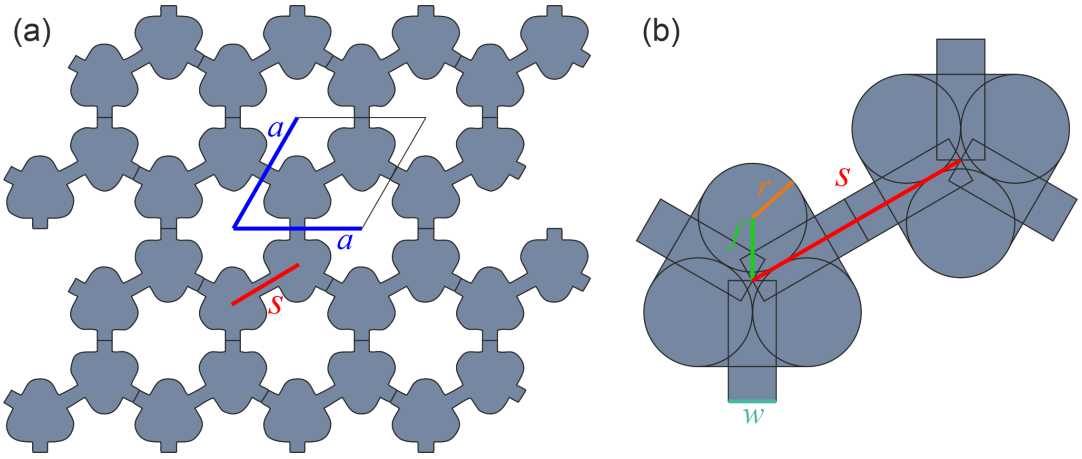

Figure 6.1: (a) Geometry of the valley hall crystal with period a. (b) Unit cell construction based on the shamrock geometry. s is center to center distance or the side of the hexagon in (a), and w is the width of the connectors.

6.4 Isotropic vs. anisotropic silicon

In this section the difference in the phononic dispersion relation between isotropic and anisotropic materials is explored. Here isotropic silicon and [110] x oriented anisotropic silicon is considered. The difference between both materials is the elastic matrix. For the isotropic case, the full matrix can be defined by two independent elastic constants C_{12} and C_{44}, defined as functions of the Young's modulus E, and the Poisson's ratio ν, as $C_{44} = E/2(1+\nu)$ and $C_{12} = E\nu/(1+\nu)(1-2\nu)$. The third elastic constant can be defined in terms of the other two as $C_{11} = C_{12} + 2C_{44}$. For the anisotropic case, the elastic matrix is defined by three independent elastic coefficients.

To make crystal resizing easier, the geometry is parameterized in terms of the center to center distance s. The period of the structure is then $a = \sqrt{3}s$, the radius of each circle is $r = nr \cdot a$, and the width of the walls is defined as $w = nw \cdot s$. The thickness of the structure is defined by t. Figure 6.2 shows the phononic dispersion relation for the designed Valley crystal with $nr = 0.13$ and $nw = 0.2$ and t =220 nm, for Isotropic and [110] oriented silicon. Two different dimensions with $s = 220$ nm and 440 nm are also considered.

For the case of isotropic silicon, there are isolated Dirac points at 8.28 GHz for s=440 nm and 12.66 GHz for s=220 nm. For the anisotropic case, the isolated Dirac point only appears for $s = 220nm$. In terms of fabrication, the E-beam lithography process can be more accurate in larger structures. Therefore the first option is fabricate the structure in nano-crystalline silicon that is supposed to behave as isotropic material and develop the topology on it. But this big structure also introduces some experimental limitations as will be described next.

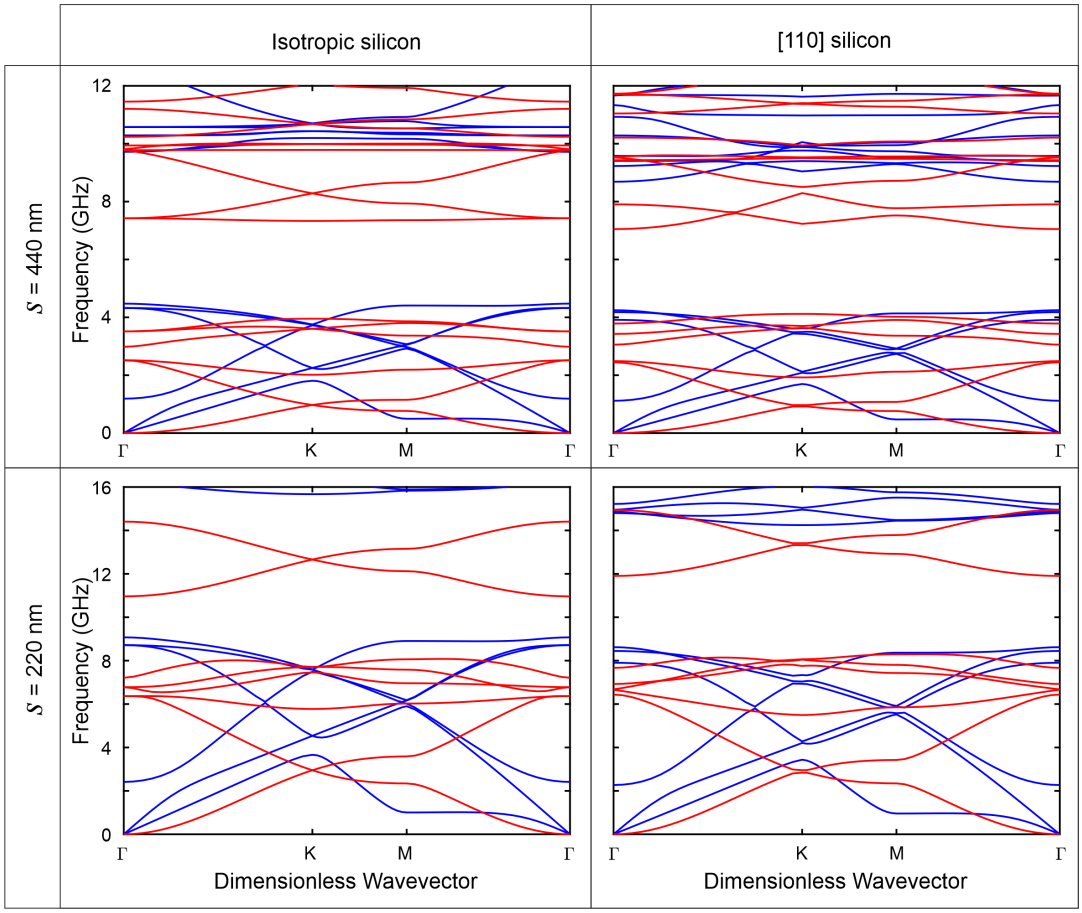

Figure 6.2: Phononic dispersion relation for the designed topological crystal considering Isotropic and [110] oriented silicon. Two crystal dimensions with s= 440 and 220 nm are considered. For the isotropic silicon an isolated Dirac point appears in both sizes. For the anisotropic [110] silicon, only the crystal with s=220 nm presents the required Dirac point to develop the Valley topological approach.

6.5 Linear diffraction for large holed scatters

Figure 6.3(a) shows a SEM image of the designed topological crystal fabricated in nano-crystalline silicon with a thickness of t=220 nm, s=440 nm and period a=762 nm approximately. The radius and the width of the conectors are the same used in the previous simulations. Given the dimensions of the fabricated structure, the size of the drilled holes or scatters is similar or even bigger than the wavelength of the laser (λ=532 nm) used for the experimental measurements. This issue can introduce linear diffraction that interferes in the measurements.

Figure 6.3(b) shows three different measured BLS spectra. The black curve is the BLS spectra obtained when the green lasers hits a flat surface at zero degrees that can be a silver coated mirror or unpatterned silicon. The spectrum is composed of peaks that repeats each 740 MHz approximately and correspond with the intrinsic linear laser scattering. These strong peaks can mask the weak nonlinear scattering coming from the structures intended to be measured. The way to avoid this interference is ensuring that the specular reflection coming from the structure that is being measured, does not enter in the objective or lens used to focus the incident light and collect the back scattered signal. This limitation prevents to take measurements at zero degrees and sets a minimum angle for experimental measurements that can change with the lens or objective used in the experimental setup. For the 50x objective with numerical aperture of 0.45 used in this measurements, the minimum angle of measurements is 16 degrees.

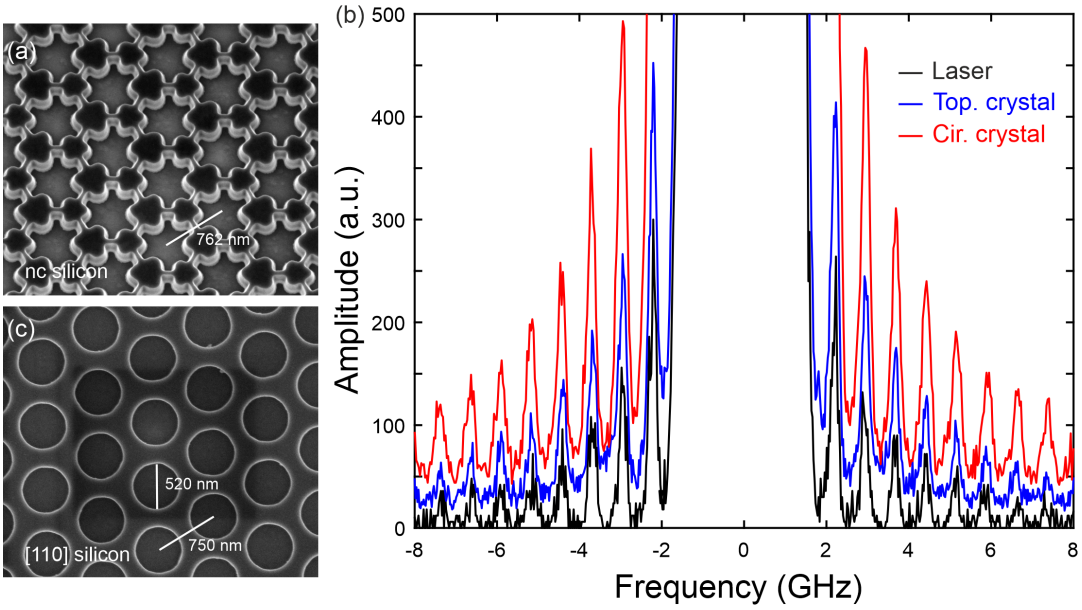

Figure 6.3: (a) SEM image of a topological crystal fabricated in nanocrystalline silicon. The period of the structure is 762 nm. (b) Brillouin spectrum obtained from the laser reference (black), topological crystal (blue) and circular phononic crystal (red). (c) Triangular phononic crystal of cricular hollows fabricated in a SOI wafer ([110] crystalline silicon) of 250 nm of thickness. The period of the structure is 750 nm and the diameter of the circles is 520 nm. These spectra show the influence of large size scatters in BLS measurements.

The blue curve in figure 6.3(b) shows the scattering spectra obtained from the topological crystal shown in figure 6.3(a). The measurement was taken with an angle of 25 degrees to ensure that no specular reflection was entering in the objective. The result was the same obtained with normal measurements in high reflecting surfaces. This kind of spectrum was not obtained before for measurements in the shamrock phononic crystals and waveguides described in chapters 3 and 4. The other difference with the previous structures besides the size and shape is the material used to fabricate this one. To discard that the origin of the peaks are from the use of nano crystaline silicon, figure 6.3(c) shows a SEM image of a triangular phononic crystal made of simple circular holes fabricated in the same SOI platform used to make the shamrock structures. The thickness is 250 nm, the period is 750 nm. similar to the

period of the topological crystal and the diameter of the circular holes are 520 nm approximately. the measured Brillouin spectrum is the red curve showed in 6.3(b).

The superposition of these three spectra shows the same frequency peaks and suggests that the the measured spectra for structures in figures 6.3(a) and (c) are the result of strong linear scattering coming from the light that is diffracted by the large periodic array that enters back into the collection objective. These results set a geometrical limitation for measurements in the BLS spectroscopy setup. Changing the laser for one with a longer wavelength is not an option because all the optics and detection system is fixed for a wavelength of 532 nm. The solution is to reduce the size of the scatter in the phononic crystal and figure 6.2 shows that the designed geometry also presents an isolated Dirac point for crystals with s=220 nm, which gives a period a=381 nm approximately. The experimental results obtained in the previous chapters shows that there will not be diffraction issues with this sizes. Besides that, these dimensions allows the use of standard SOI wafers for the fabrication of the structures in which this work already shown that theory and experiments agrees well.

6.6 Opening a gap for the Dirac cones in K

The next step to obtain the edge modes in the Valley approach is to open the Dirac point to create a gap. The way to do that is to break the C_6 symmetry of the crystal by changing the size of the rounded triangles that form the unit cell. Figure 6.4(a) shows the modified crystal and figure 6.4(b) the unit cell. The only change is that now there are two different circle radii r_1 and r_2 for each rounded triangle. The considered thickness is t=220 nm, the side of the hexagon is s=220 nm which gives a period a=381 nm. The width of the connectors are $w = 0.2s$=44 nm. $r_1 = 0.105a$ and $r_2 = 0.155a$. These values for the radius are optimized to open the largest possible gap.

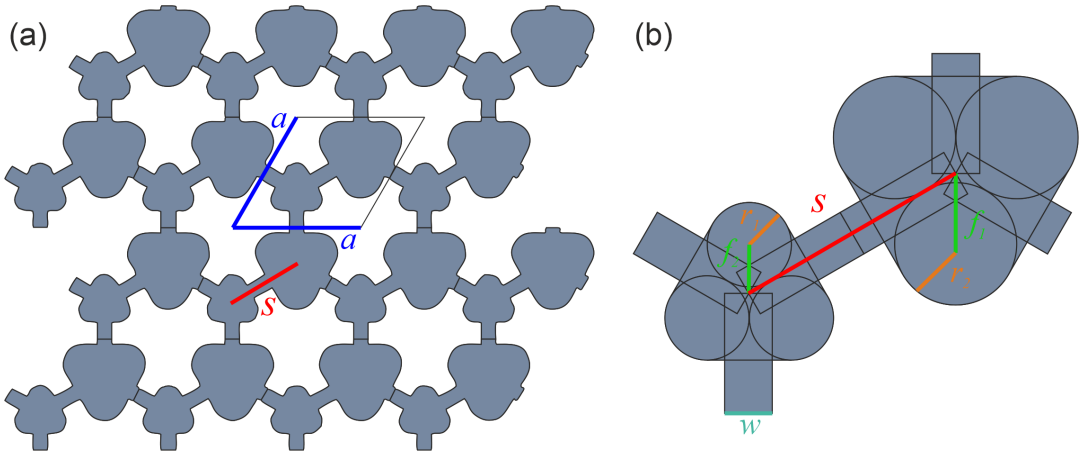

Figure 6.4: (a) Modified Valley Hall crystal geometry to perturb the system and lift the degeneracy of the Dirac point. (b) Unit cell for the new geometry. There is a different radius for each rounded triangle. The period and the width of the connectors remains the same as in the original geometry.

Figure 6.5 shows the dispersion relation only for the band that exhibits the Dirac point in figure 6.2 when s=220 nm. The calculation considers both isotropic silicon (a) and

[110] crystalline silicon (b). When $r_1 = r_2 = 0.13a$, there are two conical dispersion (Dirac cones) in each vertex of the Brillouin zone and they do not close completely in the case of crystalline silicon. This is a consequence of the inhomogeneity of the material. It will close completely for a closer value in the radius that can be further optimized.

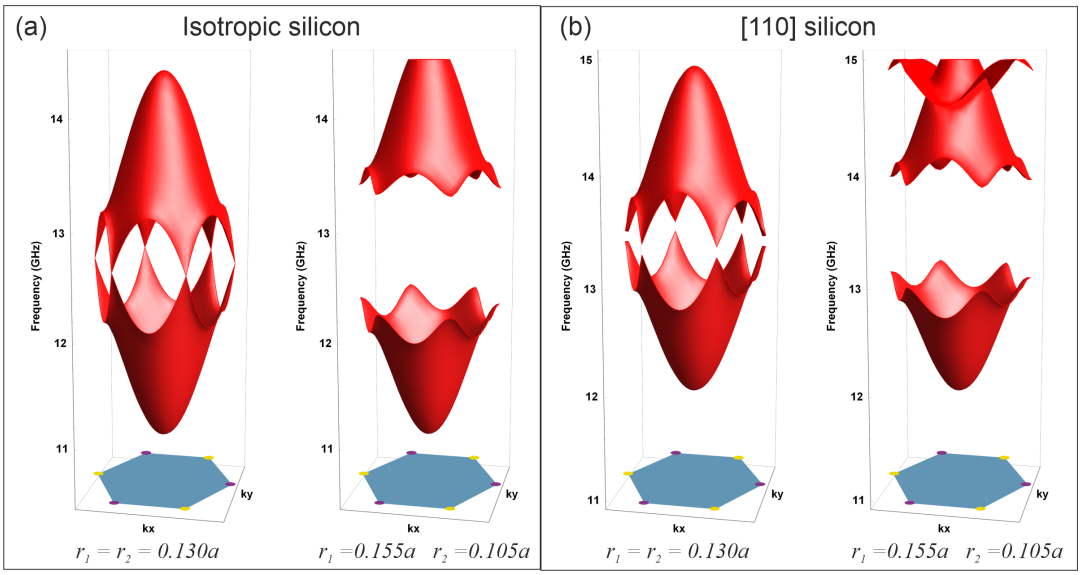

Figure 6.5: Phononic dispersion relation for isotropic (a), and [110] crystalline silicon (b) calculated along the entire Brillouin zone considering only the band that presents a Dirac point as shown figure 6.2. When $r_1 = r_2 = 0.13a$, there are two Dirac cones in each vertex of the hexagon (Brillouin zone), and it does not close completely for the case of [110] silicon. When $r_1 = 0.155a$ and $r_2 = 0.105a$, it is possible to open a full gap of approximately 1 GHz in both cases.

When $r_1 = 0.105a$ and $r_2 = 0.155a$, the degeneracy of the Dirac points is lifted and it is possible to open a gap from 12.27 GHz to 13.36 GHz for the isotropic case and from 13.03 GHz to 14.13 GHz in the [110] silicon. A gap of approximately 1 GHz is found in both cases which is important to resolve the peaks in the experimental measurements using the Brillouin setup. From now on, the calculations will be focused on the [110] crystalline silicon because this platform was already tested in this work using other phononic crystal geometries.

Once the degeneracy in the Dirac point was lifted, the next step is to ensure the band inversion of the mode profiles at the edges of the gap. This can be achieved in the VH approach just by flipping the unit cell of the crystal. Figure 6.6 shows the phononic band dispersion calculated considering the original and flipped unit cell. The dispersion relation is exactly the same because it is the same crystal in both cases. This figure is intended to show the mode profile at the edges of the gap and show the band inversion. The band inversion also can be understood intuitively because because in the lower edge of the gap, the mode profile is the same in both cases with the only difference that it is flipped. If the mode profiles are compared without taking into account the size of the rounded triangles, the mode profile in the lower band for the dispersion shown on the left is similar to the mode profile in the upper band shown on the right and vice versa.

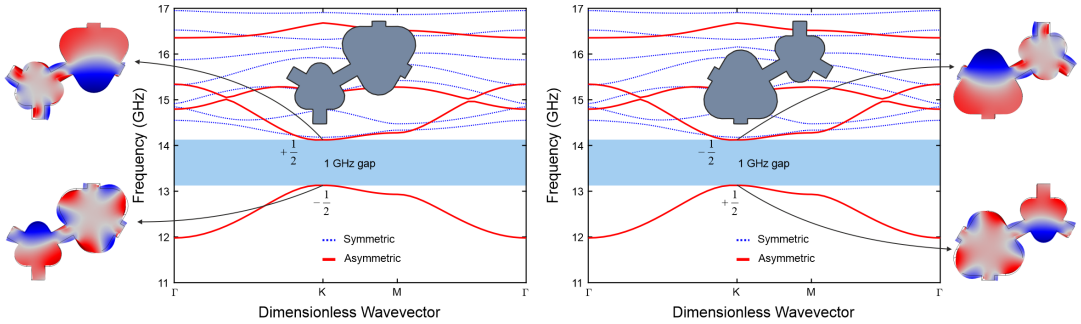

Figure 6.6: Phononic dispersion relation for the optimized geometry considering [110] silicon and the unit cell shown in the insets. The band diagram is exactly the same in both cases because it is the same simulated crystal; but the mode profile at the edges of the gap changes when the unit cell changes. It shows the band inversion required to obtain topological edge states inside the gap.

6.7 Valley Hall edge states

From literature [31, 85], is known that the Valley Chern numbers at the K point are $+1/2$ or $-1/2$ as shows figure 6.6. Therefore, according to the bulk-edge correspondence, if two crystals formed by different unit cells face each other as shown in figure 6.7, the gap needs to close to neutralize the Valley Chern numbers and re-open again. At this change of phase, an edge mode has to appear at the interface of both crystals, highlighted by the dotted line. The absolute value of the difference of Valley Chern numbers for the bands below the gap is $|\Delta C| = \left|+\frac{1}{2} - \left(-\frac{1}{2}\right)\right| = 1$, which corresponds with the number of modes that must appear inside the gap.

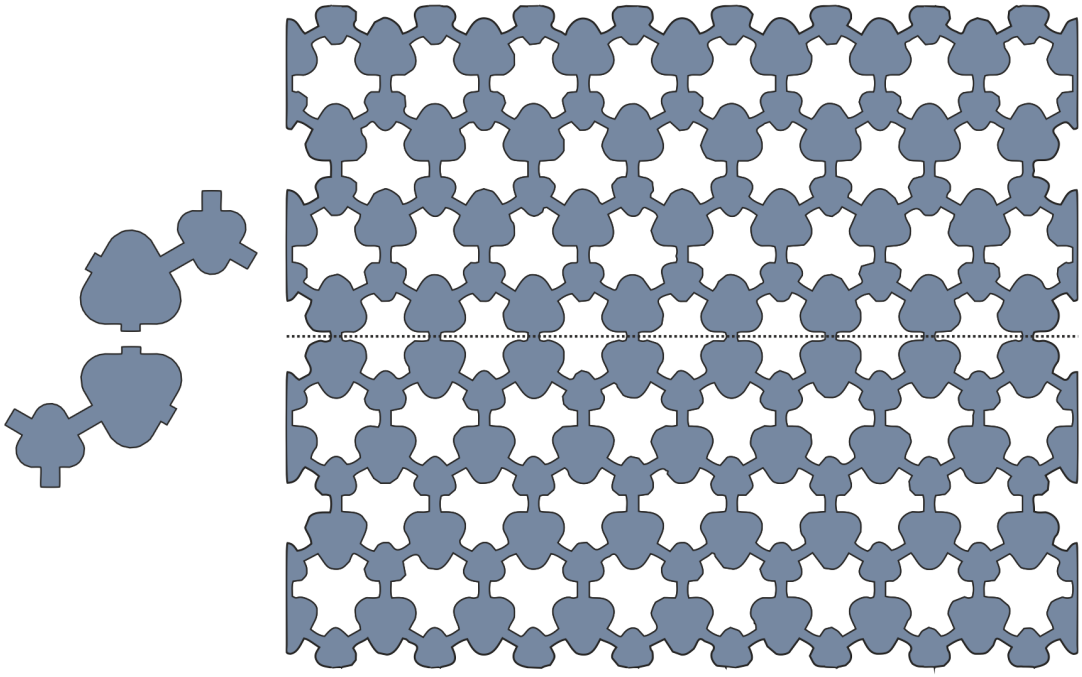

Figure 6.7: construction of the Valley Hall topological interface as a result of the interface between two different crystals formed by the flipped unit cells highlighted in the left part.

Figure 6.8 shows the simulated phononic dispersion relation for the geometry presented in figure 6.7. The considered material is the [110] crystalline silicon, the thicknes of the suspended membrane is t=220 nm, side of the hexagon s=220 nm, period a=381 nm, connectors width w=44 nm, radius $r_1 = 0.105a$=40 nm, and $r_2 = 0.155a$=59 nm. For these parameters, there is an isolated mode inside the gap going from approximately 13 GHz for $k_x = 0$, to 13.7 GHz for $k_x = \pi/a$.

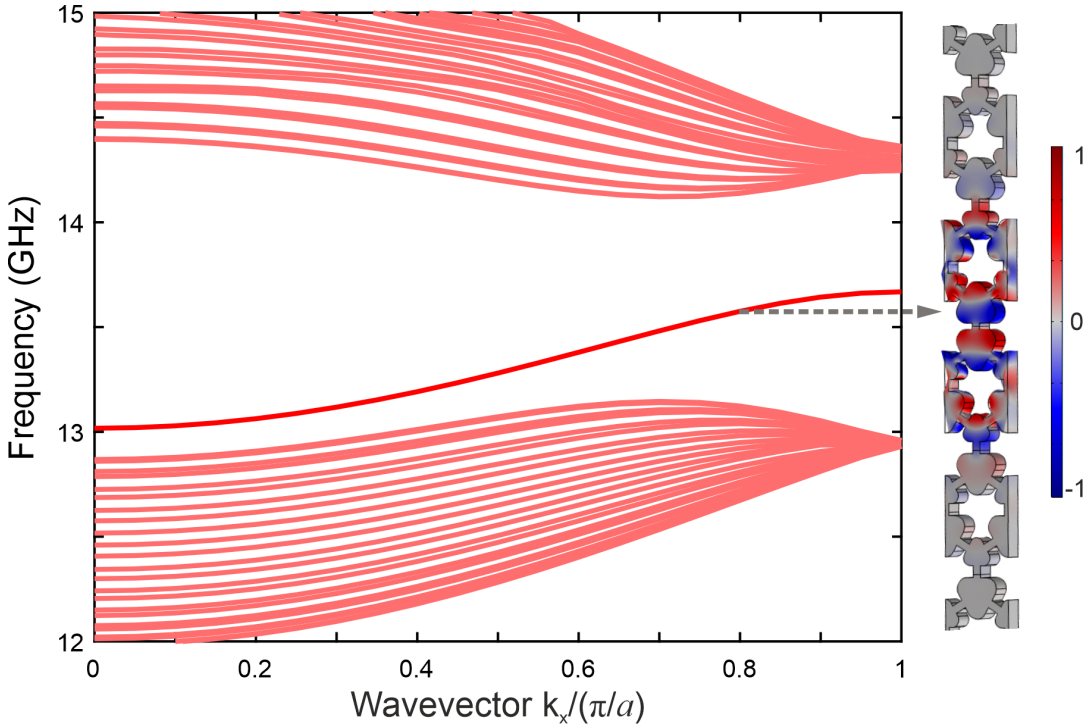

Figure 6.8: Phononic dispersion relation for the Valley Hall topological waveguide. There is a clear isolated mode inside the gap. The inset on the right shows the mode profile of the interface mode for $k_x/(\pi/a) = 0.8$. The mechanical displacement of the mode is localized at the interface of both crystals. Color bar indicates normalized out of plane displacement.

The inset on the right of figure 6.8 shows the mode profile of the guided mode for $k_x/(\pi/a) = 0.8$. The color bar indicates the normalized out of plane displacement. The mechanical displacement is fully localized at the interface of both crystals. The guided mode is well localized at the middle of the gap for wavevectors close to π/a. It increases the probability to be detected and resolved in the BLS spectroscopy setup. Therefore this is a potential geometrical configuration for the experimental detection of topological modes above 10 GHz for the first time.

6.8 Conclusions

This chapter presents the design of a topological crystal based on the Valley Hall approach. The influence of the anisotropy of the material is explored for the particular case of crystalline silicon. The main conclusions are summarized below.

- 2D Periodic structures with an hexagonal array similar to that of the graphene are the best systems to emulate the Valley hall approach in phononics because in many cases exceptional points are founded in K.
- For the proposed geometry, the anisotropy of the silicon restricts the design of topological structures to dimensions where the thickness of the membrane and the side of the hexagonal array coincides; it is, when $S = t$. For the case of isotropic silicon, it was shown that topological modes can be obtained at least for geometries with $S = t$ and $S = 2t$.
- With the design and fabrication of large periodic structures compared with the laser wavelength ($\lambda = 532$), an experimental limitation settled by the linear diffraction of the light by the periodic structure itself was evident. This sets an upper limit in the dimensions of the drilled scatters. The diameter of the drilled hole in 2D plates should be less than the laser wavelength used in the experiment.
- The valley Hall approach allows large gaps to be obtained which enables further experimental detection of topological edge states using BLS spectroscopy. The mass distribution of the unit cell in the proposed geometry results in a 1GHz gap for the optimized dimensions and an isolated edge mode that can be located right at the middle of the gap for certain mechanical wavevectors.

Chapter 7

Conclusions and perspectives

This thesis was intended to study the propagation of hypersonic waves in phononic waveguides. It covered the study of trivial waveguides and the more recently introduced topological waveguides. It also explores the advantages and limitations of both types of waveguides, the geometrical constraints for their realization and in this particular work, the experimental limitations for final characterization.

Here the physics behind the spontaneous Brillouin scattering was analytically detailed and a simplified approach was introduced for the scattering efficiency calculations based on the displacements of the interfaces under study and their overlap with the incident light. Besides that, the Brillouin light scattering spectroscopy technique was explained and presented as the measurement tool for the experimental results presented in this thesis.

The design of phononic crystals with wide bandgaps have many applications such as the engineering of the thermal conductance of the structure [10], and can be used as a platform to isolate thermal damping for the study of organic molecular systems [48], among others. Here we made a detailed study of the gap design as a function of the geometrical and intrinsic material parameters. A clear and direct characterization of hypersonic band gaps covering different directions in the reciprocal space was also presented here [87]. At the time of writing this thesis, similar results in the literature was not reported.

One advantage to use shamrock crystals to design defect line waveguides is that the wide bandgaps in these structures allows a better resolution for the measurement of guided modes. In small gaps these modes can be mixed and difficult to identify. the results in chapter 4 show a measured guided mode isolated at least one GHz from lower and higher frequencies. This also makes shamrock waveguides a nice platform for the integration of IDT transducers. The constraints in the design of the fingers in the transducers can be relaxed to cover a broad range of frequencies without exciting undesired mechanical modes.

From the design of topological waveguides, some geometrical limitations were clear. In the case of the QSHE, the small change in the mass distribution within the crystal unit cell, limits the width of the gap that can be opened from the shrunken or expanded configurations. This sets some limitations for the experimental characterization using BLS spectroscopy. One possible solution is to downscale the full system to enlarge the gap but the E-beam lithography fabrication becomes even harder, or almost impossible.

It seems that the most suitable system for the experimental demonstration of topological transport above 10 GHz frequencies is the QVHE geometry approach. This is

true at least for the materials, dimensions, and characterization techniques explored throughout this work. This configuration enables the possibility to open wide gaps after lifting the degeneracy of Dirac points and obtain centered and isolated topological edge modes.

7.1 BLS spectroscopy mapping

The BLS spectroscopy technique joined with an external excitation source can be a powerful tool to show phonon transport and robustness in trivial and topological waveguides. The general idea of the proposed system is shown in figure 7.1. the external excitation is illustrated as an IDT transducer that can excite one or more guided modes of the waveguide structure. If it is possible to couple the excitation into the structure, the BLS setup can map different positions, by placing the incident laser along the waveguide, notated in the figure with numbers, and record the amplitude of the measurement for a certain period of time. The changes in amplitude along the waveguide, as illustrated on the right part of the figure, can give information about the attenuation of the propagated mode.

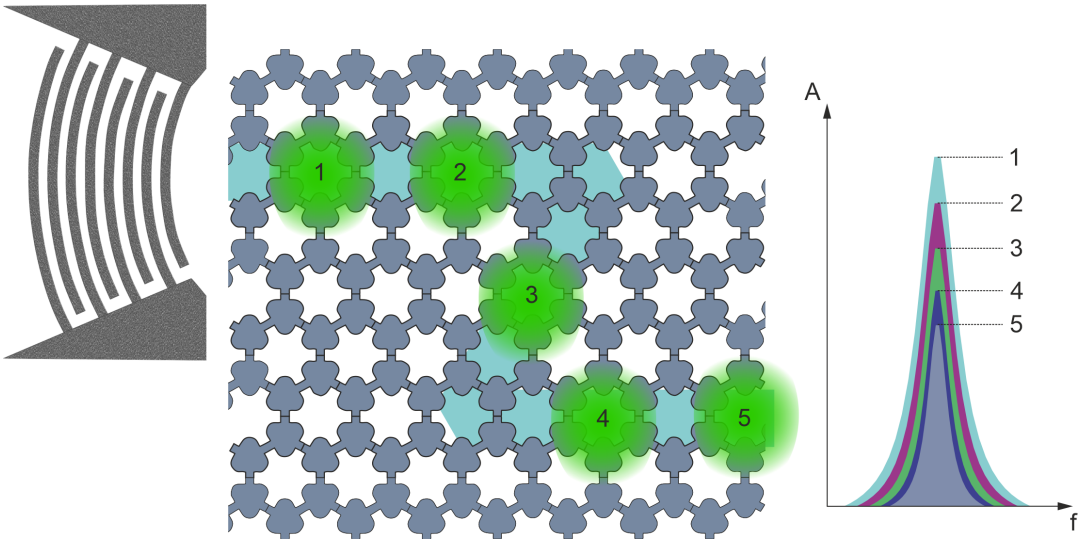

Figure 7.1: Phonon trasport measurements using BLS spectroscopy. An external source illustrated here as an IDT transducer can excite guided modes of the system. The incident laser can be placed in different points along the waveguide to measure in the same period of time, the amplitude of the light scattered by the guided mode. The attenuation of the peak can give information about the robustness of the guided mode.

For the case of trivial waveguides, it will be interesting to see the phonon propagation along straight waveguides, evaluate the robustness of different configurations and also explore the so called glide-plane waveguides [64, 65], to see if it is possible to obtain trivial chiral phonon transport at GHz frequencies. Waveguides with angles also can be designed and measured to have an estimation on how much a trivial mode is scattered when facing a change of direction in the path.

For the topological waveguides the robustness along Z and Ω shaped bends can be evaluated, as is explored in almost all the works that intend to evaluate the robustness of the interface waveguides [30, 31, 72, 86, 88–90]. For the particular case of Valley Hall, different topological interfaces can be explored beside the bridge interface presented in chapter 6. Zig-zag interfaces can support two guided modes [91], one of them being topologically protected, and the other one being a trivial guided mode. This can be an ideal structure to compare the robustness of trivial and topological modes propagating along the same interface. The robustness of each mode can be evaluated simultaneously and provides experimental proof that topology in fact works and is better when compared with non-protected guided modes.

Even without an external source of excitation, BLS spectroscopy is a promising tool for the characterization of topological waveguides. As was shown in chapter 3 for the shamrock crystal, this technique allows band characterization and band reconstruction of a Dirac point as was done before for KHz frequencies [92]. These experimental results set the basis to prove the topological nature of an interface mode that also can be potentially detected.

Bibliography

[1] Alexander G Krause et al. “A high-resolution microchip optomechanical accelerometer”. In: *Nature Photonics* 6.11 (2012), pp. 768–772.

[2] Julien Chaste et al. “A nanomechanical mass sensor with yoctogram resolution”. In: *Nature nanotechnology* 7.5 (2012), pp. 301–304.

[3] Emanuel Gavartin, Pierre Verlot, and Tobias J Kippenberg. “A hybrid on-chip optomechanical transducer for ultrasensitive force measurements”. In: *Nature nanotechnology* 7.8 (2012), pp. 509–514.

[4] John D Teufel et al. “Sideband cooling of micromechanical motion to the quantum ground state”. In: *Nature* 475.7356 (2011), pp. 359–363.

[5] Jasper Chan et al. “Laser cooling of a nanomechanical oscillator into its quantum ground state”. In: *Nature* 478.7367 (2011), pp. 89–92.

[6] Michael Sigalas and Eleftherios N Economou. “Band structure of elastic waves in two dimensional systems”. In: *Solid state communications* 86.3 (1993), pp. 141–143.

[7] Manvir S Kushwaha et al. “Acoustic band structure of periodic elastic composites”. In: *Physical review letters* 71.13 (1993), p. 2022.

[8] Rosa Martínez-Sala et al. “Sound attenuation by sculpture”. In: *nature* 378.6554 (1995), pp. 241–241.

[9] Taras Gorishnyy et al. “Hypersonic phononic crystals”. In: *Physical review letters* 94.11 (2005), p. 115501.

[10] Nobuyuki Zen et al. “Engineering thermal conductance using a two-dimensional phononic crystal”. In: *Nature communications* 5.1 (2014), pp. 1–9.

[11] Matt Eichenfield et al. “Optomechanical crystals”. In: *Nature* 462.7269 (2009), pp. 78–82.

[12] Gregory S MacCabe et al. “Nano-acoustic resonator with ultralong phonon lifetime”. In: *Science* 370.6518 (2020), pp. 840–843.

[13] Kejie Fang et al. “Optical transduction and routing of microwave phonons in cavity-optomechanical circuits”. In: *Nature Photonics* 10.7 (2016), pp. 489–496.

[14] Rishi N Patel et al. “Single-mode phononic wire”. In: *Physical review letters* 121.4 (2018), p. 040501.

[15] Hengjiang Ren et al. “Two-dimensional optomechanical crystal cavity with high quantum cooperativity”. In: *Nature communications* 11.1 (2020), pp. 1–10.

[16] Jordi Gomis-Bresco et al. “A one-dimensional optomechanical crystal with a complete phononic band gap”. In: *Nature communications* 5.1 (2014), pp. 1–6.

[17] Saeed Mohammadi et al. “Evidence of large high frequency complete phononic band gaps in silicon phononic crystal plates”. In: *Applied Physics Letters* 92.22 (2008), p. 221905.

[18] Sarah Benchabane et al. “Guidance of surface waves in a micron-scale phononic crystal line-defect waveguide”. In: *Applied Physics Letters* 106.8 (2015), p. 081903.

[19] Wei Cheng et al. “Observation and tuning of hypersonic bandgaps in colloidal crystals”. In: *Nature materials* 5.10 (2006), pp. 830–836.

[20] B Graczykowski et al. “Phonon dispersion in hypersonic two-dimensional phononic crystal membranes”. In: *Physical Review B* 91.7 (2015), p. 075414.

[21] Qiyu Liu, Huan Li, and Mo Li. “Electromechanical Brillouin scattering in integrated optomechanical waveguides”. In: *Optica* 6.6 (2019), pp. 778–785.

[22] K v Klitzing, Gerhard Dorda, and Michael Pepper. “New method for high-accuracy determination of the fine-structure constant based on quantized Hall resistance”. In: *Physical Review Letters* 45.6 (1980), p. 494.

[23] David J Thouless et al. “Quantized Hall conductance in a two-dimensional periodic potential”. In: *Physical review letters* 49.6 (1982), p. 405.

[24] Michael Victor Berry. “Quantal phase factors accompanying adiabatic changes”. In: *Proceedings of the Royal Society of London. A. Mathematical and Physical Sciences* 392.1802 (1984), pp. 45–57.

[25] Xiujuan Zhang et al. “Topological sound”. In: *Communications Physics* 1.1 (2018), pp. 1–13.

[26] B Andrei Bernevig, Taylor L Hughes, and Shou-Cheng Zhang. “Quantum spin Hall effect and topological phase transition in HgTe quantum wells”. In: *science* 314.5806 (2006), pp. 1757–1761.

[27] Long Ju et al. “Topological valley transport at bilayer graphene domain walls”. In: *Nature* 520.7549 (2015), pp. 650–655.

[28] FDM Haldane and S Raghu. “Possible realization of directional optical waveguides in photonic crystals with broken time-reversal symmetry”. In: *Physical review letters* 100.1 (2008), p. 013904.

[29] Cheng He et al. “Acoustic topological insulator and robust one-way sound transport”. In: *Nature physics* 12.12 (2016), pp. 1124–1129.

[30] Jiuyang Lu et al. “Observation of topological valley transport of sound in sonic crystals”. In: *Nature Physics* 13.4 (2017), pp. 369–374.

[31] Qicheng Zhang et al. “Gigahertz topological valley Hall effect in nanoelectromechanical phononic crystals”. In: *Nature Electronics* 5.3 (2022), pp. 157–163.

[32] Léon Brillouin. “Diffusion de la lumière et des rayons X par un corps transparent homogène”. In: *AnPh* 9.17 (1922), pp. 88–122.

[33] Charles Kittel and Paul McEuen. *Introduction to solid state physics*. Vol. 8. Wiley New York, 1976.

[34] DF Nelson and M Lax. “Theory of the photoelastic interaction”. In: *Physical Review B* 3.8 (1971), p. 2778.

[35] Yariv Amnon and Pochi Yeh. “Optical waves in crystals: propagation and control of laser radiation”. In: *New York City, NY: Wiley* (1984).

[36] Jieping Xu and Robert Stroud. *Acousto-optic devices: principles, design, and applications*. Wiley, 1992.

[37] LS Hounsome et al. “Photoelastic constants in diamond and silicon”. In: *physica status solidi (a)* 203.12 (2006), pp. 3088–3093.

[38] Steven G Johnson et al. "Perturbation theory for Maxwell's equations with shifting material boundaries". In: *Physical review E* 65.6 (2002), p. 066611.

[39] Omar Florez et al. "Brillouin scattering self-cancellation". In: *Nature communications* 7.1 (2016), pp. 1–8.

[40] Raphaël Van Laer et al. "Interaction between light and highly confined hypersound in a silicon photonic nanowire". In: *Nature Photonics* 9.3 (2015), pp. 199–203.

[41] SM Lindsay, MW Anderson, and JR Sandercock. "Construction and alignment of a high performance multipass vernier tandem Fabry–Perot interferometer". In: *Review of scientific instruments* 52.10 (1981), pp. 1478–1486.

[42] Manuel Cardona, Gernot Güntherodt, and R Merlin. *Light scattering in solids III: recent results*. Vol. 3. Springer, 1982.

[43] Ralf Lucklum, Mikhail Zubtsov, and Aleksandr Oseev. "Phoxonic crystals—a new platform for chemical and biochemical sensors". In: *Analytical and bioanalytical chemistry* 405.20 (2013), pp. 6497–6509.

[44] Jordi Gomis-Bresco et al. "A PhoXonic crystal: Photonic and phononic bandgaps in a 1D optomechanical crystal". In: *2014 16th International Conference on Transparent Optical Networks (ICTON)*. IEEE. 2014, pp. 1–4.

[45] Bahram Djafari-Rouhani, Said El-Jallal, and Yan Pennec. "Phoxonic crystals and cavity optomechanics". In: *Comptes Rendus Physique* 17.5 (2016), pp. 555–564.

[46] Zhengyou Liu et al. "Locally resonant sonic materials". In: *science* 289.5485 (2000), pp. 1734–1736.

[47] Zian Jia et al. "Designing phononic crystals with wide and robust band gaps". In: *Physical Review Applied* 9.4 (2018), p. 044021.

[48] Burak Gurlek, Vahid Sandoghdar, and Diego Martin-Cano. "Engineering long-lived vibrational states for an organic molecule". In: *Physical Review Letters* 127.12 (2021), p. 123603.

[49] Amir H Safavi-Naeini and Oskar Painter. "Design of optomechanical cavities and waveguides on a simultaneous bandgap phononic-photonic crystal slab". In: *Optics express* 18.14 (2010), pp. 14926–14943.

[50] Amir H Safavi-Naeini et al. "Two-dimensional phononic-photonic band gap optomechanical crystal cavity". In: *Physical Review Letters* 112.15 (2014), p. 153603.

[51] Immo Söllner, Leonardo Midolo, and Peter Lodahl. "Deterministic single-phonon source triggered by a single photon". In: *Physical review letters* 116.23 (2016), p. 234301.

[52] A Srikantha Phani, J Woodhouse, and NA Fleck. "Wave propagation in two-dimensional periodic lattices". In: *The Journal of the Acoustical Society of America* 119.4 (2006), pp. 1995–2005.

[53] Florian Maurin et al. "Probability that a band-gap extremum is located on the irreducible Brillouin-zone contour for the 17 different plane crystallographic lattices". In: *International Journal of Solids and Structures* 135 (2018), pp. 26–36.

[54] Marcus Albrechtsen et al. "Nanometer-scale photon confinement in topology-optimized dielectric cavities". In: *arXiv preprint arXiv:2108.01681* (2021).

[55] Geraint Owen and Paul Rissman. "Proximity effect correction for electron beam lithography by equalization of background dose". In: *Journal of Applied Physics* 54.6 (1983), pp. 3573–3581.

[56] Vy Thi Hoang Nguyen et al. "The CORE sequence: A nanoscale fluorocarbon-free silicon plasma etch process based on SF6/O2 cycles with excellent 3D profile control at room temperature". In: *ECS journal of solid state science and technology* 9.2 (2020), p. 024002.

[57] Robert W Boyd. *Nonlinear optics*. Academic press, 2020.

[58] R Loudon and JR Sandercock. "Analysis of the light-scattering cross section for surface ripples on solids". In: *Journal of Physics C: Solid State Physics* 13.13 (1980), p. 2609.

[59] K Charles Kao and George A Hockham. "Dielectric-fibre surface waveguides for optical frequencies". In: *Proceedings of the Institution of Electrical Engineers*. Vol. 113. 7. IET. 1966, pp. 1151–1158.

[60] Jeff Hecht. *City of light: the story of fiber optics*. Oxford University Press on Demand, 2004.

[61] Abdelkrim Khelif and Ali Adibi. *Phononic crystals: fundamentals and applications*. Springer, 2015.

[62] Jean-Michel Lourtioz et al. *Photonic crystals: towards nanoscale photonic devices*. Springer, 2008.

[63] John D Joannopoulos et al. *Photonic crystals: molding the flow of light*. Springer, 2008.

[64] Peter Lodahl et al. "Chiral quantum optics". In: *Nature* 541.7638 (2017), pp. 473–480.

[65] Immo Söllner et al. "Deterministic photon–emitter coupling in chiral photonic circuits". In: *Nature nanotechnology* 10.9 (2015), pp. 775–778.

[66] Mikio Nakahara. *Geometry, topology and physics*. CRC Press, 2003.

[67] Barry Bradlyn et al. "Topological quantum chemistry". In: *Nature* 547.7663 (2017), pp. 298–305.

[68] Charles L Kane and Eugene J Mele. "Quantum spin Hall effect in graphene". In: *Physical review letters* 95.22 (2005), p. 226801.

[69] Long-Hua Wu and Xiao Hu. "Scheme for achieving a topological photonic crystal by using dielectric material". In: *Physical review letters* 114.22 (2015), p. 223901.

[70] Sabyasachi Barik et al. "Two-dimensionally confined topological edge states in photonic crystals". In: *New Journal of Physics* 18.11 (2016), p. 113013.

[71] Sabyasachi Barik et al. "A topological quantum optics interface". In: *Science* 359.6376 (2018), pp. 666–668.

[72] Si-Yuan Yu et al. "Elastic pseudospin transport for integratable topological phononic circuits". In: *Nature communications* 9.1 (2018), pp. 1–8.

[73] Ling Lu, John D Joannopoulos, and Marin Soljačić. "Topological photonics". In: *Nature photonics* 8.11 (2014), pp. 821–829.

[74] Barry Simon. "Holonomy, the quantum adiabatic theorem, and Berry's phase". In: *Physical Review Letters* 51.24 (1983), p. 2167.

[75] Alfred Shapere and Frank Wilczek. *Geometric phases in physics*. Vol. 5. World scientific, 1989.

[76] Arno Bohm et al. *The Geometric phase in quantum systems: foundations, mathematical concepts, and applications in molecular and condensed matter physics*. Springer, 2003.

[77] Fukui Takahiro, Hatsugai Yasuhiro, and Suzuki Hiroshi. "Chern Numbers in Discretized Brillouin Zone: Efficient Method of Computing (Spin) Hall Conductances". In: *Journal of the Physical Society of Japan* (2005).

[78] Di Xiao, Ming-Che Chang, and Qian Niu. "Berry phase effects on electronic properties". In: *Reviews of modern physics* 82.3 (2010), p. 1959.

[79] Xiao-Liang Qi and Shou-Cheng Zhang. "Topological insulators and superconductors". In: *Reviews of Modern Physics* 83.4 (2011), p. 1057.

[80] Mário G Silveirinha. "Bulk-edge correspondence for topological photonic continua". In: *Physical Review B* 94.20 (2016), p. 205105.

[81] Vincent Laude. "Principles and properties of phononic crystal waveguides". In: *Apl Materials* 9.8 (2021), p. 080701.

[82] Mário G Silveirinha. "Proof of the bulk-edge correspondence through a link between topological photonics and fluctuation-electrodynamics". In: *Physical Review X* 9.1 (2019), p. 011037.

[83] Nikhil Parappurath et al. "Direct observation of topological edge states in silicon photonic crystals: Spin, dispersion, and chiral routing". In: *Science advances* 6.10 (2020), eaaw4137.

[84] Kostya S Novoselov et al. "Unconventional quantum Hall effect and Berry's phase of 2π in bilayer graphene". In: *Nature physics* 2.3 (2006), pp. 177–180.

[85] Mikhail I Shalaev et al. "Robust topologically protected transport in photonic crystals at telecommunication wavelengths". In: *Nature nanotechnology* 14.1 (2019), pp. 31–34.

[86] Hengjiang Ren et al. "Topological phonon transport in an optomechanical system". In: *Nature communications* 13.1 (2022), pp. 1–7.

[87] Omar Florez et al. "Engineering nanoscale hypersonic phonon transport". In: *arXiv preprint arXiv:2202.02166* (2022).

[88] Xin-Tao He et al. "A silicon-on-insulator slab for topological valley transport". In: *Nature communications* 10.1 (2019), pp. 1–9.

[89] Motoki Kataoka, Masaaki Misawa, and Kenji Tsuruta. "Design and Robustness Evaluation of Valley Topological Elastic Wave Propagation in a Thin Plate with Phononic Structure". In: *Symmetry* 14.10 (2022), p. 2133.

[90] Bakhtiyar Orazbayev and Romain Fleury. "Quantitative robustness analysis of topological edge modes in C6 and valley-Hall metamaterial waveguides". In: *Nanophotonics* 8.8 (2019), pp. 1433–1441.

[91] Hironobu Yoshimi et al. "Experimental demonstration of topological slow light waveguides in valley photonic crystals". In: *Optics Express* 29.9 (2021), pp. 13441–13450.

[92] Daniel Torrent and José Sánchez-Dehesa. "Acoustic analogue of graphene: observation of Dirac cones in acoustic surface waves". In: *Physical review letters* 108.17 (2012), p. 174301.